Alma Mater Studiorum
Università di Bologna

DOTTORATO DI RICERCA IN

Scienze Ambientali:

Tutela E Gestione Delle Risorse Naturali

Ciclo XXIII

Settore scientifico-disciplinare di afferenza: GEO/12

"Development Of Oil Spill Detection Techniques For Satellite Optical Sensors And Their Application To Monitor Oil Spill Discharge In The Mediterranean Sea"

Presentata da: Andrea Pisano

Coordinatore Dottorato — Enrico Dinelli

Relatore — Nadia Pinardi

Esame finale anno 2011

Correlatore

Rosalia Santoleri

Index

Abstract

Development Of Oil Spill Detection Techniques For Satellite Optical Sensors And Their Application To Monitor Oil Spill Discharge In The Mediterranean Sea

Andrea Pisano

Marine oil pollution, beyond rare accidents, is a highly frequent activity mainly coming from illegal discharges of hydrocarbons intentionally released by ships into the marine environment. Naval and aerial surveillance is generally adopted in monitoring activities for maritime traffic and ocean pollution, although cannot provide a regular, continuous and synoptic monitoring due to the limitations in space, time and weather conditions. Satellite remote sensing can play an important complementary and supporting role for continuous monitoring and early detection of oil spill discharges at sea. In the last decades, several research and pre-operational projects clearly demonstrated the capability of satellite synthetic aperture radar (SAR) sensors in oil spill detection. At present, SAR detection is commonly part of the early warning monitoring systems currently used by several Nations or International agencies. However, the narrow swath (100-400 km) and long revisit time of SAR sensors and the high cost of their images strongly limit the possibility to have a daily monitoring of large areas of the ocean. To overcome SAR limitations we developed a new methodology which makes use of satellite optical sensors, characterized by very large swaths (1500-2000 km), short revisit times and free of charge. We used for the first time MODIS high and medium resolution (250 and 500 m) and MERIS full resolution (300 m) top of atmosphere reflectance imagery and developed an innovative highly automated detection technique.

The developed oil spill detection method consists of three main parts – image flattening, features extraction and oil spill classification. Image flattening is the procedure

to obtain identifiable spills in optical reflectance images and involves the removal of oceanic and atmospheric natural variability in order to enhance oil-water contrast. The basic idea is the elimination of all signals extraneous to the response of oil and clean water exalting oil-water contrast. This is made of several customized steps that aim to improve the oil spill spectral signal at the top of the atmosphere instead of detecting the spectral signature on sea surface after removal of the atmospheric contribution. The result of this step is a new image (the flattened image) in which oil spill better stands out. Further, this procedure has permitted to define the optimal reflectance band in which to detect the hydrocarbon. The features extraction method applies to the flattened image and relies on a new clustering algorithm which groups and contours oil spill signatures with similar reflectance into clusters, i.e. regions with common mode reflectance values. Each cluster is composed by many regions among which one or more oil spills can belong to. To identify and retain only oil spill regions, we apply to each cluster region a set of *"slick features parameters"*. These parameters have been determined by analyzing a set of reference oil spills observed *in situ* and are related to the area, shape and reflectance properties, as reflectance contrast, of hydrocarbons. This analysis allowed to define the spectral, geometric and statistical criteria to discriminate between oil spills and look-alike clusters (e.g. slick-like regions with wrong region-water contrast). After pruning, most of obviously non-slick features (e.g. large regions) and look-alikes are eliminated. However, slick patchiness, residual natural variability after flattening, small residual clouds, etc., contribute to the impossibility to automatically eliminate all look-alikes with the above "clear-cut" pruning criteria. This required our oil spill candidates to be further analyzed. Therefore, an oil spill classification method has been developed. It is based on the assignment of a score to each candidate oil spill remaining after pruning. Scores have been devised from a second set of features parameters, which take into account the spectral difference between each candidate region and surrounding water. The final result is a classification of candidate oil spill regions by means of the assignment of a score as level of confidence.

The method has been tested and validated using an independent dataset of 101 oil spills observed in situ and revealed its capability to detect also small slicks coming from illegal discharges. The success of the method was quantified by comparing the automated classified slicks against the certified oil spills. The result of this validation shows that the method was able to detect 78% of the certified oil spill cases. Obviously, optical sensors are not able to detect spills when the area is covered by clouds. The comparison with respect to SAR detection results indicated the inability of lower spatial resolution optical sensors, such as MODIS and MERIS, to detect spills when the dimension is less than 1 Km^2.

Introduction

Oil and oil product spillages at sea are highly frequent events, taking place all the time and worldwide. Beyond rare accidents, caused by ships in distress, rupture of pipelines or malfunctioning of oil extraction platforms, marine oil pollution is "operational", that is due to the illegal discharges of hydrocarbons intentionally released by ships into the marine environment along transportation routes. Based on reports on marine oil pollution (Huijer, 2005; REMPEC, 2002; Fingas, 2001; ESA, 1998; ITOPF), is estimated that annually about the 45% of the global oil pollution comes from operative discharges from ships, while tankers and platforms accidents contribute only to 5% and 2% respectively. Thus deliberate spills appear with considerably higher frequency than those corresponding to reported ship accidents. Operational pollution has become a common practice, mainly along maritime traffic routes, representing the main source of marine pollution from ships. The Mediterranean basin, due to its strategic position, has always represented a major route for transportation. As regards oil transport, the *Regional Marine Pollution Emergency Response Center for the Mediterranean Sea* (REMPEC), has estimated that about the 25% of the world's sea-borne oil traffic transits the Mediterranean. It has been estimated that up to some 600.000 tons of oil and oily waters are spilled in the Mediterranean Sea every year due to operational pollution (REMPEC 2002).

While accidental pollution at sea can be reduced yet never completely eliminated, illegal discharges from ships can indeed be eliminated by the strict enforcement of existing regulations and the control, monitoring and surveillance of maritime traffic. Several Mediterranean coastal states however are not provided with ships, aircrafts or other means specially equipped for pollution surveillance and therefore lack a regular surveillance service as well as a standard pollution reporting system. Besides encouraging the discharge of contaminated ballast waters or oily mixtures, a first consequence of the situation is the absence, for the Mediterranean, of verified data on spills due to illegal discharges from ships and the only existing observational data are those few cases occasionally reported by various sources (ships, civilian and military airplanes). In particular, the scarcity of relevant observational data makes even a preliminary estimation of the dimension, distribution and evolution of the problem virtually impossible. The identification of "hot spots" (i.e., the areas at major risk of operational pollution) is also extremely difficult. Nevertheless, the

urgent need for an enhanced surveillance and monitoring capability over the whole basin, which has to be primarily oriented to the prevention and control of illicit discharges from ships, is commonly accepted. In support of these goals, the set up of the *European Maritime Safety Agency* (EMSA), created in the wake of the *Erika* and *Prestige* oil tanker accidents (Regulation (EC) 1406/2002), is one of the key European level initiatives aimed at improving the enhancement of the overall maritime safety system within the Community. The Agency's main objective is to provide technical and scientific assistance to the European Commission and Member States in the proper development and implementation of EU legislation on maritime safety (Regulation (EC) 2038/2006), pollution by ships and security on board ships. To do this, one of EMSA's most important supporting tasks is to improve cooperation with, and between, Member States in all key areas. In addition, the Agency has operational tasks in oil pollution preparedness, detection and response.

Naval and aerial surveillance is generally adopted in monitoring activities for maritime traffic and ocean pollution. Aircrafts are more suitable to be brought into action to identify the polluter, the extent and the type of spill. An example is the German aerial surveillance, which locates oil discharges by SLAR (Side-Looking Airborne Radar), infrared/ultraviolet (IR/UV) scanning is used to quantify the extent of the film, a microwave radiometer (MWR) is used to quantify the thickness and a laser-fluoro-sensor (LFS) is used for oil type classification (Trieshmann *et al.*, 2003). Airborne and naval surveillance is however limited by the high costs and is not efficient for wide areas due to the limited coverage. In fact, ships and aircrafts they cannot provide a regular, continuous and synoptic monitoring due to the limitations in space, time and weather conditions. Further, several Mediterranean coastal states, especially in the southern boundary of the basin, are not provided with means specially equipped for pollution monitoring.

Satellites can play an important complementary and supporting role in detecting and deterring pollution from ships. Furthermore, whenever a real time early-warning message can be passed to responsible authorities, mainly Coast Guards, satellites can effectively support the possibility of the identification of the polluting ship and ultimately the prosecution of offenders. In the last decade, satellite remote sensing has proved to be an effective support in detecting these events. Since the launch (1992) of the first ESA *Synthetic Aperture RADAR* (SAR) ERS-1 satellite, several projects exploit SAR in oil spill detection within the Mediterranean basin. Among others, we may recall a series of projects funded by the European commission and the European Space Agency (ESA), such as AESOP (AErial and Satellite surveillance of Operational Pollution in the Adriatic Sea) (Ferraro *et al.*, 2007), RAMSES (Regional earth observation Application for Mediterranean Sea Emergency Surveillance), VASCO (Value Added provision for Slicks and hazardous

Cargoes Operational detection) and CLEOPATRA (Chemical Effluent and Oil Pollution Alert and TRAcking), as well as several studies performed by the EC-JRC in the field (Ferraro *et al.*, 2007; Ferraro *et al.*, 2006 a) and b); Tarchi *et al.*, 2006; Topouzelis *et al.*, 2006; Pavlakis *et al.*, 2001). EMSA manages a SAR satellite-based monitoring system for marine oil spill detection and surveillance in European waters (CleanSeaNet). This service provides a range of detailed information including oil spill alerts to Member States and rapid delivery of available satellite images and oil slick position. At present, SAR sensors are of primary use for their well demonstrated capability in oil spill detection, but long revisit times and low spatial coverage, due to SAR high spatial resolution and consequent narrow swaths, typically of order 100-400 km, call for a multi-platform SAR slick detection effort as well as wider swaths platforms, i.e. optical sensor satellites (with swath greater than 1000 km). Optical oil spill detection is very recent (since 2000, Hu, 2003), thanks to the increased spatial resolution of the new generation optical sensors, i.e. *Moderate Resolution Imaging Spectroradiometer* (MODIS) onboard NASA's TERRA and AQUA platforms and *Medium Resolution Imaging Spectrometer* (MERIS) on board the European Space Agency (ESA)'s ENVISAT platform. The 250 m and 300 m spatial resolution of some MODIS and all MERIS optical bands are now comparable to typical illegal discharge slick dimensions (1-10 km), while the typical 1 km resolution of past sensors was practically useless in slick detection, if one excludes major disasters which do not need to be detected, but only monitored in their evolution in time. In synthesis, SAR and optical platform observations have to be combined to optimize monitoring, which is hindered by low coverage and high revisit times in exclusively SAR observation systems and cloud cover in their optical counterparts.

The main objective of this thesis is to explore the potential capability of optical sensors in oil spill detection. We have developed a new methodology to detect oil spills in optical satellite sensors imagery, studying MODIS and MERIS images. This research effort was part of the PRIMI (PRogetto pilota Inquinamento Marino da Idrocarburi/Pilot Project Marine Oil Pollution) pilot project (Nirchio *et al.*, 2009), funded by the *Italian Space Agency* (ASI). PRIMI has implemented a modular operational system for the continuous monitoring of marine oil pollution and forecast of oil pollutants' dispersion in the Italian seas. The system makes use of up-to-date space technologies both for the marine environment monitoring and for the assimilation of satellite data into forecasting models. It consists of four components, two of which for oil slick detection via multi-platform SAR and optical satellite imagery, an oil spill displacement forecast subsystem based on numerical circulation models and a central archive that provides WEB-GIS services to users. The innovative strategy of PRIMI oil spill monitoring system relies in the inclusion of ocean colour imagery in the observational module, thus permitting a daily coverage of large areas,

such as the Italian seas or the Mediterranean Sea, which couldn't rely on SAR data alone. The efficiency of present optical imagery in slick detection has been proven in both previous studies and preliminary R&D analyses (MODIS imagery) before the PRIMI project, which have demonstrated that slicks are visible in high resolution top of atmosphere (TOA) reflectance imagery, in qualitative/visual terms. This capability constituted the starting point and was part of the prototypal operator-assisted PRIMI system. On the other hand, the quantification of oil-water contrast in order to develop detection techniques was one of the main R&D challenges and innovations of the work of this thesis and contributed to develop the first integrated radar-optical observing system for monitoring oil spill discharges operationally tested by the PRIMI project. The passage from image inspection, relying on human operator skills, to more objective and automated detection procedures will be explored in this thesis by combining the spectral signatures of the various available MODIS and MERIS products. The ocean colour image processing and analysis for oil spill detection is also strongly innovative since present algorithms on oil slick detection for MERIS and MODIS data are lacking. The field is indeed new: only recently ocean colour data spatial resolution has reached values (250-300 m) compatible with the detection of the more frequent, smaller illegal discharge oil slicks (100 m - 1 km), which are the most serious threat to the marine environment, from the oil pollution standpoint.

This thesis presents a new oil spill detection methodology, which makes use of MODIS and MERIS L1B satellite TOA reflectance imagery, for the first time in a highly automated way. In Chapter 1, we overview the general state of marine oil pollution, with particular regards to the Mediterranean sea and introduce the use of space-borne sensors in terms of their usefulness as operational monitoring systems in oil pollution (Chapter 1). In Chapter 2, we describe the basic physical principles which were taken into account to establish the applicability of optical satellite data to oil detection and to build the new methodology. The ocean colour data treatment developed in this thesis is presented in details in Chapters 3 and 4. It will consist in the implementation of new procedures to construct specific products obtained by combining relevant existing L1B and L2 products in the various optical bands. These new procedures are directed to both enhance oil-water contrast and substitute standard existing procedures (e.g. atmospheric correction), which otherwise would flag pixels invested by oil slicks. New methods will be presented to eliminate oceanic and atmospheric natural variability from input images (image flattening) in order to enhance slick-clean water contrast (Chapter3). In Chapter 4, we present a specific clustering technique. This is necessary to group oil spill signatures with similar reflectance into clusters, i.e. regions with common mode reflectance values. To distinguish between oil spill and look-alike clusters, we apply to each cluster region a set of *"slick*

features parameters" determined analyzing a set of reference oil spills observed *in situ,* constituting the oil spill (OS) database built during the thesis work. Finally, we define a score look-up table which relay on optical characteristics of oil. This is used to classify an oil spill candidate and to define its probability to be a spill (Chapter 4). The evaluation of the developed algorithm was made using a set of certified OS cases in the OS database, in order to cover as many oil spill types and illumination-view situations as possible. This allowed to quantify the capability and limits of the developed algorithm (Chapter 5). Summary and conclusions resume the main results obtained during the thesis and discuss the possibility to improve the capability of the pruning parameters to eliminate look-alikes. Finally, appendixes introduce the basic concepts of ocean remote sensing and discuss some technical aspects of ocean colour sensors, introducing MODIS and MERIS, and the practical processing steps to manage satellite data.

Chapter 1

Marine Oil Spill Pollution: Towards A Definition Of An Operational Monitoring System

This chapter presents the state of the art of oil spill monitoring and detection at sea by the use of satellite remote sensing. We first overview the general state of marine oil pollution, with particular regards to the Mediterranean sea. We then introduce the use of space-borne sensors in terms of their usefulness as operational monitoring systems in oil pollution. We conclude with the presentation of the first Italian project for oil spill monitoring (PRIMI), introducing the optical observation module, based on MODIS and MERIS imagery, whose implementation is the objective of this work.

1.1 Operational pollution in the Mediterranean Sea

The Mediterranean basin is the major route for oil transportation between East and West. Tankers enter or exit the Mediterranean Sea through the Suez Canal, the Black Sea and the Strait of Gibraltar. There are about 40 oil-related sites (i.e., pipelines, terminals, refineries, offshore platforms etc.) distributed along the coastal zone, from and to which an estimated 0.55 and 0.15 billion metric tons, respectively, of crude oil and petroleum products are annually loaded, unloaded and transported by oil tankers (Pavlakis *et al.*, 1996). The main tanker traffic flows in the East-West direction. The most important oil traffic lane (an estimated of 90% of total oil tanker traffic) (REMPEC, 2002) connects Suez Canal and the Sidi Kerir terminal of the Sumed pipeline (also known as Suez-Mediterranean pipeline) in Egypt with Gibraltar, passing between Malta and Sicily Channel, and following the coasts of Tunisia, Algeria and Morocco. The traffic on this main axis reduces gradually as it moves westward and branches off towards unloading terminals in the Adriatic Sea,

Ligurian Sea, Gulf of Lion, Corsica and Spain, resulting to be hot spots areas. Figure 1.1 shows the map of tanker shipping routes in the Mediterranean Sea, each one associated with its own quantity of oil transported (LMIU, 2001). The second important oil traffic route starts from the loading terminals in the Eastern Mediterranean (in Syria and in the Gulf of Iskenderun in Turkey) and after passing Cyprus joins the main axis. The third major route connects loading terminals in the Black Sea with the main East-West axis, passing through the Istanbul Straits, Sea of Marmara, Çanakkale Straits, and the Aegean Sea.

Taking into account that the total amount of oil transported by sea in 2000 (REMPEC, 2002) was estimated at approximately 1.715 million of tons and that the estimated volume of oil (crude oil and refined products) that was carried by sea in the Mediterranean was put in 1999 at some 360-370 million tons annually, it appears that approximately 20-25% of the oil globally transported by sea crosses the Mediterranean Sea. Further, up to some 600.000 tons of oil and oily waters are spilled at sea every year due to operational pollution (REMPEC, 2002).

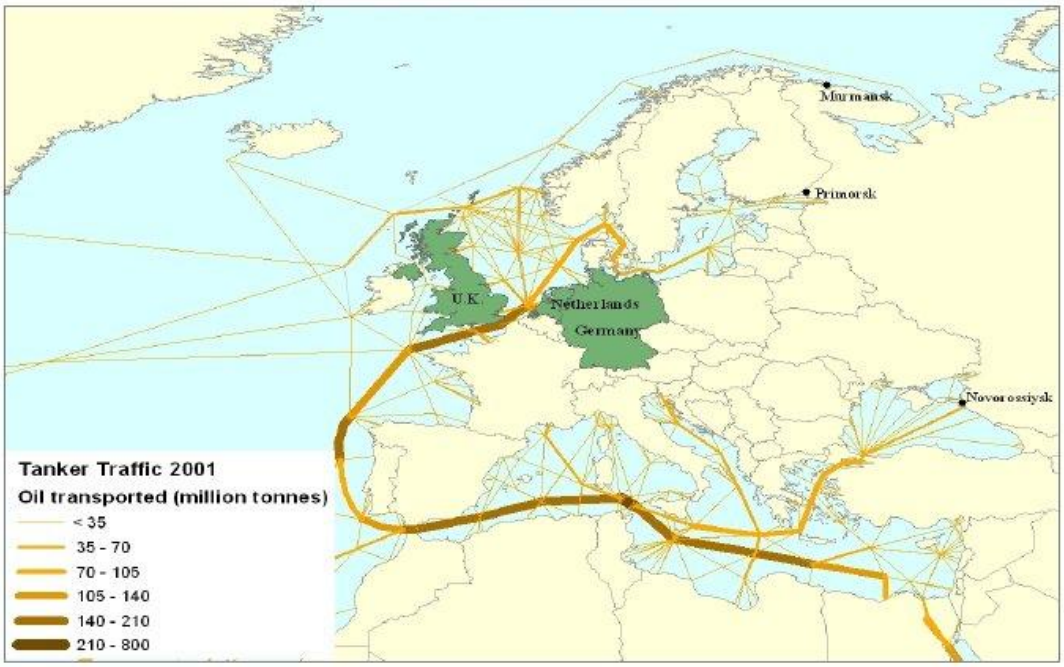

Figure 1.1 Map of tanker shipping routes in Europe, (LMIU, 2001)

Recent studies on oil spill long-term monitoring carried out by the *European Commission-Joint Research Center* (*JRC*) (Bernardini et al., 2005; Ferraro et al., 2006a,b; Pavalakis et al., 2001; Tarchi et al., 2006; Topouzelis et al., 2006), based on the analysis of a large number of SAR images, detected a significant number of *possible spills* in the Mediterranean sea, producing a mapping for the years 1999-2004. The presence of oil at sea has not been validated by aerial or vessel surveillance. For this reason is used the term

"possible oil spills". In total 18,947 SAR images were analyzed and 9299 possible oil spills were detected from 1999 to 2004. Table 1.1 summarizes the results obtained for the whole Mediterranean.

Year	Coverage (square degrees)	Possible Spills
1999	1382	1638
2000	3642	2297
2001	2495	1641
2002	1840	1401
2003	2289	897
2004	3885	1425

Table 1.1 Yearly coverage and possible oil slicks detected over the whole Mediterranean basin in the period 1999-2004.

The cumulative results as a point-like map and the corresponding coverage of analyzed images for the same period are displayed in figure 1.2 and 1.3. The majority of spills are located beyond the 12 nautical miles limit of territorial waters, probably indicating deliberate intention to avoid risks of legitimate actions within the area of jurisdiction of the coastal states. Oil spills have been identified in archive images and then compared to the total number of satellite images analyzed, because the presence of oil at sea couldn't be validated *in situ*. Figure 1.4 displays the oil spill density as obtained by merging the information from the two previous maps, i.e. by normalizing the number of observed possible oil slicks in a given area with the total number of observations available for that area. Such a procedure basically removes any bias effect and accounts for uneven coverage of the area. Similar studies were performed for the Black Sea, during the period 2000-2004: 3125 SAR images analyzed and 1227 possible oil spills detected (figures 1.5 and 1.6).
These maps let us to understand the spatial distribution of possible oil slicks and to identify hot spot areas. It is evident how the spills distribution appears highly correlated with the major shipping routes (figure 1.1). Concentrations appear in the Ionian and Adriatic Sea, along the African coasts through the Sicily Channel up to the Aegean Sea, and the Northern Tyrrhenian Sea, along the Ligurian Sea, the Gulf of Lion and the east part of Corsica. All over the region, however, the spills show considerable spatial dispersion.

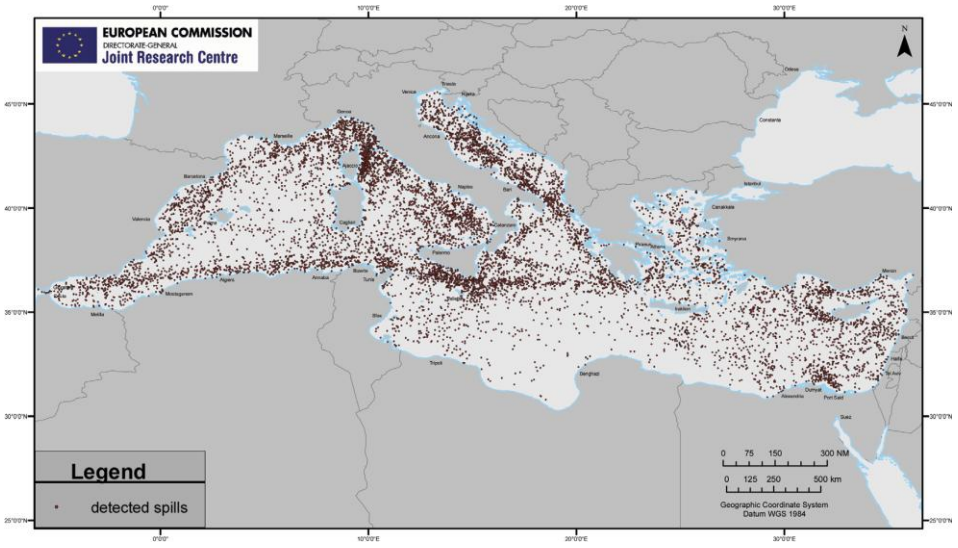

Figure 1.2 Possible oil spills detected in the period 1999-2004 in the Mediterranean sea.

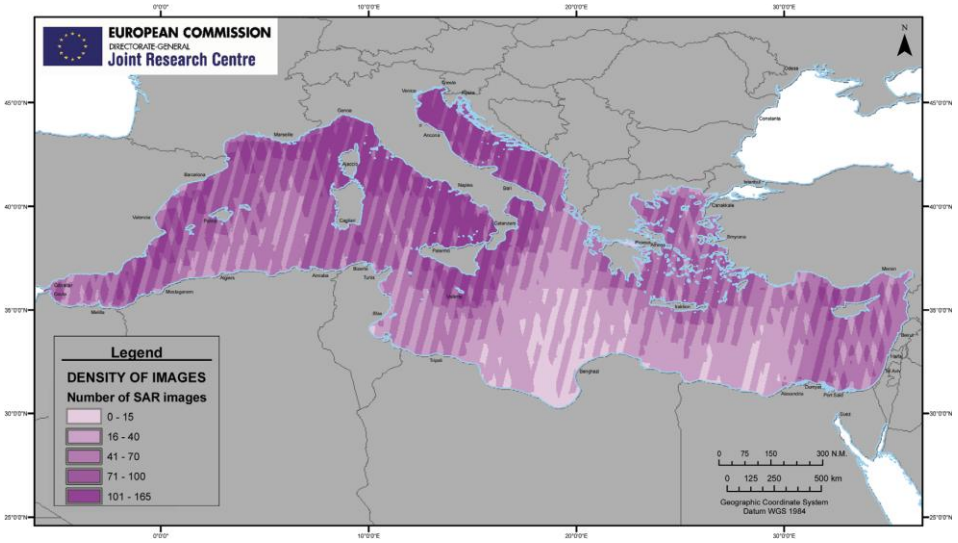

Figure 1.3 Coverage of SAR images available for the period 1999–2004.

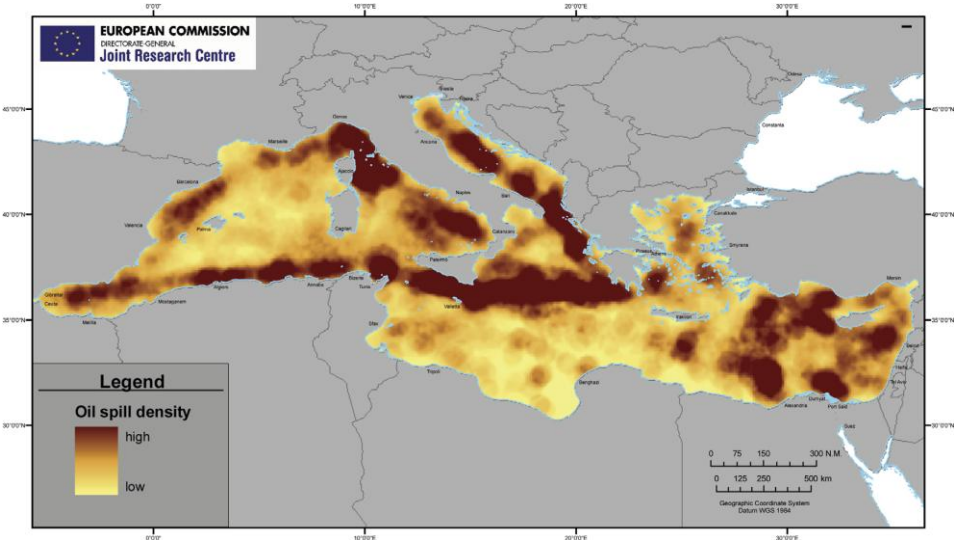

Figure 1.4 Oil spill density for the Mediterranean sea for the period 1999-2004.

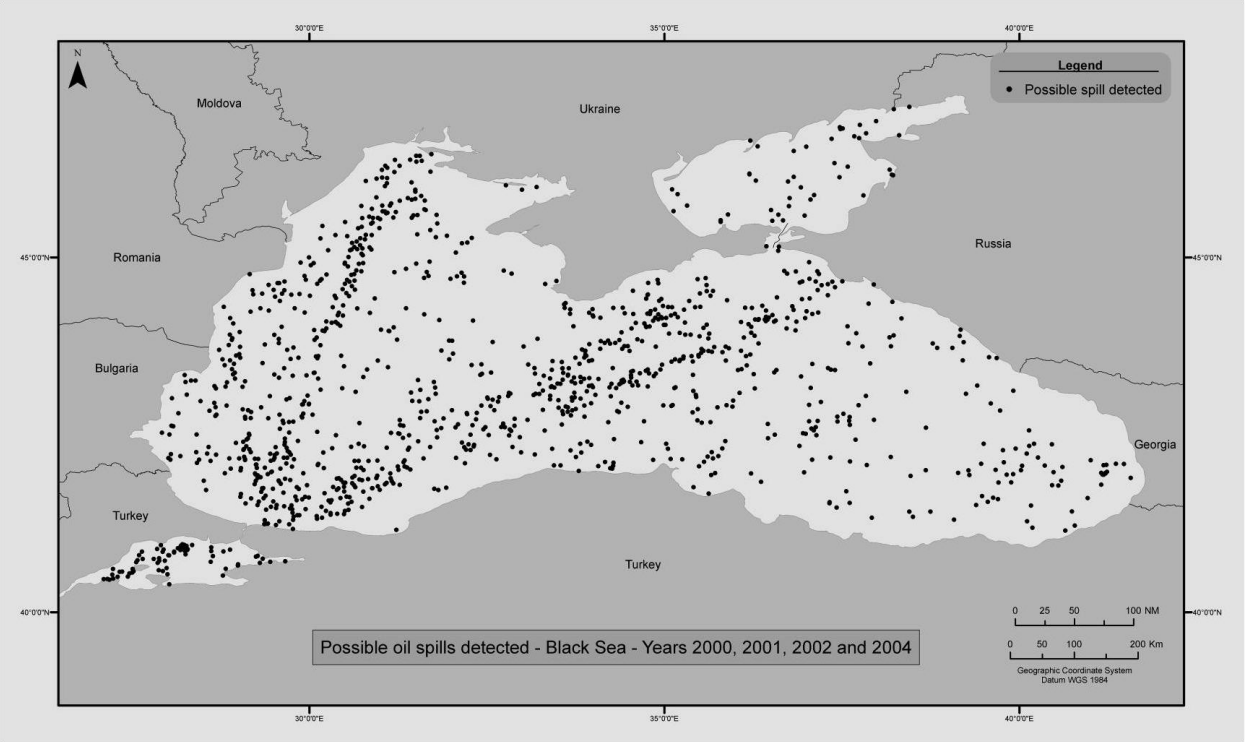

Figure 1.5 Black Sea Oil Spill Analysis: 3125 SAR images analyzed and 1227 possible oil spills detected during the period 2000-2004.

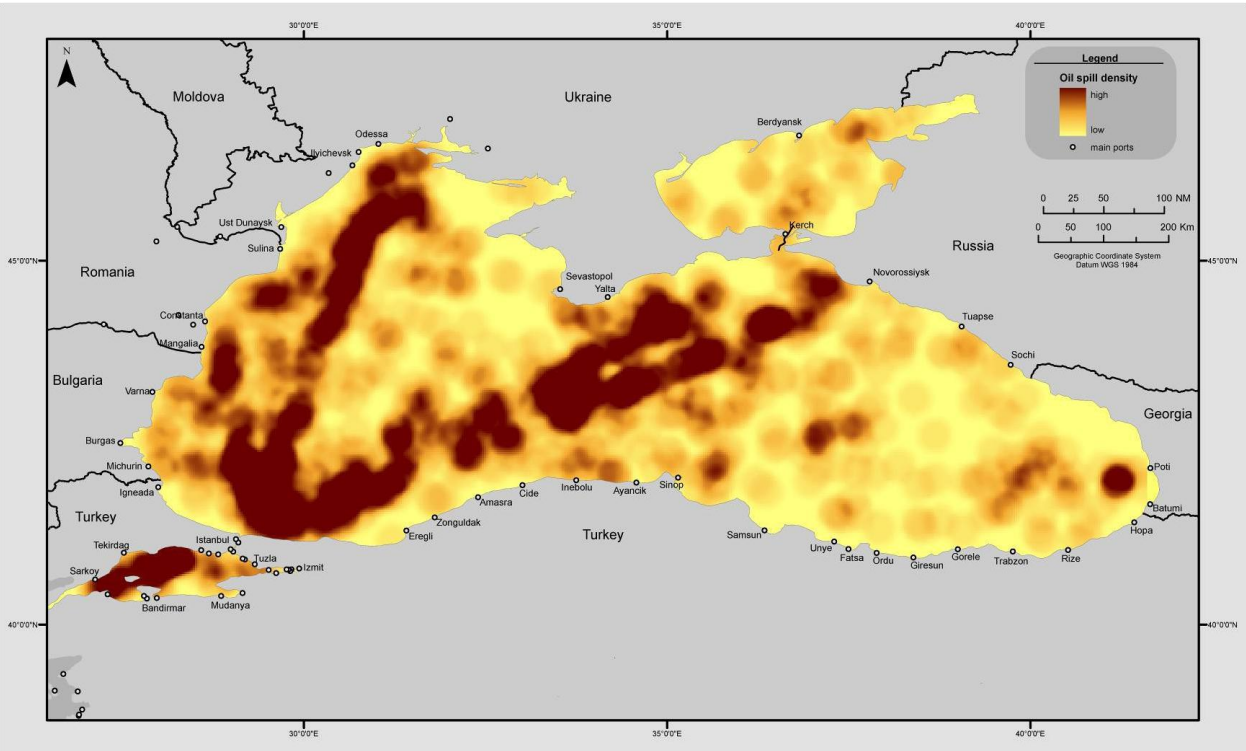

Figure 1.6 Black Sea OS Analysis: OS distribution (2000-2004).

In the framework of the mapping activities carried out at JRC, we report the case study of the Adriatic sea for the development of the AESOP (AErial and Satellite surveillance of Operational Pollution in the Adriatic Sea) project (Ferraro *et al.*, 2007), as area of special interest, for the same period (1999-2004). The Adriatic basin is crossed by main traffic lines. They include routes to important oil terminals and oil refineries as well as intense ferries line traffic, showing thus an enhanced sensitivity to pollution. The Adriatic Sea covers in total an area of approximately 1537 square degrees. Specific analysis of the oil spill density distribution and evolution has been carried out over the area (Bernardini et al., 2005; Tarchi et al., 2006). In total, in the period 1999–2004, the satellite images analyzed in the Adriatic Sea cover an area of 1520 square degrees and 1049 possible oil spills were detected (figure 1.4).

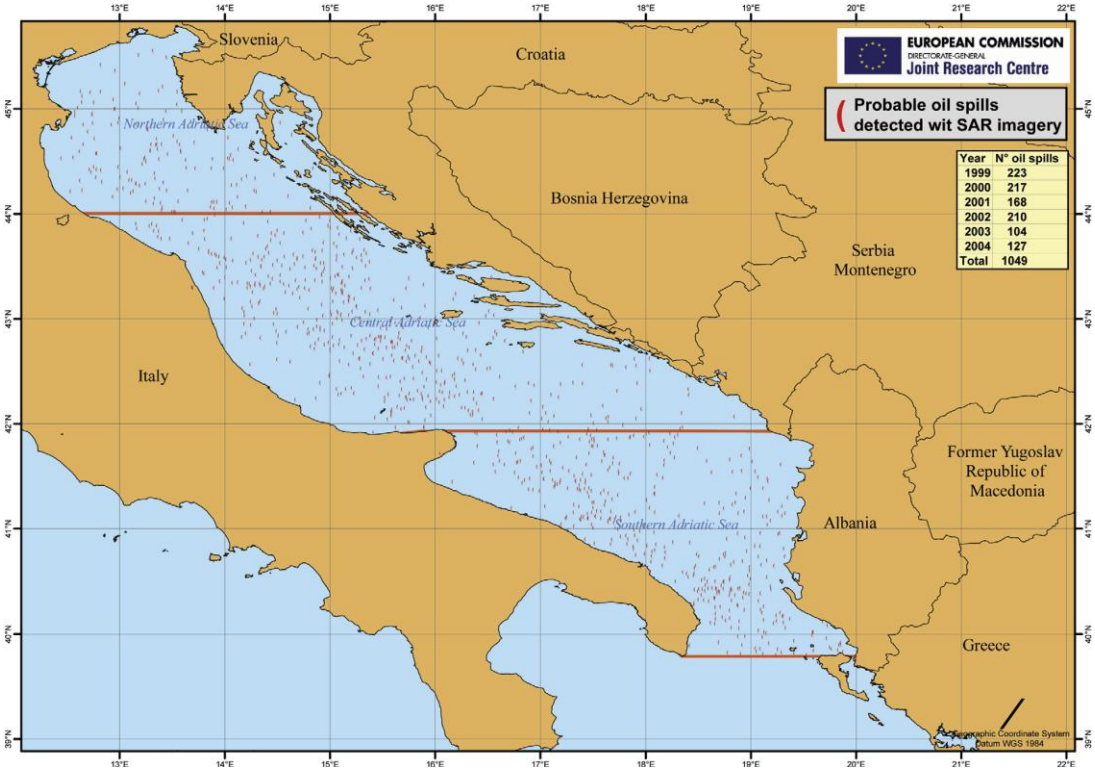

Figure 1.4 Possible oil spills detected in the period 1999-2004 in the Adriatic Sea (Ferraro *et al.*, 2007).

Thus, considering the oil spill distribution in the Mediterranean Sea, taking into account how frequent such spillages occur (that up to 600.000 tons of oil are spilled every year due to illegal operations), and the distinct hydrological and ecological characteristics of the basin, as well as its extensive coastline (45,000 km) and high concentration of specially protected areas, the situation in the Mediterranean Sea is of significant concern.

Surveillance activities on maritime traffic and sea pollution are generally achieved by local authorities by means of ships and aircrafts. For example, the *Italian Coast Guard* is responsible for naval and aerial maritime surveillance, providing a fleet of more than 300 ships and several aircrafts. This kind of surveillance is however too much limited for the definition of an operational monitoring system, because of the impossibility to provide continuous spatial and temporal coverage of wide areas. In this context, satellites can play an important complementary and supporting role to naval and aerial surveillance, in detection and deterring of pollution at sea. In the last decade, the use of remote sensing data for maritime surveillance and sea based oil pollution monitoring of wide geographic areas has been successfully demonstrated. We may recall as a first series of projects those funded by the European Commission, such as AESOP (AErial and Satellite surveillance of Operational Pollution in the Adriatic Sea) (Ferraro *et al.*, 2007), RAMSES (Regional earth observation Application for Mediterranean Sea Emergency Surveillance), VASCO (Value Added provision for Slicks and hazardous Cargoes Operational detection) and CLEOPATRA (Chemical Effluent and Oil Pollution Alert and TRAcking). These projects explored the possibility of setting up an operational system based on the use of NRT space-borne imagery to support and integrate aerial surveillance in the detection of oil pollution and in the monitoring of main shipping routes in the Mediterranean region. More recently, the set up of the *European Maritime Safety Agency* (EMSA), created in the wake of the *Erika* and *Prestige* oil tanker accidents, was one of the key European level initiatives aimed at improving the enhancement of the overall maritime safety system within the Community. EMSA manages a SAR satellite-based monitoring system for marine oil spill detection and surveillance in European waters (CleanSeaNet). This service provides a range of detailed information including oil spill alerts to Member States and rapid delivery of available satellite images and oil slick position.

1.2 Satellite sensors for oil spill detection

Satellite sensors are here reviewed and evaluated in terms of their usefulness in responding to oil spills. The discussion of the sensors is divided into two main categories, namely active and passive. Active sensors are those that provide their own source of illumination or excitation in the microwave region, whereas passive sensors rely on illumination from solar radiation and Earth emission, in the visible, infrared and microwave regions. As regards the observation of the sea from space, sea surface properties such as color, reflectance, temperature and roughness can be remotely sensed. The necessary condition for oil to be remotely sensed is when one or more of these properties are modified.

The ability to detect and monitor spills is determined by several factors, such as the characteristics of the sensor (sensing angle, sensor footprint, resolution, observing frequency, bandwidth, sensing distance, etc.), solar zenith angle during sensing, type and composition of the spilled oil, meteorological conditions and oceanic state during the spill, chemical reaction and mixing with the surrounding water and duration of the spill in the water. All these factors contribute to the complexity for remote detection of oil spills. Remote sensing technology has provided the capability for early detection, monitoring, and tracking of oil spills, and successful results have been largely documented. Techniques to detect oil spills are summarized in Brown *et al.*, (2001-1998), Fingas and Brown (1998-1997), Sherman (1992) and Lodge (1989).

Of primary use in oil spill detection is the *Synthetic Aperture Radar* (SAR). SAR capabilities are widely well demonstrated (Brekke & Solberg, 2005) and thus it still turns out to be the most efficient and superior satellite sensor in oil spill detection. SAR is particularly useful for *its all-weather* and *all-day* capability, that is in observing the sea at night and at cloudy weather conditions. For this reason, it is often preferred to optical sensors. However, SAR has some limitations, as the presence of natural phenomena that can give false oil spill detections (*look-alikes*), such as phytoplankton, rain cells and fresh water slicks, very difficult to distinguish. In addition, SAR is only applicable for oil spill monitoring in a certain range of wind speeds and does not have capabilities for oil spill thickness estimation and oil type recognition. Furthermore, SAR data are expensive, not available daily (long revisit time, several days) and cover small areas (reduced swath, 100-500 km), as shown in table 1.2. These limitations do not provide spatial and temporal coverage for a systematic monitoring activity.

Optical sensors also have showed potential in oil spill detection, although their operational use was mainly carried out on board aircrafts. An example is the laser fluorosensor, an useful instrument for its unique capability to identify oil on water, but used only on aircrafts and useless due to its large size, weight and high coast. Unlike SAR, the use of visible techniques was generally restricted to that of documentation because of the lack of a positive oil detection mechanism, due to no specific spectral characteristics that can distinguish it from the background (Brown & Fingas, 2001; Fingas & Brown, 1998-1997; Brown *et al.*, 1998/1996). Further, the coarse spatial resolution of past sensors (~ 1 km), cloud cover interference and daily visibility, have contributed to their limitation. However, in the past few years, optical sensors have provided useful imagery for a large number of oil spill events. Passive microwave and thermal infrared sensors have been studied for several years, providing the potential as all-weather (the former) and all-day (the latter) oil sensors, but many commercial instruments lack sufficient spatial resolution to be practical and

operational. Only in recent years, with the new generation of optical sensors (i.e., MODIS and MERIS), thanks to the increased spatial (250-300 m) and spectral resolution, a forward step has been done. They also provide wide swaths, daily revisit time and data free (table 1.2). Table 1.2 summarizes main sensors, active and passive, together with their resolution, swath, revisit time and repeat cycle, commonly used in oil spill detection.

Sensor (Agency)	**Resolution (m)**	**Swath (Km)**	**Revisit Time (days)**	**Full-earth repeat cycle (days)**
		Radar		
ERS-1 (ESA)	30	100/500	3	35
ERS-2 (ESA)	30	100/500	3	35
Radarsat-1 (CSA)	10-100	50/500	2	7-17
Radarsat-2 (CSA)	10-100	50/500	2	7-17
ASAR (ESA)	25-150	450	7	
X-band SAR† (ASI)	15-100	40/200	6h (full constellation)	
		Optical		
Landsat (NASA)	15-120	185		16
SPOT	10	60/85	2-3	26
AVHRR (NOAA)	1100	2700	1	12h
MODIS† (NASA)	250-1000	2330	1 1/2	1
MERIS† (ESA)	300-1200	1150	3	4-5

Table 1.2 Satellite sensors mainly used in oil spill detection.

X-band SAR (on board of Cosmo-SkyMed constellation, fully operative since 2010), MODIS and MERIS sensors, marked with a cross in table 1.2, are the newest generation sensors and do not yet have a proper documentation as oil spill detectors.

In summary, SAR is still the most efficient and superior satellite sensor for oil spills detection, particularly for its high resolution and for observing the sea at night and at cloudy weather conditions, though it does not have capabilities for oil spill thickness estimation and oil type recognition. Optical sensors, despite their limitations (cloud cover and daily

visibility), can play an important complementary and supporting role in detecting and monitoring oil pollution, together with SAR images.

1.2.1 Detection of oil spills by SAR sensors

SAR sensors have provided useful imagery for a large number of marine oil spills and several studies on oil detection algorithms has been ongoing for more than a decade. Most of these examine the ability of several algorithms and techniques to detect oil spills using SAR data (Brekke & Solberg, 2004; Ferraro *et al.*, 2007; Solberg and Theophilopoulos, 1997; Solberg *et al.*, 1999; Del Frate *et al.*, 2000; Espedal and Wahl, 1999; Espedal and Johannessen, 2000; Fiscella *et al.*, 2000; Pavalakis *et al.*, 2001; Topouzelis *et al.*, 2002; Karathanassi *et al.*, 2007; OCEANIDES project; Benelli & Garzelli, 1999; Barni et al., 1995;). SAR sensors emit their own energy in the microwave range, which is then reflected from the sea surface and received back at the sensor. A radar image is a representation of the backscatter return and is mainly proportional to the surface roughness at the scale of the radar wavelength (few centimeters). The main agent of radar backscattering are the *wind-generated short gravity-capillary waves*. These capillary waves reflect radar energy producing a "bright" area in radar imagery known as sea clutter. The possibility of detecting an oil spill in a SAR image relies on the fact that the oil film has a dampening effect on these waves and decreases the backscattering of the sea surface resulting in a dark feature that contrasts the brightness of the surrounding spill-free sea. Figure 1.5 gives two examples.

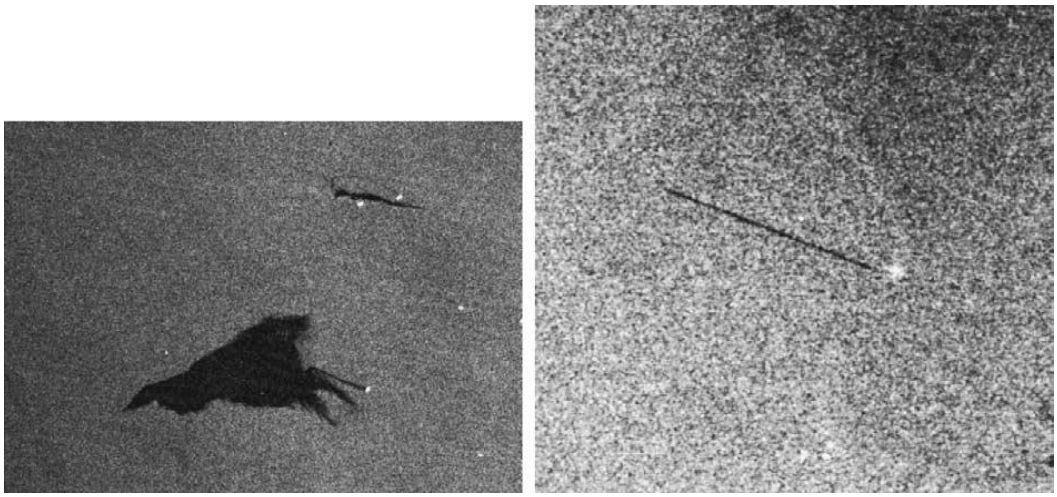

Figure 1.5 Left: RADARSAT-1 ScanSAR image (30th of July 2002) containing two oil spills on an homogenous background. Right: ENVISAT ASAR image (24th of July 2003) containing a linear oil spill.

The wind intensity drastically influences the backscatter and the visibility of slicks on the sea surface. A minimum wind field of 2–3 m/s creates sufficient brightness in the image

and makes the oil film visible. On the other end, when the wind speed is too high, greater than 7-10 m/s, it causes the spill to disappear. First, because the short waves receive enough energy to counterbalance the dumping effect of the oil film. Then, when the sea-state is fully developed, the turbulence of the upper sea layer may break and/or sink the spill or a part of it. As a consequence of the above brief discussion the identification of an oil spill in a SAR image includes always as first and basic step the detection of dark features. Typically, a SAR image may show several dark features that are not oil spills (Bern *et al.*, 1993; Wahl *et al.*, 1993), in most cases due to both meteorological and/or oceanographic effects (i.e., fresh waters slicks, wind slicks, chlorophyll, algal blooms, ice etc..). These look-alike features pose a fundamental problem to the identification of oil spills and the analysis procedure must include a discrimination phase.

The standard methodology used for oil spill detection in SAR images can be divided in (Indregard *et al.*, 2004):

- Detection of slicks by automatic algorithms;
- Manual verification of the slicks (oil/look-alike) and assignment of confidence levels.

Inspection by experienced operators is necessary to validate the outputs of the algorithms, especially in an operative context. A framework for oil spill detection algorithms can be resumed with the one in figure 1.6.

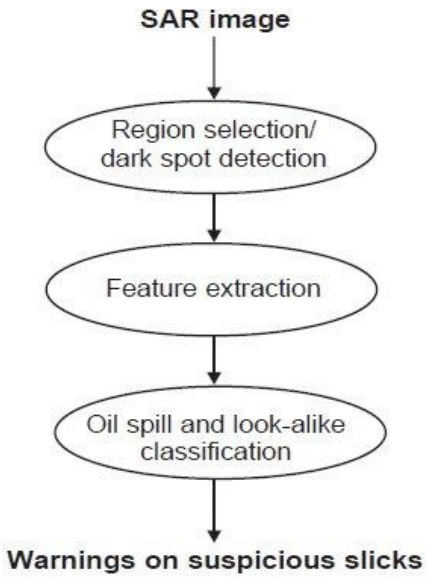

Figure 1.6 Representative framework for oil spill detection algorithms.

The basic steps of an identification's procedure (figure 1.6) can be described as follows:

1. Isolation and contouring of all dark signatures, through appropriate threshold and segmentation processing of the image;
2. Extraction of key parameters for each candidate signature, which usually are related to its shape, internal structure and radar backscattering contrast;
3. Test of the extracted parameters against predefined values, which characterize man-made oil spills, usually determined through phenomenological considerations and statistical assessments;
4. Computation of probabilities for each candidate signature. Features falling above a probability threshold are considered to be oil spill with associated a confidence level which is increasing with the corresponding probability. Alternatively, the confidence level can be defined in terms of peculiar characteristics of the identified feature. In this case high confidence spill are the feature having all the characteristics that a real spill usually exhibits in a SAR image.

The general approach can be also more sophisticated taking into account relevant environmental parameters having an impact on the spill shape, such as the time history of wind fields and currents (Espedal & Wahl, 1999).

Finally, it must be recalled that two main limits exist in the use of SAR images: the assessment of the quantity of oil and the identification of the polluter. Of great interest for the competent authorities, is the amount of oil represented by the spillage. However, an accurate estimation cannot be achieved, since it requires accurate knowledge of the spill thickness, which cannot be measured by SAR sensors. Moreover, satellites SAR images are unable to identify the pollution culprit (i.e. the name of the ship that polluted); satellite can at best identify the position of the probable pollution culprit.

1.2.2 Detection of oil spills by optical sensors

In the past, several studies on oil spill observability by optical sensors have been carried out. The slick from the *Ixtoc I* well blowout in Gulf of Mexico (1979) was detected using GOES (Geostationary Operational Environmental Satellite) and also by the AVHRR infrared sensor (O'Neil *et al.*, 1983). Tseng and Chiu (1994) examined the use and capability of the AVHRR sensor for the detection and monitoring of oil spills studying the spills in the Persian Gulf (Persian Gulf war, 1991). Several workers were able to detect the Arabian Gulf War spill in 1991 (Cross, 1992; Rand *et al.*, 1992; AI-Ghunaim *et al.*, 1992; A1-Hinai *et al.*, 1993). The massive Exxon Valdez slick (Alaska, 1989) was detected on SPOT (Satellite Pour l'Observation de la Terre) satellite data (Dean *et al.*, 1990). Oiled ice in Gabarus Bay

resulting from the Kurdistan spill was detected using LANDSAT data (Dawe *et al.*, 1981; Alfoldi & Prout, 1982). The Haven spill near Italy was also monitored by satellite (Cecamore *et al.*, 1992). A spill in the Barents sea was tracked using an IR band on NOAA 10 (Voloshina & Sochnev, 1992). Most recently, *Hu* (Hu *et al.*, 2003) demonstrated the detectability of oil spill with MODIS imagery, by an example from Lake Maracaibo, Venezuela, in the visible and near-IR range. Clear images of the spills in Lake Maracaibo were captured by MODIS, during the period 2002-2003, as that showed in figure 1.7. Kostianoy *et al.*, (2006), compared ASAR ENVISAT and RADARSAT images with AVHRR and MODIS images during a monitoring period (2004-2005) of oil pollution in Southeastern Baltic Sea. Optical sensors have thus provided their capabilities in oil spill observability, but yet they lack of detection algorithms.

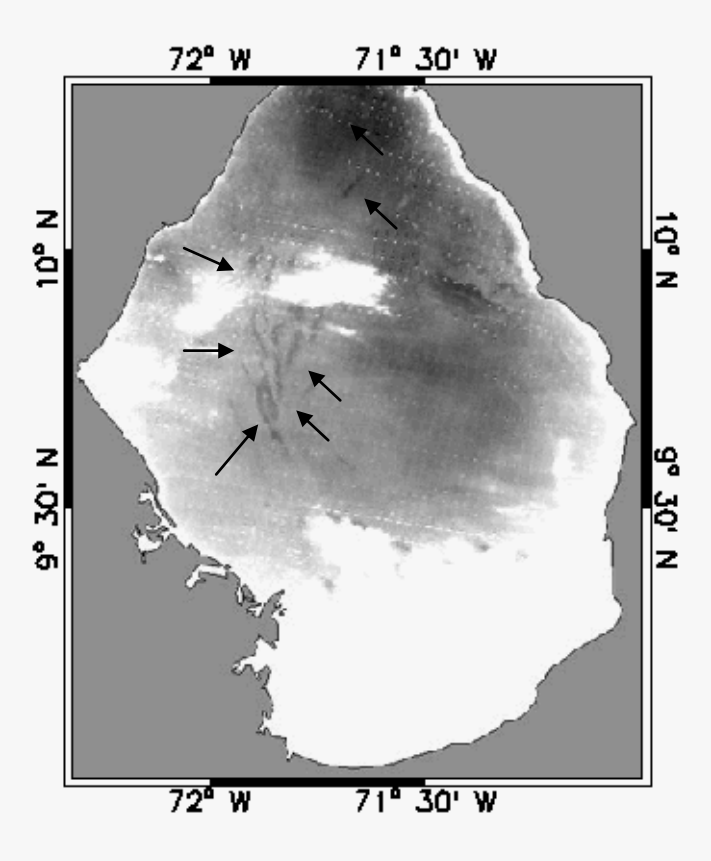

Figure 1.7 MODIS image (16/01/2003, band 859 nm) showing oil spills in Lake Maracaibo (Hu *et al.*, 2003). Major slicks are marked with arrows. White color represents clouds or extreme turbidity near the coast.

Optical sensors measure the solar irradiance being reflected by the sea and the radiance emitted by the sea surface itself, within the visible, infrared (IR) and microwave spectral windows. The radiation that have interacted with or being emitted from the sea surface, influenced by the optical processes in the surface layer of water, carries the

oceanographic information from the sea to the sensor. Thus, the presence of a floating oil film will modify the radiance leaving the sea surface (water-leaving radiance). The mechanism of this phenomenon mainly depends on the optical properties of the sea surface and of the oil film (i.e., absorption and scattering coefficients), which in turn depend on sea state (wind and waves) and on the zenith angle of the incident light and of satellite. We give a more detailed discussion on oil remote sensing in paragraph 2.4. Here we say that, to be detectable, an oil spill should have a spectral signature (in the visible and/ or in thermal range) and a significant contrast with its background.

Ultraviolet (UV) and passive microwave sensors (MWR) technology is currently used to detect oil spills (Fingas & Brown, 1997), but finds application only on board aircrafts and are not yet present onboard satellites. In the UV range oils absorbs light and become electronically excited. This excitation is rapidly removed through the process of fluorescence emission, primarily in the first part of the visible region of the spectrum. Fluorescence is a strong indication of the presence of oil since very few other compounds show this tendency. Natural fluorescing substances, such as chlorophyll, fluoresce at sufficiently different wavelengths than oil to avoid confusion. Chlorophyll yields a peak at 685 nm, while fluorescence response of crude ranges from 400 to 650 nm with peak centers in the 480 nm region. As different types of oil yield slightly different fluorescent intensities and spectral signatures, it is possible to differentiate between classes of oil under ideal conditions (Brown *et al.*, 1994 a,b; Fruhwirth *et al.*, 1994; Hengstermann and Reuter, 1990; Balick *et al.*, 1997). In the microwave range, oil slicks emit stronger radiation than the water and appear as bright objects on a darker sea. The emissivity factor of water is 0.4 compared to 0.8 for oil (O'Neil *et al.*, 1983; Ulaby *et al.*, 1986). A passive microwave device can detect this difference in emissivity and could therefore be used to detect oil. In addition, as the signal changes with thickness, the device could be used to measure thickness. Zhifu *et al.*, (2002), did some experiments using airborne (AMR-OS) and a ship borne (K-band) MWRs looking at various oil types and thickness. They found that MWRs are useful tools for measuring the thickness and estimating the volume of the spills, but the resolution is not fine enough to give accurate results.

Oil absorbs solar radiation and re-emits a portion of this radiation as thermal energy primarily in the 8-14 μm region. According to Fingas and Brown (1997), an oil layer on the surface of the sea may appear to be at a different brightness temperature with respect to the surrounding sea water. Due to its thermal inertia, lower than sea water, oil polluted areas can become warmer than the surrounding water in daytime, the opposite during night. In particular, in infrared images, thick oil appears hot, intermediate thickness of oil appear cool and thin oil os sheens are not detected. The thickness at which these transitions occur

are poorly understood, but evidence indicate that the transition between the hot and cold layer lies between 50 and 150 μm and the minimum detectable layer is between 10 and 70 μm (Fingas & Brown,1997). Thick oil films essentially act as absorbers of solar radiation and, on sunny days, appear to be hotter than the surrounding sea. But at night, the spill can appear cooler than the surrounding sea since it releases heat quicker than the surrounding water. Thin film can appear cooler due to a decrease in emissivity of the thin oil layer.

Optical techniques for detection and monitoring of oil spill are very recent (Grimaldi *et al.*, 2008/2009; Casciello *et al.*, 2007) and constitute first attempts in this filed. These methods explore the thermal infrared region (TIR) of optical sensors. Exploiting the relation between the spectral response (brightness temperature) and the thickness of oil films, Byfield and Boxall (1999) distinguished light from heavy oils by experimental optical data. Grimaldi *et al.*, (2008/2009), and Casciello *et al.*, (2007), presented a new technique for oil detection based on the general *RST* (Robust Satellite Techniques) approach, applied to AVHRR and MODIS observations in the thermal infrared region. The technique is based on a preliminary characterization of AVHRR radiances in normal conditions (unperturbed). This characterization can be done with the construction of a homogeneous multi-year data-set of co-located satellite images, collected for the same acquisition time and the same month of year. Thus, the presence of an oil polluted area will result in a variation on spectral signature compared to its unperturbed value. However, the proposed approach, which exploits the analysis of multi-temporal satellite records in terms of brightness temperature, finds hard applicability in oil spill detecting because of its sensitivity to the atmospheric conditions.

1.3 The PRIMI project and work area

PRIMI (Progetto Pilota Inquinamento Marino da Idrocarburi/Pilot Project Marine Oil Pollution) is a project funded by the Italian Space Agency (Nirchio *et al.*, 2009) for the development of an observation and forecasting system to monitor marine pollution from hydrocarbon oil spills in the Italian Seas. The system consists of four components, two of which for oil slick detection via multi-platform SAR and optical satellite imagery (SAR and Optical Module), an oil spill displacement forecast subsystem based on numerical circulation models (Forecast Module) and a central archive that provides WEB-GIS services to users (Archive Module). The system also provides meteorological, oceanographic and ship detection information. The PRIMI project has set up an oil spill monitoring system which, to our knowledge, for the first time integrates multi-platform SAR (ERS, ENVISAT, RADARSAT, COSMO-SkyMed) and optical (MODIS TERRA, MODIS AQUA and MERIS)

satellites into an Observation Module for OS detection in the seas around Italy (Ligurian, Tyrrhenian, Adriatic and Ionian Seas). The architectural design framework is schematically showed in figure 1.8. The system, working continuously in "surveillance" mode, utilizes satellite observational information as input to detect oil spillages and predict their displacement and transformation via its Forecast Module. The oil spill detection system (Observation Module) is based on the use of multi-platform SAR and optical data. The combination of SAR and optical satellites ensures a frequent revisit time of any Mediterranean area, as well as high resolution monitoring of the sea surface. The Forecast Module consists of a set of numerical circulation models, i.e. the Mediterranean Forecasting System (MFS, Pinardi, 2003), regional higher resolution forecasting systems for the Adriatic and Tyrrhenian Seas and the Channel of Sicily and an oil dispersion and modification model stemming from the MEDSLIK model (Lardner, 2006). The Archive Module stores observational and forecast data and a WEB-GIS system is accessible to end users, to which oil spill detection reports are also sent ("alert" mode).

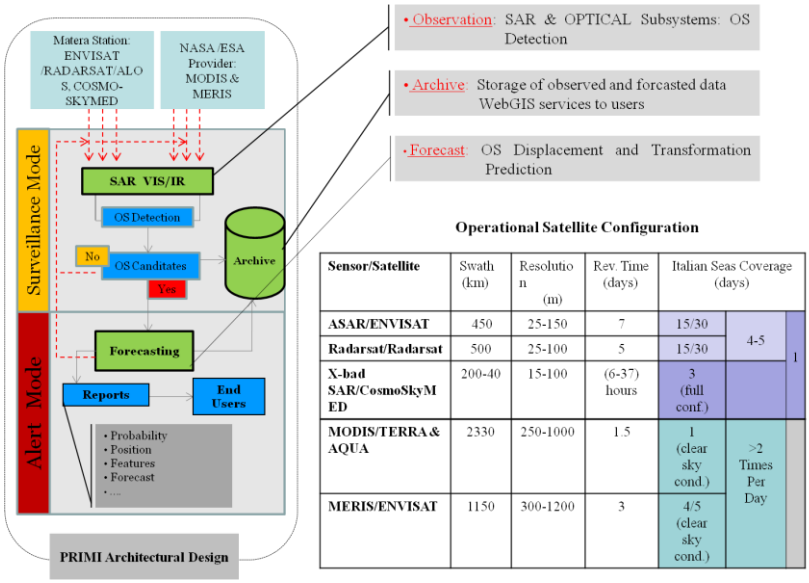

Operational Satellite Configuration

Sensor/Satellite	Swath (km)	Resolution (m)	Rev. Time (days)	Italian Seas Coverage (days)		
ASAR/ENVISAT	450	25-150	7	15/30	4-5	1
Radarsat/Radarsat	500	25-100	5	15/30		
X-bad SAR/CosmoSkyMED	200-40	15-100	(6-37) hours	3 (full conf.)		
MODIS/TERRA & AQUA	2330	250-1000	1.5	1 (clear sky cond.)	>2 Times Per Day	
MERIS/ENVISAT	1150	300-1200	3	4/5 (clear sky cond.)		

Figure 1.8 PRIMI schematic architectural design (left) and table of satellites used by the system.

The development of the Optical Observation Module, based on MODIS and MERIS high resolution imagery and used by the PRIMI system, is the objective of this work. The starting point is to investigate and understand how oil spills at sea can be remotely sensed by optical sensors in order to develop an automatic oil spill detection methodology. Then, the passage from image inspection, relying on human operator skills, to more objective and automated detection procedures will be the challenge explored in this thesis by analyzing and combining the spectral signatures of the various available MODIS and MERIS products.

Chapter 2

Methodology for Oil Spill Detection In Optical Imagery

This chapter introduces the basic physical principles of ocean remote sensing and the optical properties of hydrocarbons at sea in order to establish the applicability of optical satellite data to oil detection. We then present the methodology adopted for the development of the oil spill detection algorithm based on optical satellite imagery.

2.1 Oil spill remote sensing in optical imagery

To establish the applicability of optical satellite data to oil detection it is necessary understand what an optical sensor actually measures, the optical properties of hydrocarbons and the mechanisms of oil-radiation interaction. The principles of ocean remote sensing are described in detail in the appendixes. Here we briefly resume the physical principles and practical operation of passive radiometers operating in the visible and near-IR wavelengths, commonly referred to as *ocean colour* remote sensors, and how an oil spills can appear in an optical image.

2.1.1 Seeing through the atmosphere

The fundamental principle of remote sensing is the measure of electromagnetic (e.m.) radiation reflected and/or emitted from the observed sea surface. The e.m. radiation that have interacted with or being emitted from the sea surface carries the information from the sea to the sensor, as shown in figure 2.1. Information transfer however is limited because the radiation must pass through the Earth's atmosphere. The atmosphere is opaque to e.m. radiation at many wavelengths and there are only certain wavelength windows (visible, infrared and microwave) through which radiation may be fully (microwave) or

partially (visible and infrared) transmitted, rendering them useless for remote sensing. In those part of the spectrum where the atmosphere is transparent, the radiation passing through however may still be altered in various ways, through the processes of scattering and absorption. The atmospheric components, such as gas molecules, water vapours, aerosols and suspended particles, may absorb and/or scatter the radiation. If water droplets are present in the form of clouds, they may completely change the transmission properties of the atmosphere. The range of solar radiation in the visible and near-IR windows is between 0.3 μm and 3 μm, while, if the self emission of radiation by the sea is to be the means of remote sensing, the range is from 3 μm to 40 μm (thermal infrared) (see Appendixes A,B,C).

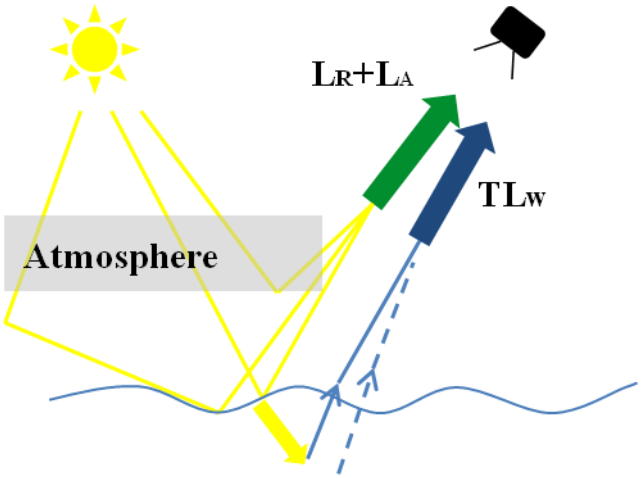

Figure 2.1 Optical pathways to an ocean colour sensor, grouped to facilitate atmospheric correction.

The top of the atmosphere radiance (TOA), i.e. radiance received by the sensor, is made up of various contributions, grouped in two components (Gordon 1978,1981): the atmospheric scattering radiance (L_R+L_A) and the water-leaving radiance (L_W). The atmospheric contribution is divided in two parts, that due to Rayleigh (molecular) scattering, L_R,, and that caused by aerosol particle scattering, L_A. This distinction is due to the fact that molecular composition of the atmosphere is generally uniform and well known (easy to model), whilst aerosols are variable in space and time (difficult to predict). The water-leaving radiance, L_W, is the signal from the sea. If L_S represents the total radiance to the sensor, we can write:

$$L_S = L_A + L_R + T\,L_W,$$

where T is the atmospheric *transmittance*, i.e. the proportion of radiation passing through the atmosphere. The most crucial step in the whole of the data processing scheme for any ocean colour sensor is the estimate of the water-leaving radiance, the useful signal, from the measured top of atmosphere L_S. This procedure is called atmospheric correction and consists in obtaining L_A and L_R, from which L_W can be determined (see Appendix E).

2.1.2 Oil spill optical properties

Let's see now how an oil film floating on the sea surface can affect the signal to the sensor. According to Byfiel (1999) and Otremba, an oil film on the sea surface impacts the conditions of the radiance field forming in the water as well as the water-leaving radiance. The mechanism of this phenomenon depends to a large degree on the optical properties of the sea surface and of the oil film, i.e. absorption and scattering coefficients. Moreover, these functions depend on sea state (wind and waves), oil thickness and incident light zenith angle (either for downwelling and upwelling radiance). Crude and heavy refined oils have three optical properties which vary slightly from oil to oil, and which make them detectable at sea by optical sensors (Byfiel, 1999):

- Their refractive index is greater than that of seawater, typically from 1.57- 1.67 in the UV to 1.48-1.52 in the visible, compared to a seawater refractive index of about 1.34;
- Their absorption coefficients are several orders of magnitude greater than that of water in the blue and decay exponentially with wavelength;
- They fluoresce when subjected to ultraviolet natural radiation, with fluorescence peaks that vary in width and wavelength position according to oil type and decay exponentially towards the red and near-infrared (NIR).

To determine how these characteristics contribute to optical oil-water contrast in remotely sensed data, it is necessary to examine how a layer of surface oil modifies upwelling radiance above the sea surface. Fig. 2.2 shows the contributions to the radiance measured above an oil slick, as seen by an optical sensor. Atmospheric path radiance, A, should be removed by atmospheric correction. Water-leaving radiance, C, is the proportion of incident light transmitted through the oil surface and scattered back up to the sensor. Surface oil modifies this in two ways, by reducing transmittance through the air-oil interface and by absorption within the oil layer. This will result in negative oil-water contrast. Oil fluorescence, D, due to ultraviolet radiation, contributes significantly in the first part of the visible range. Fluorescence peak is centered in the 480 nm region. In heavier oils with high absorption coefficients, this contribution is low. Specular reflection of sky radiance, B, is greater from an oil covered surface due to the higher oil refractive index. At near nadir

viewing angles, the reflection coefficient of oil is 3-5%, dependent on oil type, compared to 2% for seawater. This rises to 8-10% for oil and 6% for seawater at θ = 60°.

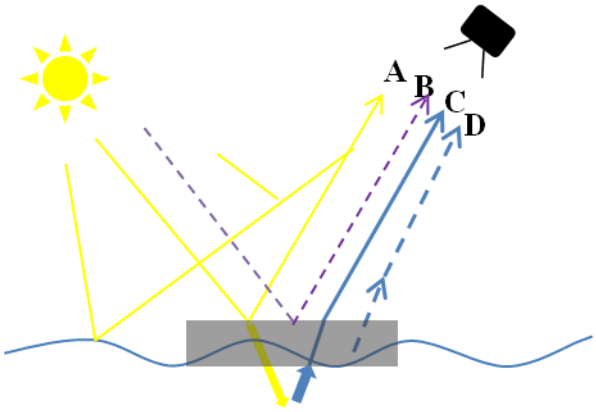

Figure 2.2 Contributions to radiance measured by an optical sensor above an oil-covered sea surface.

2.1.3 Model results on oil spill detectability in the visible spectrum

Otremba and Piskozub, (Otremba 1994-2009), provided theoretical results on the observability of floating oil film on the sea surface on the visible e.m. range. Modeling the water-leaving radiance (C arrow in figure 2.2) and the optical contrast between oil and surrounding clean water, demonstrate that there is a reflectance contrast between an oil film on the sea surface and background water so that the oil film can be detected under appropriate solar/viewing geometry and wind speeds. In general, when sea surface is flat, the contrast is always negative since the light intensity of water leaving radiance decreases. On the other hand, roughness of the sea surface results in the occurrence of positive contrast. The contrast value is influenced by the incident light factors, the sea state and the observation direction. As a rule, when observing the surface from the vertical direction, even a small surface roughness results always in a positive contrast value. The contrast is most pronounced when the observer/sensor sees the oil slick close to the sun reflection (positive contrast) and when the slick is observed at a low angle, almost horizontally (negative contrast). Of course, in the former case the contrast may be observed only off the actual sun glitter region. Several situations can be distinguished at which the contrast between the polluted surface and the clean one drops to zero. The null contrast situation happens usually

when observing the slick at moderate inclinations. The more rough the sea surface, the larger is the zenith angle at which null contrast is observed. When the sun is low over the horizon, the null contrast conditions are possible only when the sun is behind the observer's back.

In summary, from the point of view of optical remote sensing technique, the optical response of an oil film floating on a water surface can be described by the reflectance distribution over the film and by the contrast between oil and surrounding water. Thus the study of an oil film on seawater leads to firstly analyze OS-water reflectance spectra, separately for low and high glint conditions. Obviously, the dimension of an oil spill should be greater than the spatial resolution of the sensor.

2.1.4 Illumination-view geometry

Solar illumination and sensor viewing geometry impact on the behavior of oil spill visibility in optical imagery. Taken a point on Earth observed by the sensor as a reference, we define:

- Sun zenith angle θ_{Sun} as the angle between the local outward normal and the vector from the point towards the Sun;
- Satellite (view) zenith angle θ_{Sat} as the angle between the local outward normal and the vector towards the sensor;
- Azimuth difference $\Delta\Phi$ as the angle between the half-plane containing the local normal and the Sun, and the half-plane containing the local normal and the satellite.

In the principal plane, there may be *specular reflection*, also known as *high glint* condition, of a point source into the sensor when the azimuth difference is 180° and the zenith angles are equal. Figure 2.3 illustrates illumination and viewing angles. Due to the higher oil refraction index, positive oil-water contrast occurs in specular reflection, otherwise (*low glint* condition) negative contrast. Figure 2.4, relative to MODIS and MERIS imagery of the Lebanon oil spill disaster (2006), show how positive oil-water contrast occurs in high glint condition (figure 2.4 b), the opposite in low glint condition (figure 2.4 a). Under specular reflection a portion of the satellite image will result glint-contaminated. This provides a first criterion on oil spill detection, based on oil-water contrast. We classify each OS scene as "high" or "low" glint, depending on whether the slick is in specular reflection conditions or not. A detailed discussion on the geometric computation for the high and low glint condition is reported in chapter III.

Figure 2.3 Illumination and observation geometry angles.

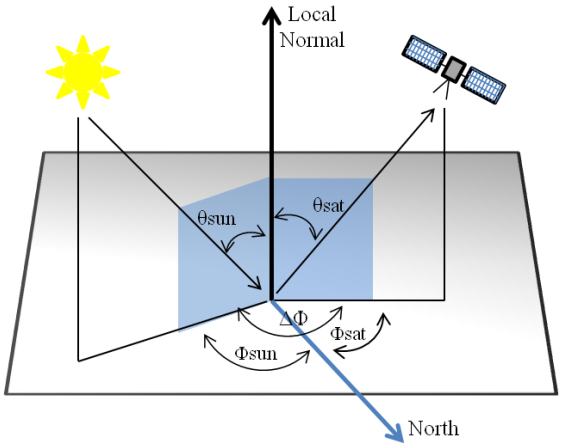

Lebanon Coast Oil Spill, 2006, True Color Images

(a) MODIS TERRA Low Glint Condition

(b) MERIS High Glint Condition

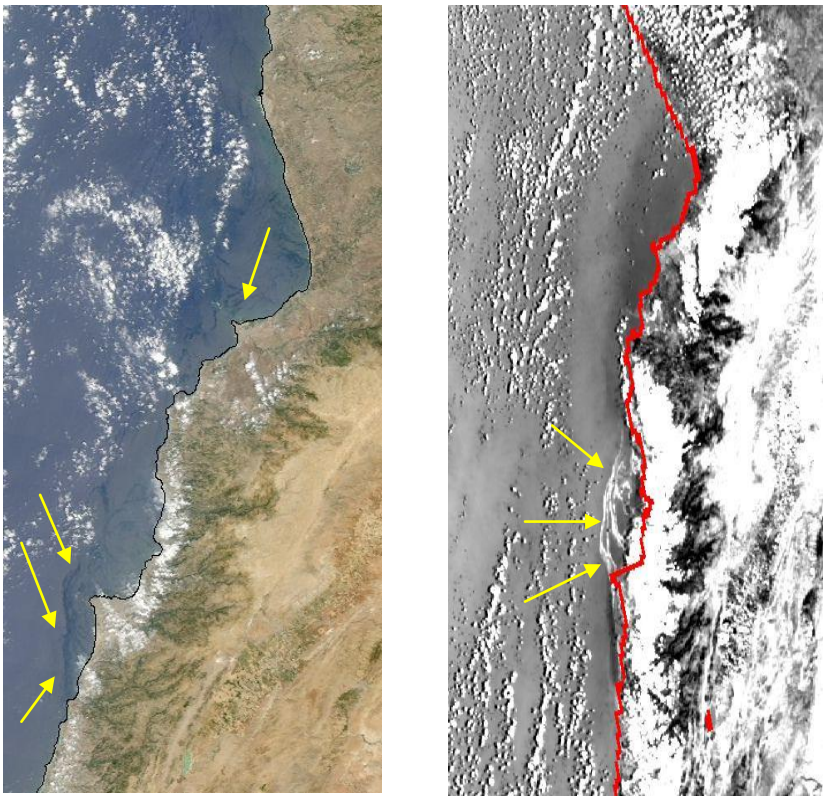

Figure 2.4 True color images relative to the oil spill disaster of the Lebanon coast (summer 2006). **(a)** MODIS TERRA (August 17 2006, 08:30 UTC) detail, low glint condition. **(b)** MERIS (July 20 2006, 08:19 UTC) detail, high glint condition.

2.2 Optical sensors used for oil spill detection algorithm

Here we introduce MODIS and MERIS satellite sensors and briefly illustrate their main technical characteristics. MODIS and MERIS data were used for the development and validation of the OS detection algorithm.

2.2.1 MODIS

Moderate-resolution imaging spectrometer (MODIS) is NASA's ocean colour sensor of the type sketched in figures G.2 (a) and G.3 (a) (Appendix G), operating in mechanical mode. MODIS is onboard of two satellites, TERRA and AQUA, with the same technical characteristics. Flying at an altitude of 705 km, in sun-synchronous orbit (i.e., the satellite crosses the equator at the same local solar time on each pass of every day) with a local overpass time of 10.30 for MODIS TERRA and 14.30 for MODIS AQUA, provides a swath of 2330 km (cross track) by 10 km (along track at nadir), a revisit time of 1-2 days and 36 discrete bands located between 0.4 and 14.4 micron region of e.m. spectrum. MODIS measures in seven bands in visible and near-IR range at finer spatial resolution, two at 250 m (bands 1-2) and five at 500 m (3-7) compared with 1 km for the main set (bands 8-36). Table 2.1 lists the principles characteristics of MODIS for the first 19 bands. Bands 1-2 are used primarily for land/cloud/aerosols boundaries (250 m), bands 3-7 for land/cloud/aerosols properties (500 m), bands 8-16 for ocean colour/phytoplankton/biogeochemistry and bands 17-19 for atmospheric water vapor (1 km). This allows the MODIS instrument to provide images of daylight-reflected solar radiation and day/night time thermal emissions. Images of the observed radiances or derived geophysical products from MODIS may show systematic artifacts that appear as stripes running perpendicular to the orbit track. This is a consequence of the different sensitivities and variable calibrations of different detectors scanning several scan lines in parallel. systematic artifacts that appear as stripes running perpendicular to the orbit track Moreover, the sensor scan mechanism uses a double sided mirror so that two ground scans instead of one can be achieved per revolution of the scan assembly. Unfortunately differences between the reflection losses on different sides introduces further striping. For the 500 and 250 meter bands, 20 and 40 detectors are distributed along-track to provide the higher along-track resolution. As such, cross-track striping artifacts at 20 and 40 line intervals can occur for the 500 and 250-meter bands, respectively. Corrections have been applied for these effects (chapter III).

Band	Bandwidth (nm)	Resolution	Application
1 (VIS)	620 – 670	250 m	Land/Cloud/Aerosols Boundaries
2 (NIR)	841 – 876	250 m	
3 (VIS)	459 – 479	500 m	Land/Cloud/Aerosols Properties
4 (VIS)	545 – 565	500 m	
5 (NIR)	1230 – 1250	500 m	
6 (NIR)	1628 – 1652	500 m	
7 (NIR)	2105 – 2155	500 m	
8 (VIS)	405 – 420	1 km	Ocean Colour/ Phytoplankton/ Biogeochemistry
9 (VIS)	438 – 448	1 km	
10 (VIS)	483 – 493	1 km	
11 (VIS)	526 – 536	1 km	
12 (VIS)	546 – 556	1 km	
13 (VIS)	662 – 672	1 km	
14 (VIS)	673 – 683	1 km	
15 (VIS)	743 – 753	1 km	
16 (NIR)	862 – 877	1 km	
17 (NIR)	890 – 920	1 km	
18 (NIR)	931 – 941	1 km	
19 (NIR)	915 – 965	1 km	

Table 2.1 MODIS sensor characteristics.

2.2.2 MERIS

Medium-resolution imaging spectrometer (MERIS) is the European Space Agency's first ocean colour sensor (Rast and Bezy, 1999), located onboard the Envisat (ESA) platform (launch March 2002). It is of the imaging spectrometer type operating in push-broom mode, as shown in figures G.2 (b) and G.3 (b) (Appendix G), and in fact has five parallel arrays to gain a swath of 1150 m. The instrument has the capability to measure across 15 spectral bands (visible to near-infrared) which are listed in table 1.3. Although the normal MERIS mode for global monitoring has a spatial resolution of 1200 m, it is capable of 300 m. Unlike MODIS, the finer resolution applies to all spectral bands. This high resolution mode is routinely acquired over European waters. MERIS has a global coverage of 3 days.

Band	Center Wavelength ± Bandwidth (nm)	Resolution (m)	Application
1 (VIS)	412.5 ± 10	300 (1200)	Yellow substance Chlorophyll, Suspended sediments, Atmospheric corrections
2 (VIS)	442.5 ± 10	300 (1200)	
3 (VIS)	490 ± 10	300 (1200)	
4 (VIS)	510 ± 10	300 (1200)	
5 (VIS)	560 ± 10	300 (1200)	
6 (VIS)	620 ± 10	300 (1200)	
7 (VIS)	665 ± 10	300 (1200)	
8 (VIS)	681.25 ± 10	300 (1200)	
9 (VIS)	708.75 ± 10	300 (1200)	
10 (VIS)	753.75 ± 10	300 (1200)	Land/Cloud/Aerosols Properties Atmosphere corrections
11 (VIS)	760.625 ± 10	300 (1200)	
12 (VIS)	778.75 ± 10	300 (1200)	
13 (NIR)	865 ± 10	300 (1200)	
14 (NIR)	885 ± 10	300 (1200)	
15 (NIR)	900 ± 10	300 (1200)	

Table 2.2 MERIS sensor characteristics.

2.3 The data

2.3.1 The oil spill data set

The methodology for oil spill detection in MODIS and MERIS imagery requires the availability of a set of certified oil spill events. We built a database of *in situ* oil spill observations, collecting all the information on oil spill disasters occurred in the Mediterranean Sea and all the oil spills reported by International and Italian National Authorities responsible for the oil spill illegal monitoring. In correspondence of each of these events, we collected the corresponding MODIS (AQUA and TERRA) L0 and MERIS full resolution (300 m) L1B passes, in which the area of hydrocarbon discharge was not covered by clouds and visible in the satellite imagery. This has constituted our OS dataset of certified oil spill cases. This includes a temporal suite of the Lebanon coastal spills, caused by air raids on coastal power plants (July-August 2006), some cases in the Italian seas reported by the Italian Ministry of the Environment, for which remediation units were sent on the spot to perform cleanup duties (2002-2008), an OS off the Algerian coast (August 6-10, 2008) and five OS's visited by CNR's R/V Urania during the PRIMI cruise (see chapter V), for a total number of 40 images. The database is currently being updated, as new OS cases become known.

Each of the MODIS L0 data were processed to produce the corresponding L1B level. MODIS L1B high resolution (250 m) and MERIS L1B full resolution TOA radiance data were visualized by an expert operator. The oil spills visible in the imagery were manually digitized via ENVI's Region of Interest (ROI) tool (figure 2.7) and saved to oil spill position text files. This allowed to add to our database the information on the pixel location of the oil spill. Finally, each OS scene in the examined images has been classified as high or low glint, depending on whether the slick was in mirror-like reflection (high sun glint) conditions or not (see chapter III).

A subset of oil spill events contained in the database has been selected to build the algorithm (training OS database), while the remaining were used to validate the methodology developed during this thesis (validation OS database). This allowed to have independent reference data for algorithm evaluation. The training database (table 2.3) contains oil spills observed by MODIS and MERIS. This database can be considered representative of Mediterranean oil slicks, being characterized by a large variety of oil slicks (large, small, with different shape and thickness, etc..) and different illumination and satellite viewing geometry in the oil spill area (high and low glint case). The training OS database consists of 15 images and includes several Lebanon satellite imagery, because in each of these imagery several slick with different characteristics were present, and 3

imagery of oil spill coming from illegal discharges, verified in situ, in order to cover also small and thin slicks.

Geometric, spectral and statistical analysis carried out on the digitized oil spill structures of the training dataset has permitted to define a set of parameters (*features parameters*) characterizing the oil spills. This allowed the development of our OS detection algorithm, mainly for the definition of shape, spectral and probability criteria for the distinction between oil spills and look-alikes. Finally, the OS ROI from the validation dataset, which includes 25 events, were used for algorithm's validation by comparing them with the oil spill structures automatically detected by our OS detection algorithm (see chapter V).

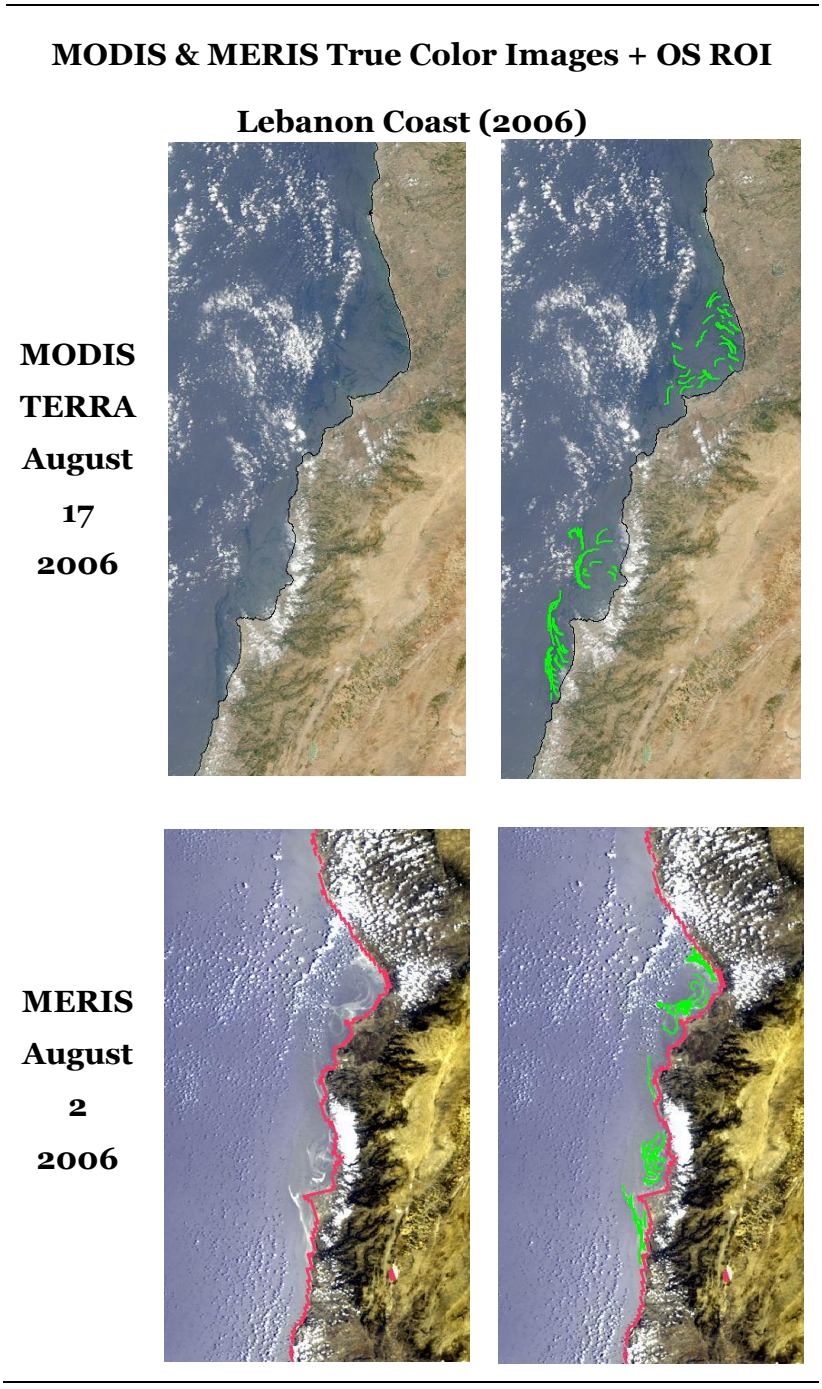

Figure 2.7 Oil spill ROI (green) manually digitized with ENVI ROI tool on Lebanon coast true color images (MODIS and MERIS). ROI pixel coordinates were saved to files and form the OS database, together with the relative imagery in the various bands.

Location	Sensor	Platform	Date (Year/JD)	Local Pass Time
Lebanon	MODIS	TERRA	2006 204	08.35
Lebanon	MODIS	TERRA	2006 213	08.30
Lebanon	MODIS	AQUA	2006 214	10.50
Lebanon	MODIS	AQUA	2006 216	10.40
Lebanon	MODIS	AQUA	2006 218	10.25
Lebanon	MODIS	TERRA	2006 218	08.50
Lebanon	MODIS	AQUA	2006 234	10.25
Lebanon	MODIS	TERRA	2006 234	08.50
Lebanon	MERIS	ENVISAT	2006 214	08.11
Lebanon	MERIS	ENVISAT	2006 217	08.16
Lebanon	MERIS	ENVISAT	2006 227	08.02
Lebanon	MERIS	ENVISAT	2006 230	08.08
Elba Island (Italy)	MODIS	AQUA	2005 229	12.15
Algeria	MODIS	TERRA	2008 220	10.50
Algeria	MODIS	AQUA	2008 220	12.30

Table 2.3 Training OS dataset.

2.2.3 MODIS and MERIS data products

MODIS (TERRA and AQUA) and MERIS imagery, are downloaded respectively from the NASA and ESA websites. MODIS L0 and MERIS L1B (see appendix F for the definition of levels) files are then processed with NASA's SeaDAS v5.4 freeware (http://oceancolor.gsfc.nasa.gov/seadas/help.html) to obtain the remapped L2 products (http://oceancolor.gsfc.nasa.gov/DOCS/MSL12/MSl12_prod.html). Table 2.4 lists MODIS and MERIS L2 products chosen to perform the processing steps described in the following section. Chosen wavelengths for each sensor and its product are:

- MODIS: (469, 555, 645, 859, 1240, 1640, 2130) nm;
- MERIS: (443, 560, 665, 681, 865) nm.

MODIS/MERIS L2 PRODUCTS	PHYSICAL SYMBOL	UNITS	DESCRIPTION
RHOT (NNN*)	ρ_T	NON-DIM.	TOP OF ATMOSPHERE REFLECTANCE
LR (NNN)	L_R	MW/CM2/μM/SR	RAYLEIGH RADIANCE
LT (NNN)	L_T	MW/CM2/μM/SR	CALIBRATED TOA RADIANCE
LW (NNN)	L_W	MW/CM2/μM/SR	WATER-LEAVING RADIANCE
T_SEN	N/A	NON-DIM.	DIFFUSE TRANSMITTANCE, GROUND TO SENSOR
TG_SEN	N/A	NON-DIM.	TOTAL GAS TRANSMITTANCE, GROUND TO SENSOR
T_O2	N/A	NON-DIM.	TOTAL OXYGEN TRANSMITTANCE
TAUA (NNN*)	N/A	NON-DIM.	AEROSOL OPTICAL THICKNESS
CLOUD ALBEDO	N/A	NON-DIM.	REFLECTANCE AT 869 NM AFTER SUBTRACTING GLINT AND RAYLEIGH REFLECTANCE
L2 FLAGS	N/A	N/A	L2 PROCESSING FLAGS (FOR LAND, CLOUD, SUNGLINT, ETC.)
QUAL_SST	N/A	N/A	SST QUALITY LEVELS MAP
SENA	ϕ_{SAT}	DEG	SENSOR AZIMUTH ANGLE MAP
SOLA	ϕ_{SOL}	DEG	SOLAR AZIMUTH ANGLE MAP
SENZ	θ_{SAT}	DEG	SENSOR ZENITH ANGLE MAP
SOLZ	θ_{SOL}	DEG	SOLAR ZENITH ANGLE MAP

Table 2.4 MODIS and MERIS products used for the OS detection algorithm. *_NNN indicates wavelength in nm.

We remind that Rayleigh radiances are due to atmospheric gas molecular scattering and that water leaving radiance is the radiance which leaves the sea surface, i.e. total radiance minus atmospheric correction.

2.4 Oil spill detection methodology

The automatic OS detection algorithm consists of three main parts, i.e. image flattening, image clustering and OS candidate selection. These techniques are described in detail in chapters III and IV. Figure 2.6 shows the scheme of our OS detection algorithm, composed of the following steps:

I. Acquisition and pre-processing:
   - MODIS L0 and MERISL1B full resolution (300 m) data download;
   - MODIS and MERIS data processing (L0 to selected standard L1B);

II. Striping correction (MODIS only) and production of geophysical data:
   - Destriping (only for MODIS imagery);
   - MODIS and MERIS data processing (L1B to L2) to produce selected geophysical products (table 2.4);

III. L2 TOA reflectance bands ($\rho_t(\lambda)$) and the selected geophysical products are the input for the image flattening procedure:
   - Cloud Masking;
   - Elimination of Rayleigh and water-leaving reflectance;
   - Elimination of aerosol contribution;

IV. The elimination of natural oceanic and atmospheric natural variability provides flattened reflectance products ($\rho_\varepsilon(\lambda)$), that become the new input for the clustering and OS classification steps:
   - Segmentation and clustering;
   - OS selection among cluster regions via geometric, spectral and statistical criteria;
   - Score assignment to OS candidates.

MODIS (TERRA and AQUA) L0 and MERIS full resolution (300 m) L1B data downloading and processing to L2 products (step I) are obtained via standard procedures (see paragraph 2.2.3). Destriping (step II) is an *ad hoc* procedure, developed to eliminate the striping effect of MODIS imagery. This is performed at MODIS L1A level. Image flattening (step III) has the objective to eliminate the oceanic and atmospheric natural

variability from the input MODIS and MERIS TOA reflectance bands ($\rho_t(\lambda)$). The results are what we call flattened images ($\rho_\varepsilon(\lambda)$) in which oil slicks, eventually present, can stand out. The enhancement of oil spill structures facilitate both the detection by a human operator and improve the automated detection process (IV). Clustering is carried out on the corrected reflectance bands and produces a set of cluster regions. The application of a set of "discriminant" criteria to each cluster region retains only a small number of regions, classified as candidate oil spills. The final result is the classification of each oil spill candidate region by means of the assignment of a score.

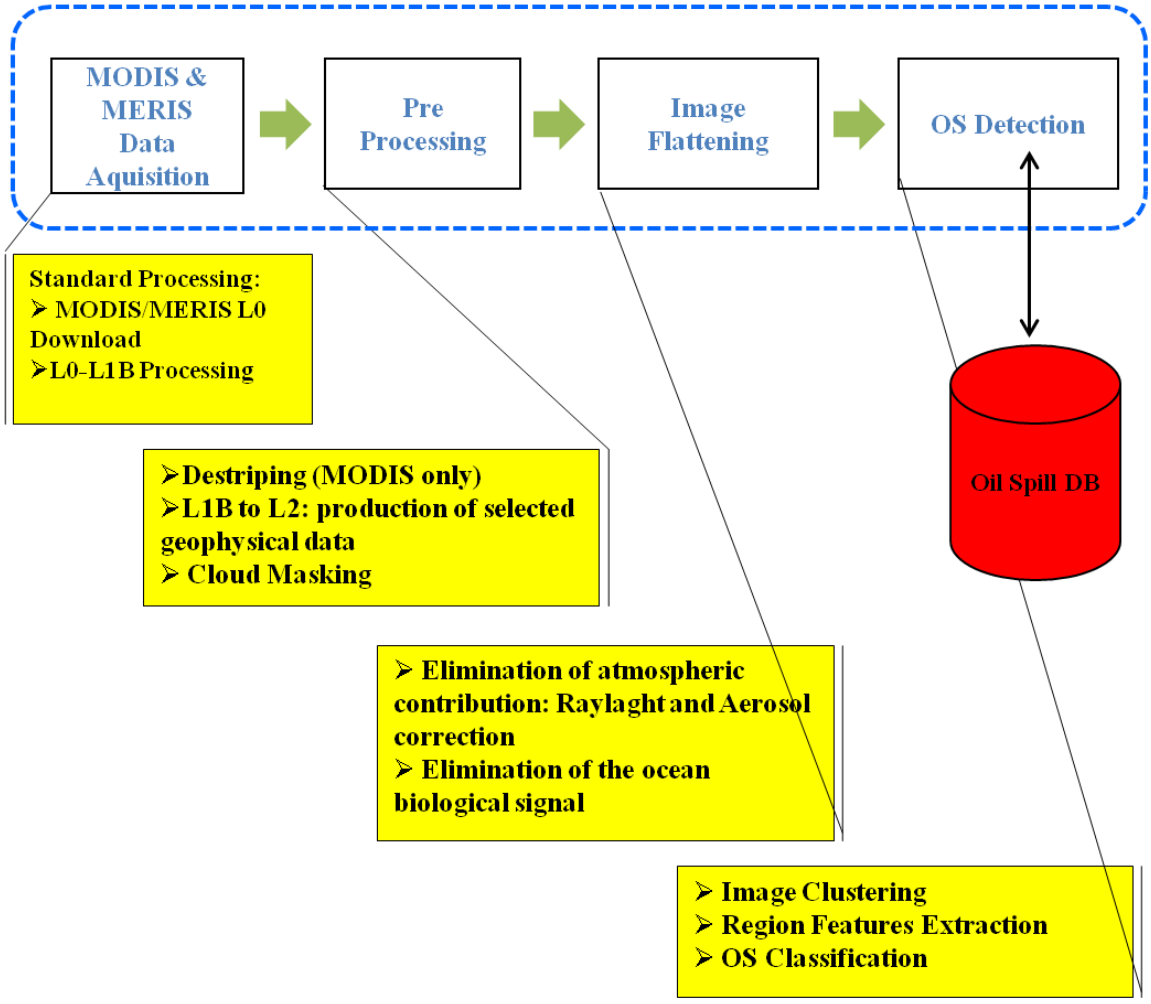

Figure 2.6 Flowchart of the OS detection algorithm.

Chapter 3

Development of Oil Spill Detection Methods for Optical Imagery: Image Flattening and Features Extraction

Here we present and discuss the methodology developed to obtain identifiable spills in MODIS high and medium (250 and 500 m) resolution and MERIS full resolution (300 m) top of atmosphere (TOA) reflectance images (ρt), i.e. the image correction. The main idea is the removal of atmospheric and oceanic natural variability from ρt bands in order to flatten them and enhance oil-water contrast. It consists of striping correction (only for MODIS imagery), cloud masking and image flattening. Finally, we illustrate the choice of a suitable set of features parameters defined to characterize the slicks based on spectral, geometric and statistical analysis carried out on the oil spill (OS) dataset.

3.1 Image flattening

The basic idea of the image correction is to enhance OS contrast with respect to clean water as much as possible in the MODIS and MERIS full resolution (300 m) TOA reflectance bands ρt(λ), for all chosen wavelengths λ1, before classifying high or low contrast surface structures as oil spills or look-alikes. Indeed, oil slicks in standard TOA reflectance images are often confused visually (and numerically) with analogous look-like oceanographic features such as chlorophyll filaments, organic and/or inorganic suspended matter etc. Moreover, atmospheric effects such as reflectance modulation due to aerosol

[1] λ = (469, 555, 645, 859, 1240, 1640, 2139 nm) for MODIS imagery;
λ = (443, 560, 665, 681, 865) for MERIS imagery.

patches can introduce further noise, thus masking the slicks. First, a destriping procedure, developed to remove the "striping" effect from MODIS imagery, and a cloud masking procedure are applied to each input $\rho_t(\lambda)$ image. Then, a procedure devised to "strip" each $\rho_t(\lambda)$ image from the reflectance deriving from atmospheric and oceanic natural variability is applied, thus leaving a smoother or flat "residual ocean" field in which oil slicks stand out better, thus being less liable to be confused with or masked by non-slick features. This is achieved by the elimination of natural variability relative to oceanic and atmospheric (Rayleigh and aerosol) contribution. This procedure, reducing signal variability, also facilitates the application of the successive image clustering step, as discussed in chapter IV.

3.1.1 Destriping and cloud masking

MODIS images are affected by "striping" (Weinreb, 1989; Antonelli, 2004), that is, horizontal stripes are clearly visible in any MODIS product (e.g. L1B TOA radiances or L2 products; figure 3.1 a) as artifact gradients. These stripes are due to the fact that two consecutive data sweeps, perpendicular to the satellite's flight direction, are acquired by the two faces of a rotating mirror, which reflect the light from the scene to the onboard sensors. Now, the two mirror sides are not optically exactly equal (coating, etc.); therefore the amount of light reflected from the same scene to the sensors by one face is slightly different from the other. Also, each scan is made of a set of lines perpendicular to the scan (i.e. parallel to the nadir track), each of which is sensed by N detectors(figure 3.1 a, the green line shows one of these lines covering two mirror scans). Indeed, for each wavelength, the light coming from the observed portion of the surface reflects on the mirror and impacts on a line of N detectors aligned parallel to the nadir track. The number N of detectors is variable depending on each band's spatial resolution. The 250 m resolution bands have N = 40, the 500 m resolution bands have N = 20 and the 1 km resolution bands have N = 10. The set of sensors receiving the light also have small response differences, thus introducing further finer striping within each large stripe. The overall result is that a data line across swaths is disturbed by a ramp-like artificial trend (figure 3.1 c). The correction of this problem has already been addressed (see e.g. Antonelli, 2004). At present, a simple version of destriping is performed at the L1A level of the standard processing. It consists of determining the slope and bias of the regression line best fitting each ramp and "rectifying" the ramp (figure 3.1 c) by subtracting the regression line from the signal. Finally, new destriped L1A files are produced and fed back into SeaDAS for the processing to obtain the final L1B and L2 products. The result L2 image after destriping is shown in figure 3.1 (b).

In particular, to eliminate detector bias, we calculate, for each detector line,

$\Delta\rho_i$ = [ρ(detector line i+1,detector 1)-ρ(detector line i, detector 1)]/[ρ(detector line i,detector 1],

that is, the percent difference in reflectance between the last (Nth) detector in one mirror side (i) and the reflectance of the first detector in the next mirror side (i+1; e.g. the difference between detectors at x = 80 and x = 112 for detector line i, x = 40-79 in figure 3.1 c). For each mirror side scan i we then have Nx values of $\Delta\rho i$, where Nx is the width of the image, in number of pixels (if no pixels are flagged). We then take the average value of the Nx $\Delta\rho i$ values, i.e. $<\Delta\rho i>$, and "rectify" each detector line within a given mirror scan by means of

$\rho_{det\ corr}$(mirror side i, detector j) = ρ(mirror side i, detector j)*[1 + $<\Delta\rho_i>$*(-1/2 +(j-1)/N)] ; j = 1, N

To correct for mirror side differences, we compute:

$<\rho_{det\ corr}(1)>$ = average of all ρdet corr (mirror side 1 scans)

and

$<\rho_{det\ corr}(2)>$ = average of all ρdet corr (mirror side 2 scans)

and correct the mirror side 1 reflectances via

$\rho_{corrected}$(mirror side 1) =$\rho_{det\ corr}$(mirror side 1) *[1. + $<\rho_{det\ corr}(2)>$/ $<\rho_{det\ corr}(1)>$]

thus modifying mirror side 1 reflectances to the values they would have if detected by mirror side 2. Mirror side 2 reflectances are left unaltered after detector correction:

$\rho_{corrected}$(mirror side 2) =$\rho_{det\ corr}$(mirror side 2).

Note that it would be the same to do the opposite, i.e. reduce mirror side 2 reflectances to mirror side 1 values. The dashed line in figure 3.1 (c) shows the result of these two corrections and it can be seen that there are no more artificial jumps across mirror sides.

Figure 3.1 (b) shows that there is still a faint trace of striping in the corrected image, due to the use of $<\Delta\rho_i>$, which are averages for each scan, while it would be more appropriate to correct separately for each $\Delta\rho_i$. The destriping algorithm is not yet fully performant as and requires further development; however, the present algorithm has proven satisfactory for our purposes, e.g. in eliminating elongated look-alike features at the border between two major stripes.

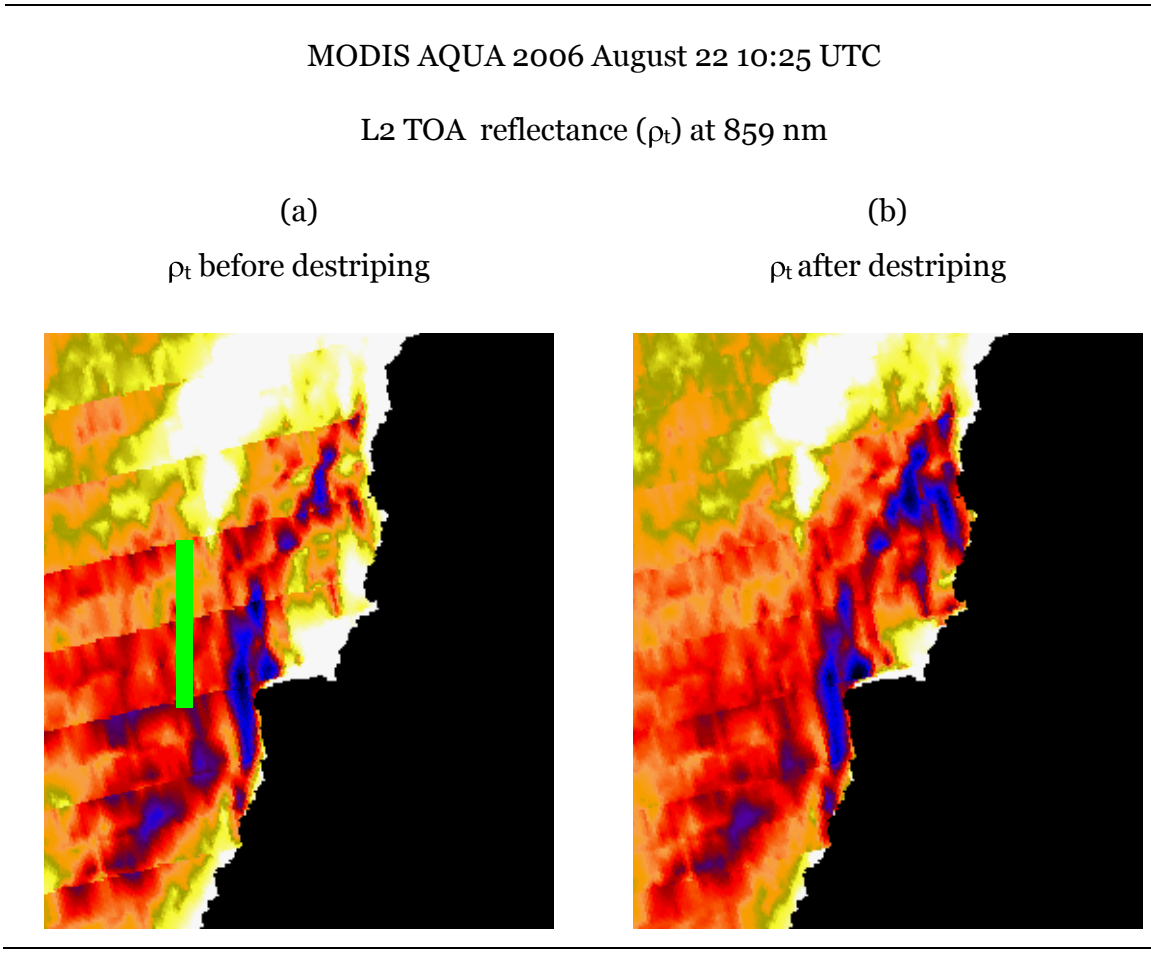

Figure 3.1 (a) MODIS L2 TOA reflectance (ρ_t) image showing striping. Green line refers to section across stripes given in **(c)** (each major stripe has 40 detectors, this being a 250 m resolution image);. **(b)** destriped image.

(c)

Reflectance (black line, in raw counts, y axis) across three mirror scans

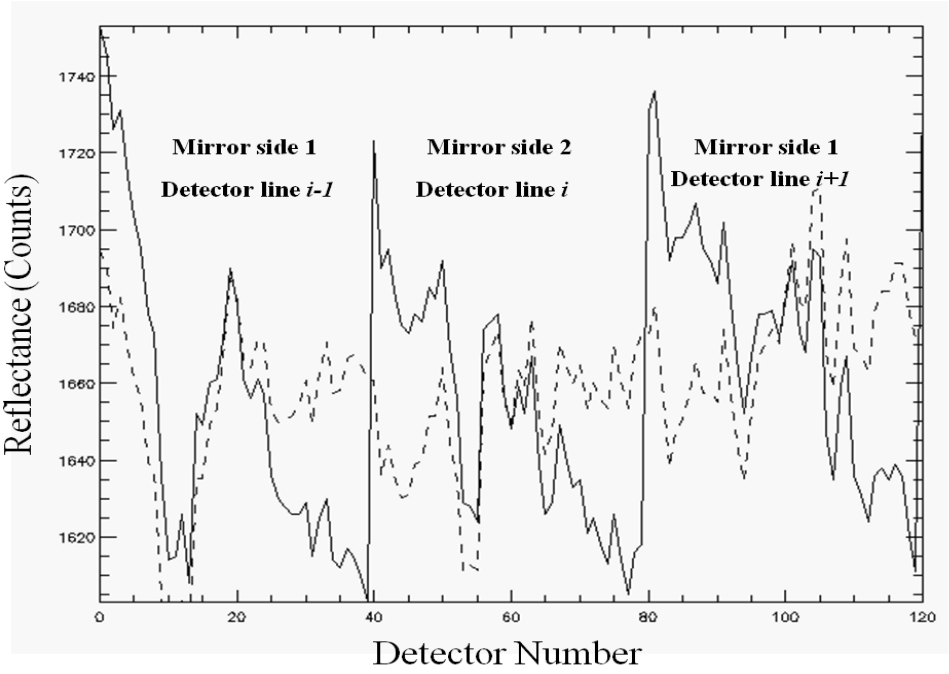

Figure 3.1 (c) Section across stripes (green arrow in **(a)**, indicating also flight direction), with striping ramps (solid line) across three swaths acquired by different mirror sides and due to sensor hardware differences and corrected reflectance after destriping (dashed line). Reflectance expressed in counts.

Finally, a cloud masking procedure is performed via the SST quality flag product (quality indicator for Sea Surface Temperature computation, see table 2.3) and a specific procedure based on the high positive contrast for the cloud pixels in the high (250 or 300 m) resolution bands. The use of the SST quality flag instead of the standard cloud flag product (L2 Flag, table 2.3) arises from the fact that the latter sometimes masks oil spill pixels as clouds. Using the SST quality flag, all pixels for which even one quality flag indicates bad SST are flagged as bad data. However, not all cloudy pixels can be removed in this way. Therefore, a custom procedure has been developed: the reflectance standard deviation of each pixel and its 3x3 pixel bounding box is computed and saved in a new matrix. Since cloudy pixels have high reflectance with respect to surrounding water, the standard deviation of a cloudy pixel and its bounding box will be high. Thus, cloudy pixels are further removed from the original image via thresholding on this standard deviation.

3.1.2 Image flattening

Image flattening is made of several customized steps, the main idea being the elimination of all signals extraneous to the response of oil and clean water, in the hope of exalting oil-water contrast. In general, ρ_t is composed of various contributions (Robinson, 1994), i.e.

$$\rho_t = \rho_r + \rho_a + \rho_{ra} + \rho_{sfc} + t\rho_w,$$

where

- ρ_r = Rayleigh reflectance;
- ρ_a = Aerosol reflectance;
- ρ_{ra} = Rayleigh-Aerosol interaction reflectance;
- ρ_{sfc} = Surface reflectance (geometric reflectance, modulated by surface orientation + wind speed and whitecap reflectance);
- $t\rho_w$ = water reflectance term at the TOA, i.e. ρ_w scaled by the air column transmittance (t).

Image flattening consists in subtracting from each reflectance band $\rho_t(\lambda)$ the contribution of the Rayleigh reflectance $\rho_r(\lambda)$, water-leaving reflectance $\rho_w(\lambda)$ and the aerosol reflectance $\rho_a(\lambda)$. We neglect Rayleigh-Aerosol interaction and surface reflectance contribution, being irrelevant for this procedure. It is to be noted that 500 m resolution MODIS bands are scaled to 250 m resolution. We discuss below the adopted steps.

Rayleigh Scattering Removal

The first attempt is to obtain Rayleigh scattering-free images. Rayleigh reflectance $\rho_r(\lambda)$ is obtained as:

$$\rho_r(\lambda) = L_r(\lambda)\, \rho_t(\lambda) / L_t(\lambda)\ ,\ \forall\ \lambda_{MODIS}, \lambda_{MERIS}$$

since Rayleigh reflectance is not available as standard L2 product. The ρ_t / L_t ratio is the scaling to convert total radiance to reflectance by normalizing by the solar zenith angle, atmospheric transmittance and earth-sun distance. Rayleigh reflectance is then removed from each TOA reflectance band obtaining $\rho_t(\lambda)$ - $\rho_r(\lambda)$ images.

Water-Leaving Reflectance Removal

The Rayleigh-removed reflectance, $\rho_t(\lambda) - \rho_r(\lambda)$, still displaying high variability, is further "flatten out" by eliminating all natural (i.e. water and atmosphere) contributions from it in the hope of obtaining an image in which non-natural features such as slicks may stand out more univocally. To this purpose, we have defined a water-leaving radiance at the top of the atmosphere (TOA) for the blue and green bands as follows:

$$L_{wTOA}(\lambda) = Lw(\lambda) * t\_sen * tg\_sen * t\_02 \text{ , } (\lambda_{MODIS} = 469, 555; \lambda_{MERIS} = 443, 560)$$

This quantity is essentially the water-leaving radiance as seen from the top of the atmosphere, obtained by multiplying the water-leaving radiance (L_w) by the atmosphere transmittances products (see table 2.3). In this way, we obtain an "attenuated" version of water leaving radiance which is subtracted from $\rho_t(\lambda) - \rho_r(\lambda)$ after being converted into reflectance. This is done because water-leaving was seen to have too strong signal and thus subtracted too much signal from $\rho_t(\lambda) - \rho_r(\lambda)$. The normalized water-leaving reflectance ($\rho_w(\lambda)$) is obtained via:

$$\rho_w(\lambda) = L_{wTOA}(\lambda)\, \rho_t(\lambda)/L_t(\lambda), \ \forall\ \lambda_{MODIS}, \lambda_{MERIS}$$

as done for ρ_r. This is subtracted from the $\rho_t(\lambda) - \rho_r(\lambda)$ blue and green band images, obtaining $\rho_t(\lambda) - \rho_r(\lambda) - \rho_w(\lambda)$ residual images. The subtraction of ρ_w is confined to the blue and green bands, because for larger wavelengths the water is essentially "black", contributions to reflectance being mainly from the atmosphere.

Aerosol Removal

The process of image flattening is concluded by the elimination of the aerosol signal using the red band (λ = 645 nm), since water is "black" at this wavelength. To this purpose, we have defined the difference $\rho_t(645) - \rho_r(645)$ as a proxy of aerosol reflectance, since Rayleigh signal has already been removed. Further, we smoothed this difference ($<\rho_t(645) - \rho_r(645)>$) in order to reduce the high variability presents in this band. Then, calculation of the reflectance distribution histogram for all $\rho_t(\lambda) - \rho_r(\lambda)$ (λ > 555 nm) or $\rho_t(\lambda) - \rho_r(\lambda) - \rho_w(\lambda)$ (λ_{MODIS} = 469, 555; λ_{MERIS} = 443, 560) products and computation of the maximum reflectance value $\rho_{max}(\lambda)$, corresponding to the maximum number of occurrences in the image, is performed. The ratio $\varepsilon(\lambda) = \rho_{max}(\lambda)/\rho_{max}(645)$ is computed for each band and is used to obtain the aerosol reflectance map normalized to band λ, i.e.:

$$\rho_{red}(\lambda) = \varepsilon(\lambda) \, [\, <(\rho_t(645) - \rho_r(645)> \,] \, , \; \forall \; \lambda_{MODIS}, \lambda_{MERIS}$$

and thus the corrected image results:

$$\rho_\varepsilon(\lambda) = \rho_t(\lambda) - \rho_r(\lambda) - \rho_w(\lambda) - \rho_{red}(\lambda) \, , \, (\lambda_{MODIS} = 469, 555; \lambda_{MERIS} = 443, 560)$$

or

$$\rho_\varepsilon(\lambda) = \rho_t(\lambda) - \rho_r(\lambda) - \rho_{red}(\lambda) \, , \, (\text{remaining bands, no } \rho_w \text{ removal})$$

The results of this procedure are what we called $\rho_\varepsilon(\lambda)$ or "flattened" reflectance. Figures 3.2 (a) and (b) show the effect of such a correction for the case of the Lebanon coastal spill. Figure 3.2 (a) represents MODIS ρ_t band at 859 nm, while figure 3.2 (b) the corrected version, i.e. ρ_ε at 859 nm. It is seen how, at least visually, the corrected image in figure 3.2 (b) is smoother and, more importantly, slicks stand out and have finer detail than in figure 3.2 (a), and striping is well removed. Reflectance range in ρ_ε (figure 3.2 b) is reduced by about 25% respect to that of ρ_t (figure 3.2 a). Now, negative values may appear, due to successive subtractions procedures.

In the next paragraph, we analyze the effects of the image correction on the remaining bands, mainly looking at the reflectance behaviour in the slick area and on the surrounding water.

(a)

ρ_t (859 nm)

MODIS AQUA, August 22, 2006, 10:25 UTC.

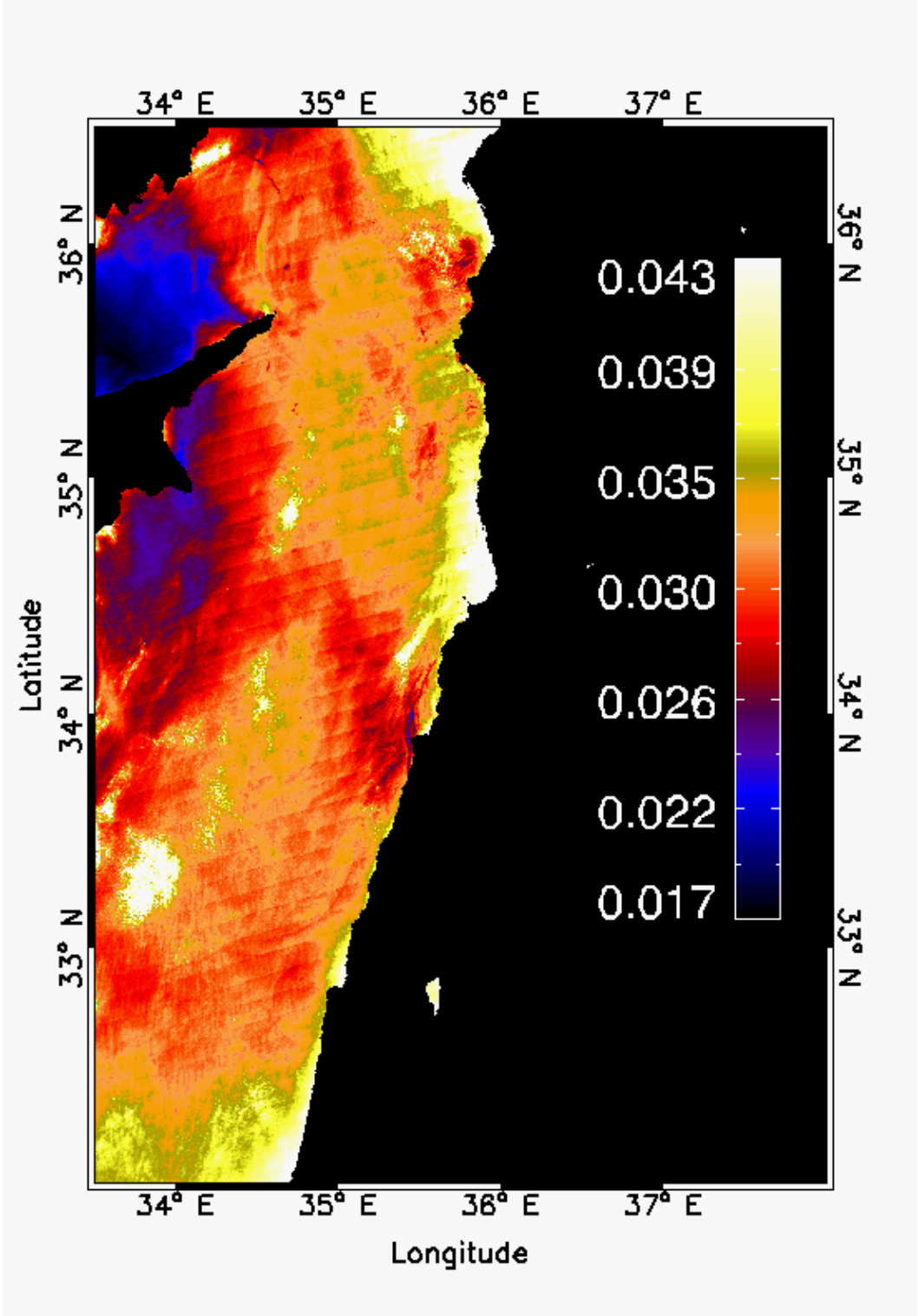

Figure 3.2 (a) ρ_t at 859 nm, MODIS AQUA, August 22, 2006, 10:25 UTC.

(b)

ρ_ε (859 nm)

MODIS AQUA, August 22, 2006, 10:25 UTC.

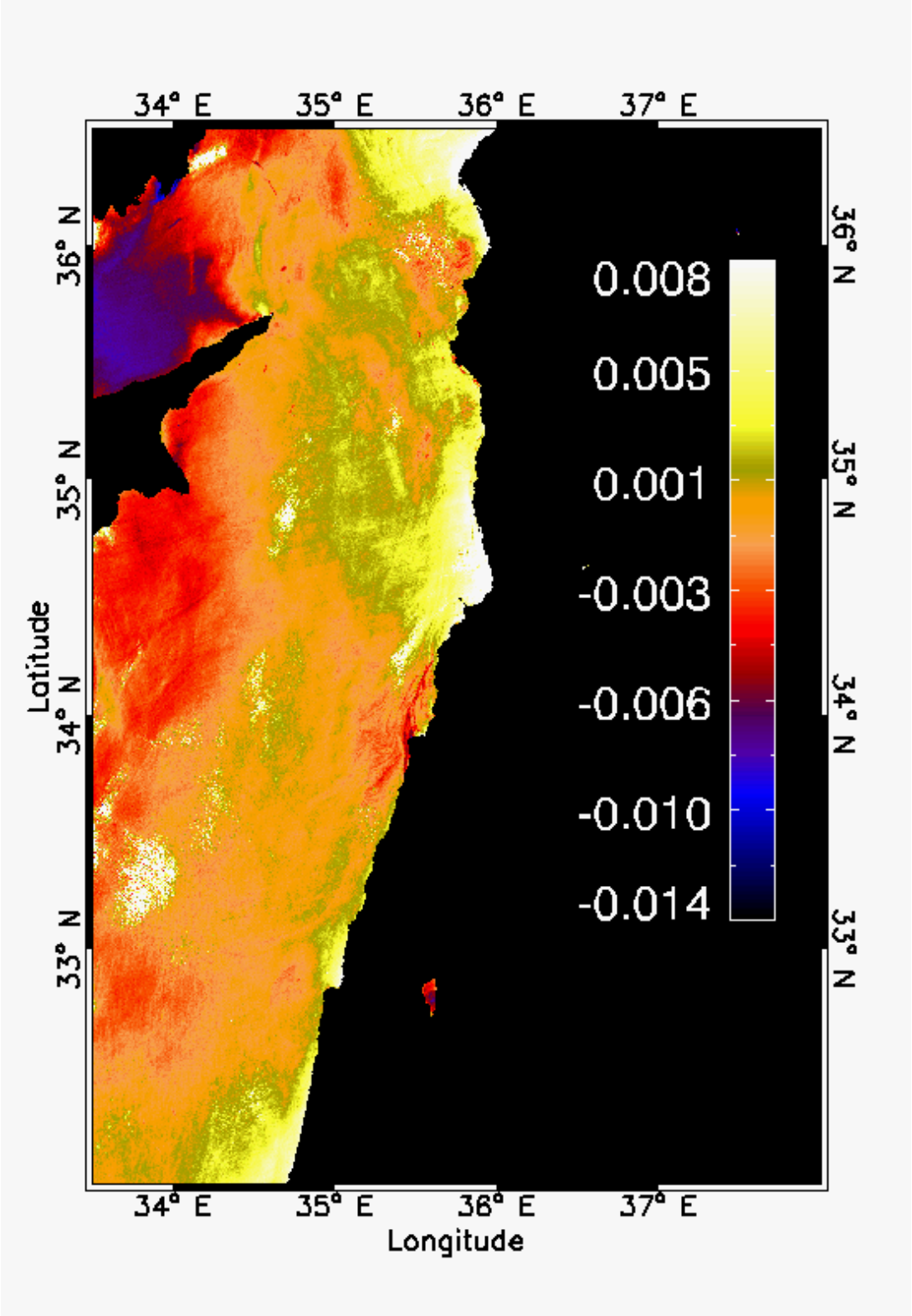

Figure 3.2 (b) $\rho_\varepsilon = \rho_t - \rho_r - \rho_{red}$ at 859 nm, MODIS AQUA, August 22, 2006, 10:25 UTC.

3.1.3 Image correction analysis

We discuss here the effects of the image correction, by showing its application to two MODIS OS scenes of the oil spill dataset, relative to the Lebanon case. One of these has already been introduced above (figures 3.2 a and b) and is in low glint case, while the other is in high glint case (figures 3.5 a and b). We analyze the reflectance contrast between slicks and surrounding water in $\rho_t(\lambda)$ and $\rho_\varepsilon(\lambda)$ local reflectance distributions, i.e. before and after image correction. For this purpose, reflectance histograms were computed for each oil spill region of the OS database and surrounding water bounding boxes, for all chosen bands. Figures 3.4 (a, b) and 3.5 (a, b) show the effects of the image correction for all MODIS bands, while figures 3.4 (c, d) and 3.5 (c, d) show oil and clean water ρ_t and ρ_ε distributions.

First, it must be said that the red band (ρ_ε at 645 nm) is corrected by subtracting a smoothed version of itself from the original. An example is shown in figure 3.3 (a) and (b) for the spill of the Lebanon case. In most cases this results in a fragmented and jagged image, with the exception of a few cases of large and thick spills, like that of figure 3.3 (b). This band is therefore not taken into account for the next steps because the large majority of spills are small, as they are caused by illegal discharge.

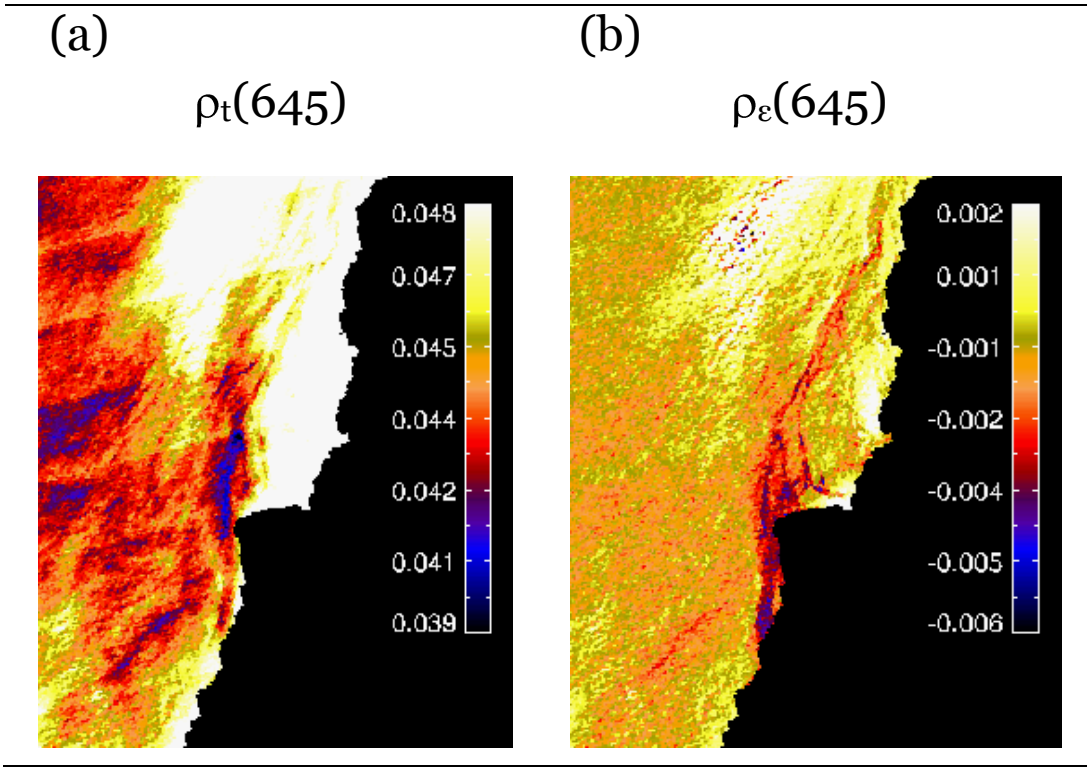

Figure 3.3 MODIS AQUA Aug. 22, 2006, 10:25 UTC, Lebanon coast detail, **(a)** ρ_t red band (645 nm); **(b)** ρ_ε red band (645 nm).

Further, not all bands react in the same way to the above correction. The oil spill region in the blue band (469 nm) of figure 3.4 (a) disappear after correction (figure 3.4 b), or the spill in high glint condition (figure 3.5 a) remains "blurred" and ill-defined after correction, for both 469 and 555 nm bands. In some cases, the ocean sensitive 469 and 555 band ρ_ε show an inversion of contrast in the slick area, displaying positive (negative) contrast in correspondence of slicks in low (high) glint conditions. This because the water leaving radiance is relatively low on the slicks, while high in water, and thus its removal from the image lowers the water signal more than the slick signal, leaving a brilliant slick in the ρ_ε. This effect will be matter of future studies for the effectiveness of auto detection as it maybe a new slick/look-alike discriminatory tool. Longer wavelength bands can display fine detail in the slick areas before correction, the benefit of the latter being a reduction in the image variability and the more net separation in reflectance values between slicks and clean water. Figures 3.4 (a, b) and 3.5 (a, b) show how, for most bands, the spatial variability found in ρ_t is eliminated in ρ_ε, i.e. after the correction described above.
We can resume the effects of the image correction as follows:

- Slicks are more recognizable by an operator in "flatter" ρ_ε images, but slick visibility is not always preserved, especially for blue and green bands.
- Striping is partially removed.
- Image flattening is useful for the clustering process (chapter IV), in that the elimination of variability reduces cluster number and number of sub-regions for each cluster. For example, mesoscale oceanic features are eliminated by flattening and therefore the clustering algorithm will not have to "handle" them together with potential oil spills, thus reducing the probability of ambiguities in feature classification.

Oil and surrounding water $\rho t(\lambda)$ and $\rho\varepsilon(\lambda)$ reflectance distributions are shown by the histograms of figures 3.4 and 3.5 (c) and (d). What is important to note is that the overall separation between oil and surrounding water reflectance distribution is not sufficiently "clear". This does not permit to define "simple" threshold values in order to discriminate oil spill regions from their background, as happens for SAR satellite images where detection is done by adaptive thresholding, based on an estimate of the typical backscatter level. The physical reason for the absence of a clear separation lies in the fact that oil spills are patchy, and this was confirmed during the validation cruise (chapter V). Oil concentration on the sea surface, even within a small oil slick, may vary from extremely thin film to heavily polluted brown or black waters with floating hydrocarbon solid particles of variable dimensions. This patchiness has a spatial variability scale inferior to the MODIS and MERIS

resolution. Further, oil film can be broken and water can be found within the film. Moreover, “clean” water pixels surrounding an OS may actually be affected by slight pollution. Finally, declouding and flattening processes are not perfect and residuals of clouds or natural surface variability may still be present. Consequently, reflectance from a pixel within an OS is often an average reflectance resulting from a mix of the above situations. At present, the band yielding best OS visibility, i.e. in enhancing and maintaining the oil spill after image correction, results to be the 859 nm, also because of its 250 m resolution. This led us to choose $\rho\varepsilon$ (859) as the “optimal” band for the clustering procedure following image correction.

In summary, the reduced variability in the corrected images, the emergence of finer detail in the slicks and their enhanced distinction in numerical values with respect to clean water suggests that this correction step is promising for unknown slick detection. However, the lack of a clear-cut separation between oil and surrounding water reflectance distribution induced us to develop classification criteria based on the definition of *ah hoc features* descriptors, tailored to oil spill detection (see paragraph below).

(a)

$\rho_t(\lambda)$

MODIS AQUA August 22 2006, OS detail of Lebanon coast

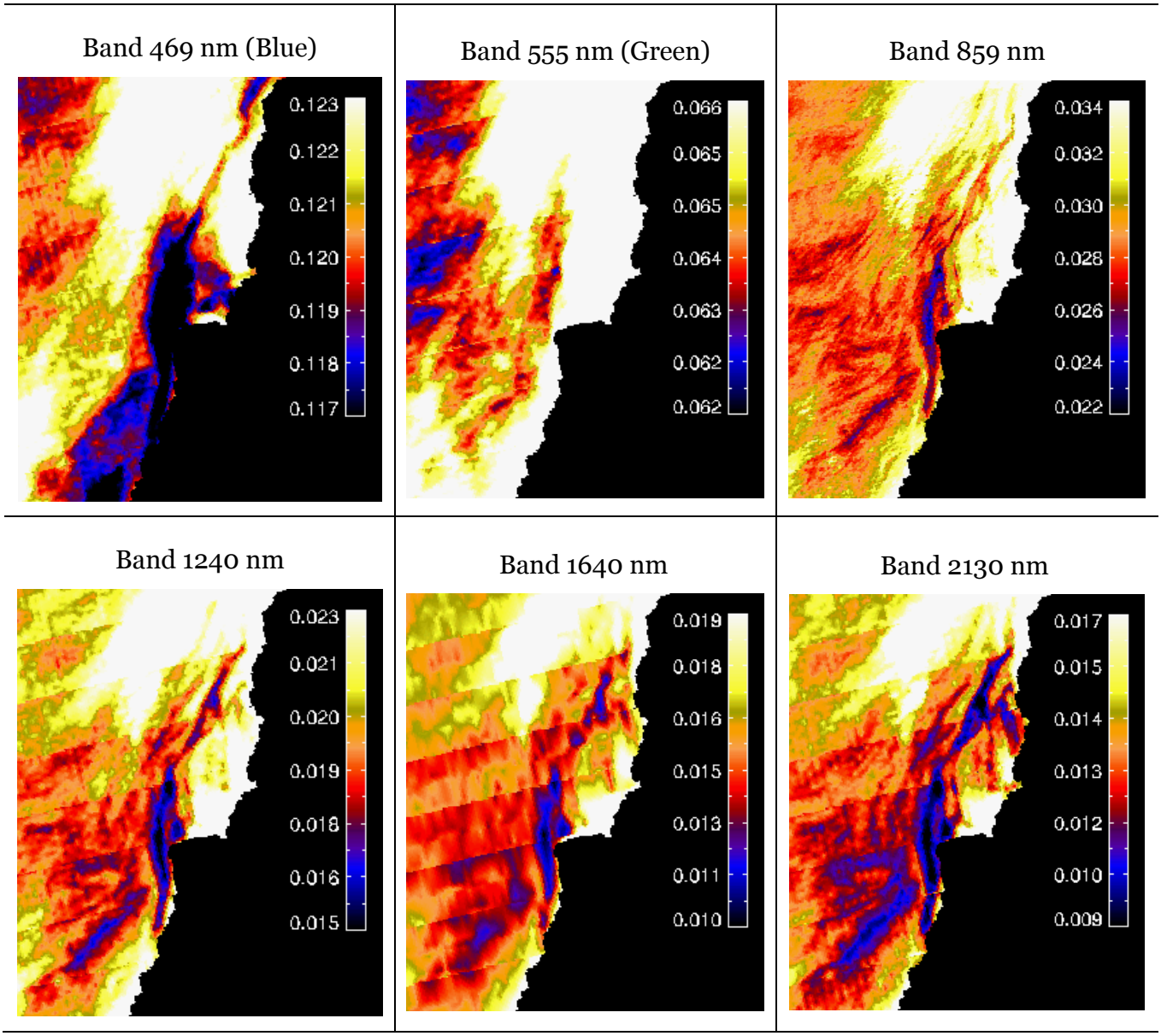

Figure 3.4 (a) ρ_t MODIS AQUA August 22, 2006, 10:25 UTC, OS detail of Lebanon coast .

(b)

$\rho_\varepsilon(\lambda)$

MODIS AQUA August 22 2006, OS detail of Lebanon coast

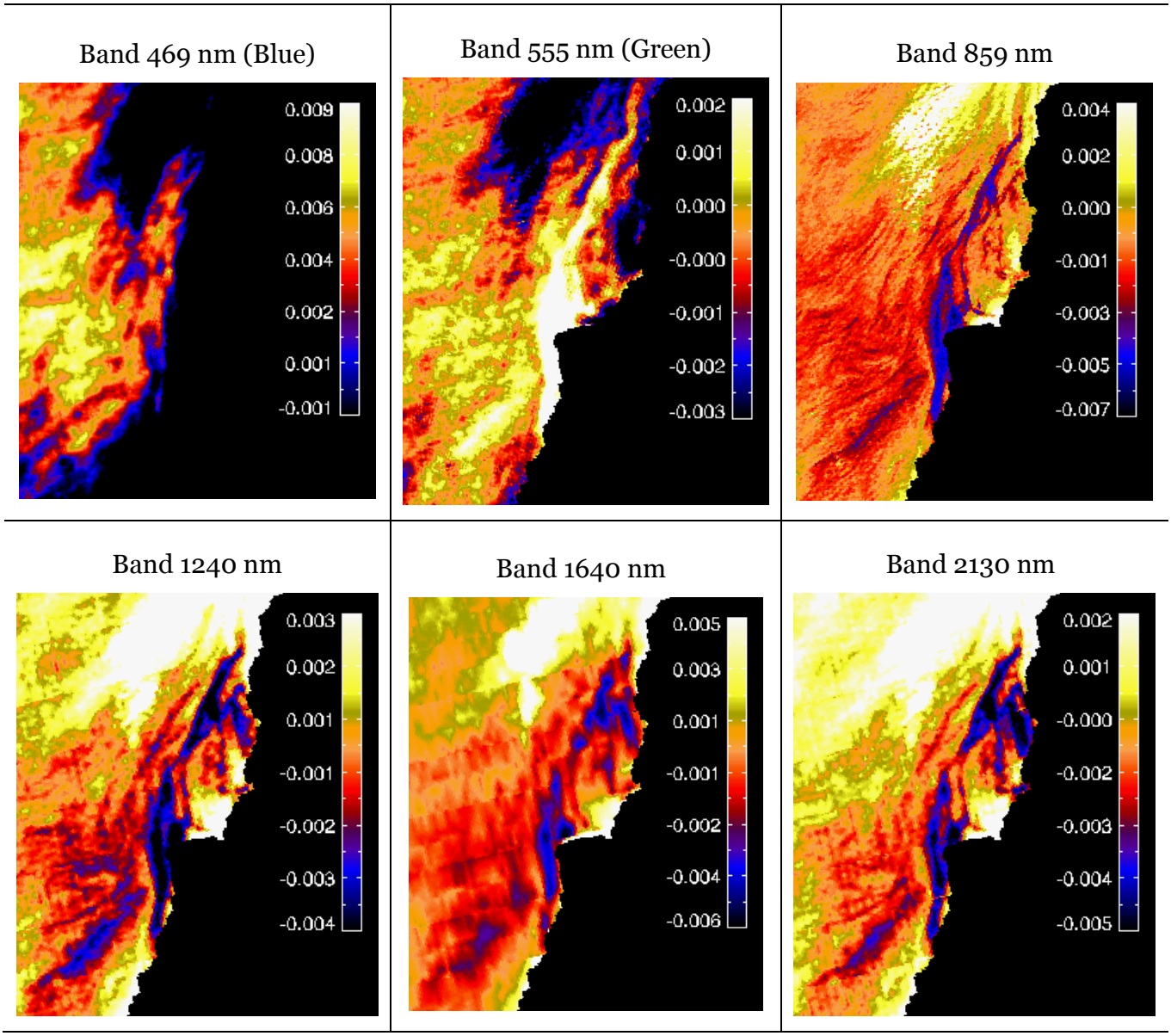

Figure 3.4 (b) ρ_ε MODIS AQUA August 22, 2006, 10:25 UTC, OS detail of Lebanon coast.

(c)

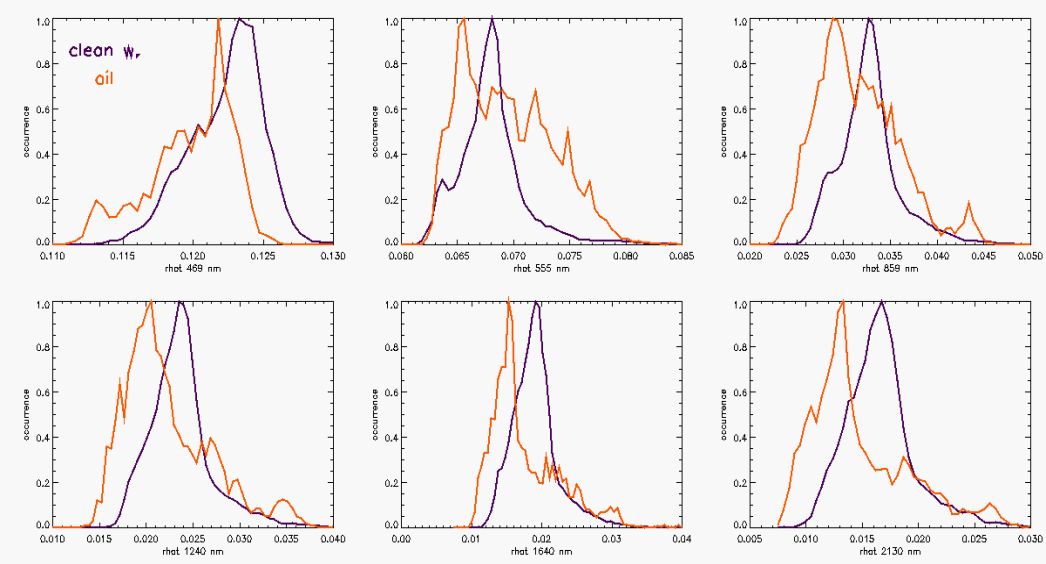

(d)

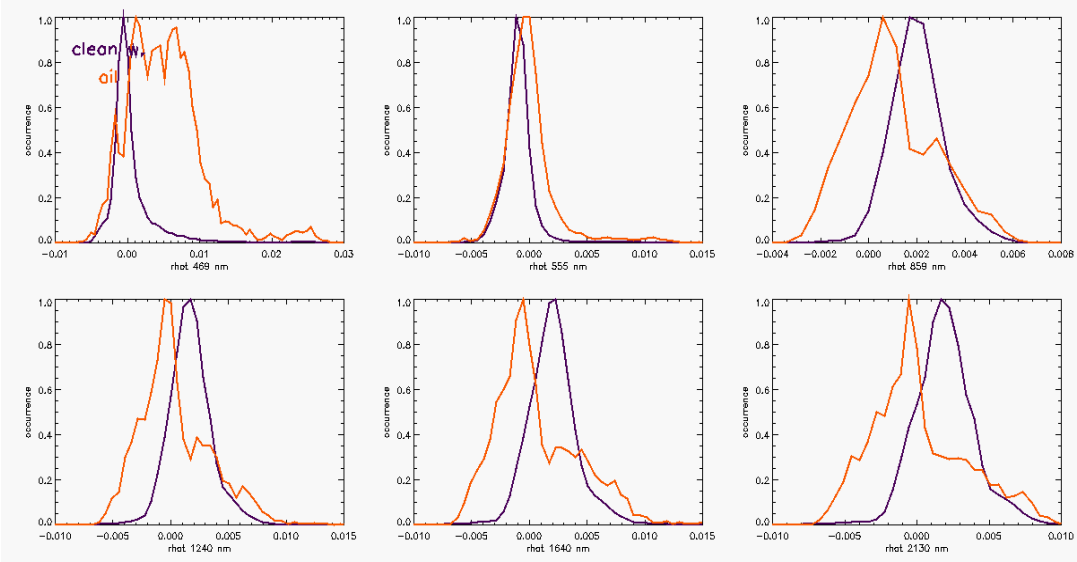

Figure 3.4 (c) ρ_t oil-water histograms **(d)** ρ_ε oil-water histograms.

(a)

$\rho_t(\lambda)$

MODIS TERRA July 23 2006, OS detail of Lebanon coast

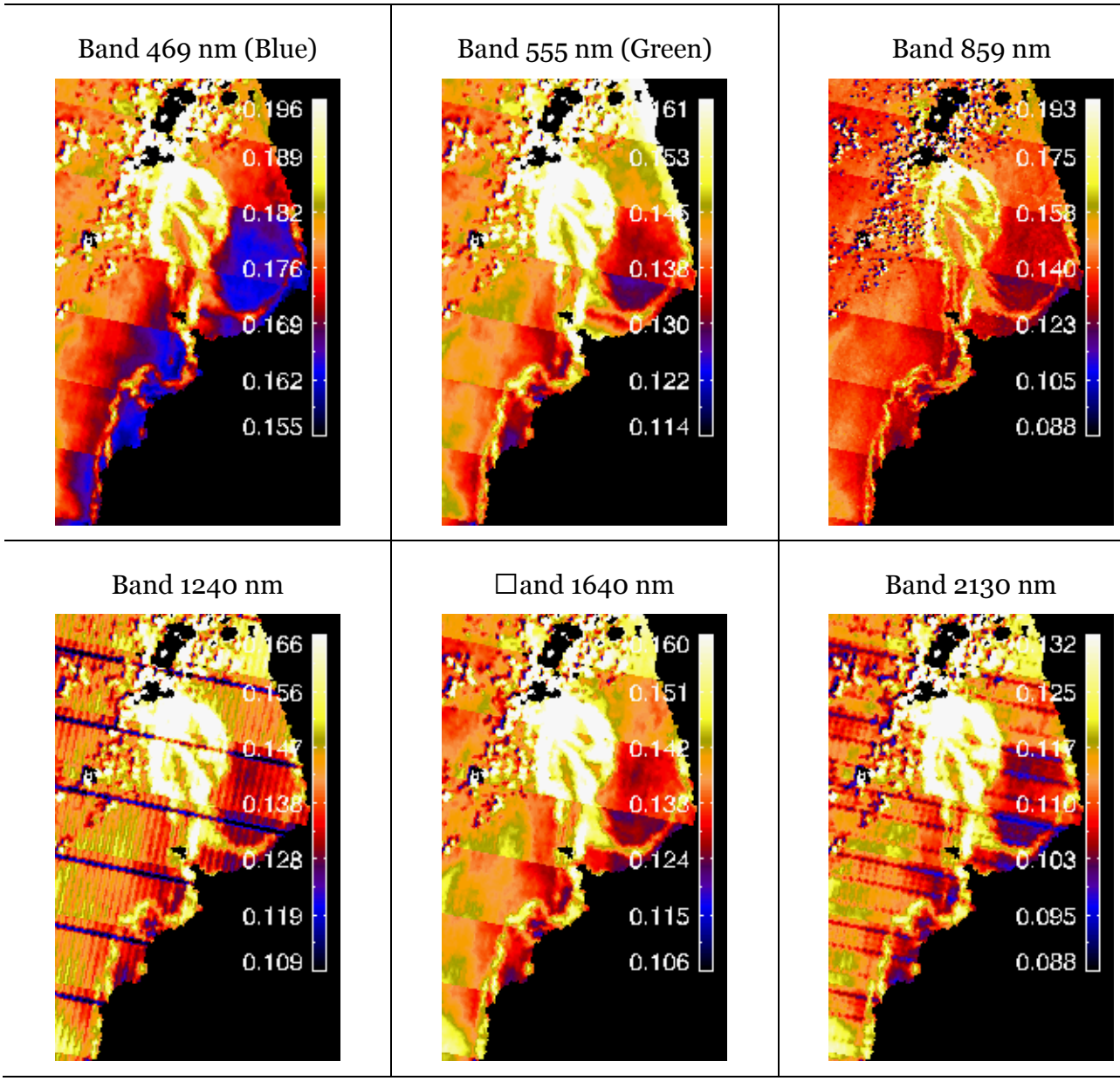

Figure 3.5 (a) ρ_t MODIS TERRA July 23, 2006, 08:35 UTC.

(b)

$\rho_\varepsilon(\lambda)$

MODIS TERRA July 23 2006, OS detail of Lebanon coast

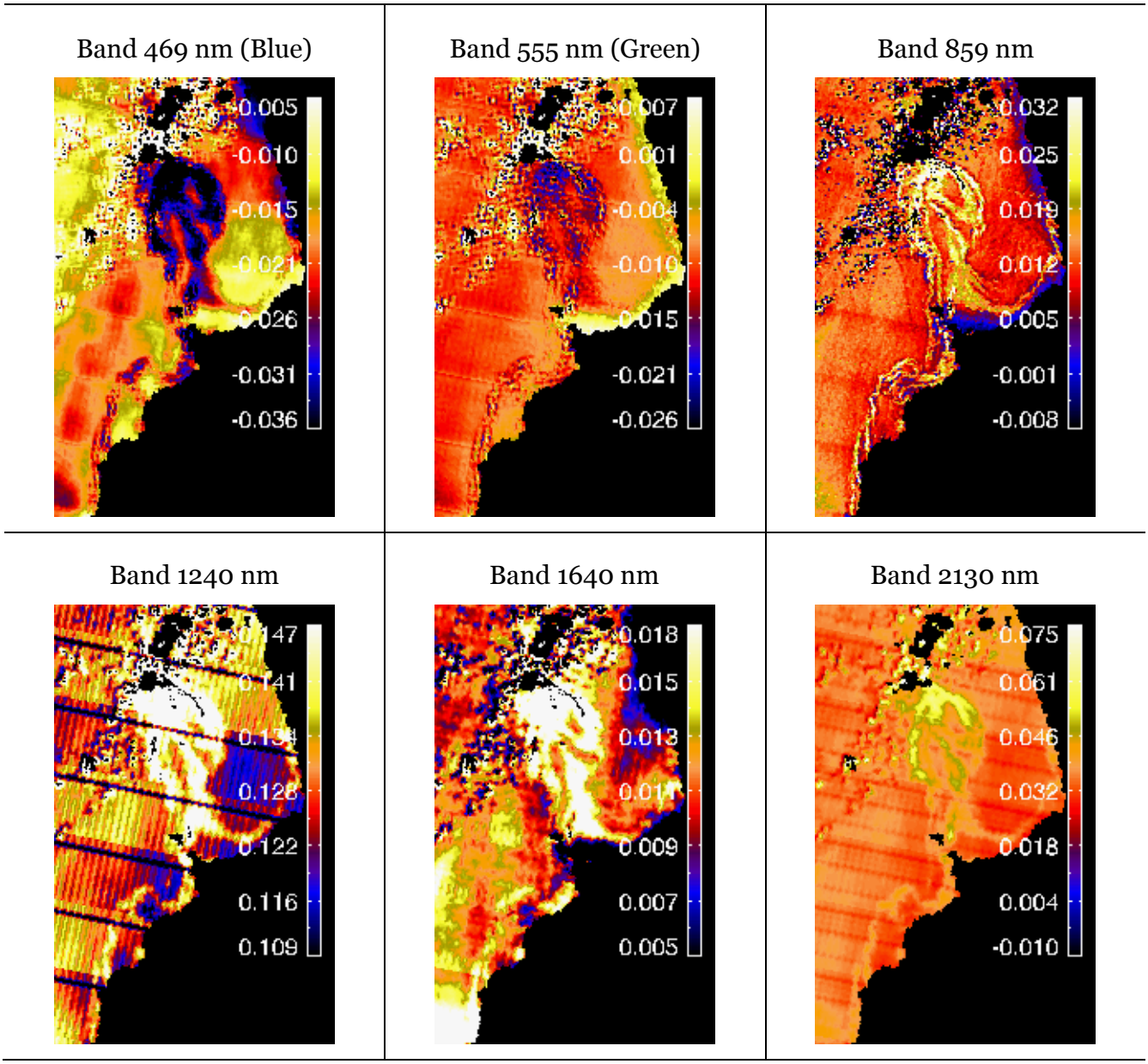

Figure 3.5 (b) ρ_ε, MODIS TERRA July 23, 2006, 08:35 UTC.

(c)

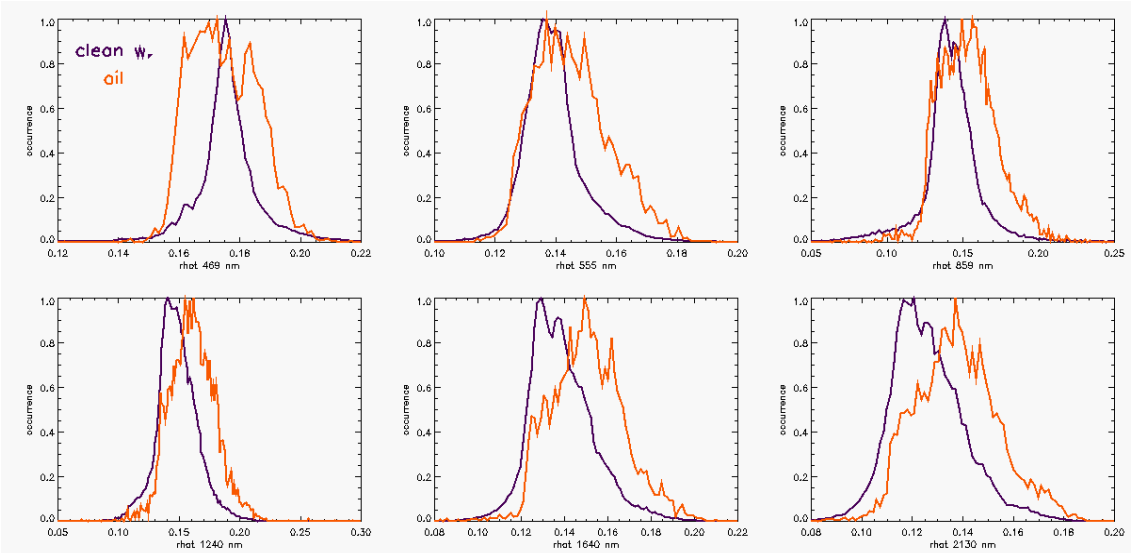

(d)

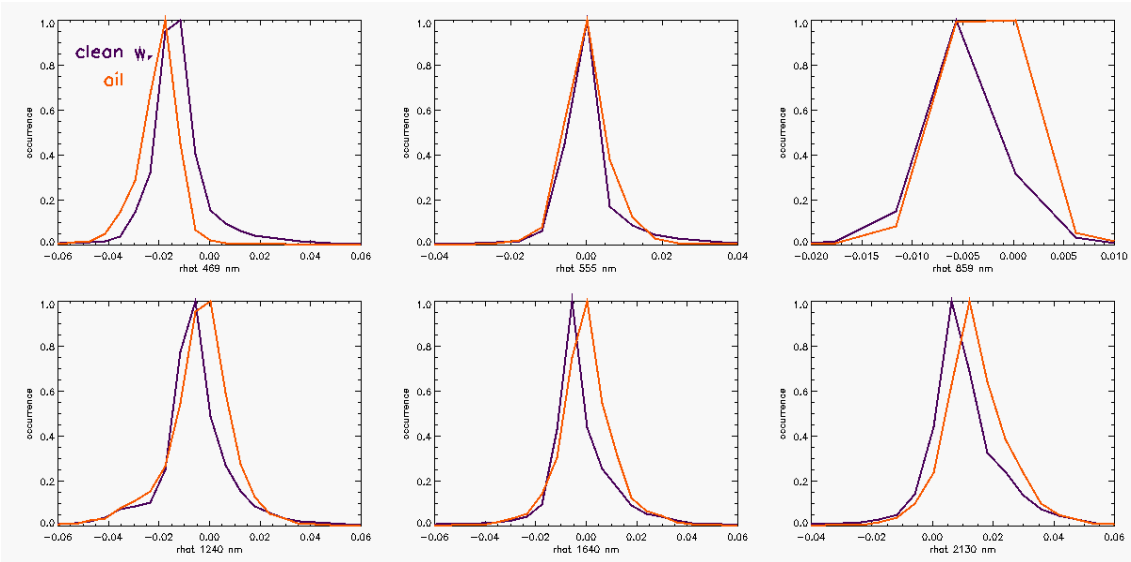

Figure 3.5 (c) MODIS TERRA July 23, 2006, (c) ρ_t oil-water histograms; (d) ρ_ε oil-water histograms.

3.2 Slick features extraction

We defined a suitable set of *features parameters* in order to characterize the oil spills and define criteria to distinguish between oil slicks and look-alikes. A first criterion is developed to classify the input examined image as low or high glint image, depending on the illumination and viewing satellite geometry. The features parameters are a mix of standard region descriptors and features tailored to oil spill detection. These have been devised and tested on a numbered of certified oil spills cases constituting the training OS database (paragraph 2.2.4). Thus, for each candidate slick a number of features is computed in order to classify it as either an oil slick or a look-alike.

3.2.1 Illumination/View analysis

A glint angle threshold was devised as high-low glint criterion. Each image pixel is classified as high or low glint pixel, depending on whether it is in specular reflection condition or not (see paragraph 2.1.4). Sun glint condition was determined by finding a threshold of the glint angle α, given by (e.g. Giglio, 2003):

$$\cos\alpha = \cos\theta_{sat}\cos\theta_{sun} - \sin\theta_{sat}\sin\theta_{sun}\cos\phi\ ,$$

where θ_v and θ_s are the satellite and solar zenith angles and ϕ is the sun-satellite relative azimuth angle, as seen from an image pixel. We determined a threshold value of $\alpha = 17.5°$, with high glint condition for $\alpha < 17.5°$ and low glint condition for $\alpha > 17.5°$. This threshold has proven to be finer that the high glint standard MODIS (and MERIS) flag (*l2_flags* product, see table 2.3), because this value of α better separates illumination-view situations in which oil slicks in TOA reflectance images are brighter than surrounding water (positive contrast) from those which are darker (negative contrast, low glint conditions). Indeed, some images classified as high glint by the MODIS flag were seen to contain both brighter and darker slicks, indicating that the flag was not sufficiently discriminatory. High and low glint cases, as distinguished by α, have been treated separately in the development of the clustering and final detection steps of the OS algorithm, because of their opposite type of contrast with surrounding water.

3.2.2 Geometric and spectral analysis

The use of standard descriptors, such as mean value, standard deviation or local contrast, didn't result suitable parameters in the oil spill characterization, i.e. to clearly distinguish OS between water, because of a lack of sufficient separation between oil and surrounding water reflectance distribution (paragraph 3.1.3). This is due to slick patchiness (verified in situ during the PRIMI cruise, chapter V), variable concentration and presence of water within the oil film itself, small thickness (mainly for spillages from ships), residual natural variability after flattening and small residual clouds. This led us to define *ad hoc* features parameters from image analysis, tailored to optical oil spill detection. We made use of a set of standard region descriptors in order to characterize the geometry and shape of the slicks, and developed a set of statistical parameters for oil reflectance distribution characterization. For each region representing a candidate slick, these parameters are defined as follows:

- **Area (A)**: Region area;
- **Perimeter (P)**: Region perimeter;
- **Shape parameters (S):**
    1. $S_1 = P / A$;
    2. $S_2 = P / 2\sqrt{\pi A}$;
    3. $S_3 = P / 4\sqrt{A}$
    4. $S_4 = 2\ln(0.25P) / \ln(A)$;
- **Cloud Vicinity (V)**: Slick distance from nearby cloud region;
- **Contrast (C)**: Ratio between mean region reflectance and mean surrounding water reflectance in a bounding box containing the slick;
- **Baricenter Reflectance**: A baricenter reflectance is the average reflectance of the region (or the surrounding water) weighted by the histogram population (figure 3.6 d).
- **Region and water reflectance histogram peak distance (dbe):** Difference between the baricenter reflectance of the OS region and surrounding water distribution histograms (figure 3.6 d).

The area (A), perimeter (P) and perimeter-area ratio (S_1) are standard geometric parameters commonly used in the methodology of oil spill detection (e.g. by SAR imagery), while the set of shape parameters (S_2, S_3, S_4) (McGarigal and Marks 1995) were specifically devised to better representing oil spill geometric structures. They in fact can take into

account the characteristic elongated shape of spills. Fractal dimension index (S_4) is appealing because it reflects shape complexity across a range of spatial scales (patch sizes). Thus, like the shape indexes (S_2, S_3), it overcomes one of the major limitations of the straight perimeter-area ratio (S_1) as a measure of shape complexity. The contrast (C) parameter is the ratio between mean candidate region reflectance and mean surrounding water reflectance, the latter being a bounding box containing the region. We expect positive (or negative) contrast for high (or low) glint scenes, depending on whether the slick is in specular reflection (high sun glint) condition or not, as defined via the glint angle α threshold criterion (paragraph 3.2.1). The cloud vicinity (V) parameter is used because cloud shadows which are darker than surrounding water maybe mistaken with oil slick structures in low glint condition. The region and water reflectance histogram peak distance (dbe) is used as spectral criterion to characterize the reflectance separation between an oil spill and its surrounding water. It is based on the definition of the baricenter reflectance of both the OS region and surrounding water and it is a finer estimation than the a mean reflectance value.

Each of these parameters was estimated for all OS regions of the training OS database and surrounding water bounding boxes. OS regions were manually digitized with the ENVI ROI tool and histograms of each parameter were also computed, as shown in figure 3.6 relative to a spill south of Elba island, northern Tyrrhenian Sea. Figure 3.6 shows an example relative to the histogram baricenter distance calculation. Table 3.1 illustrates the threshold values obtained for each parameter as result of a trial and error procedure using the oil spill database as reference.

The application of this set of parameters in oil spill selection is described in chapter IV. Mainly, for each candidate slick the set of features of table 3.1 is computed (features extraction) in order to classify the slick as either oil or look-alike. As described in chapter IV, the result of this region pruning leaves several regions that are not clearly oil spills. In the impossibility to automatically eliminate all candidates remaining after pruning, scores have been devised for a second set of distinction parameters, again computed for each region and surrounding water and making use of the OS database, some of which involve reflectance histogram integrals in order to overcome ambiguities introduced by slick patchiness (see chapter IV).

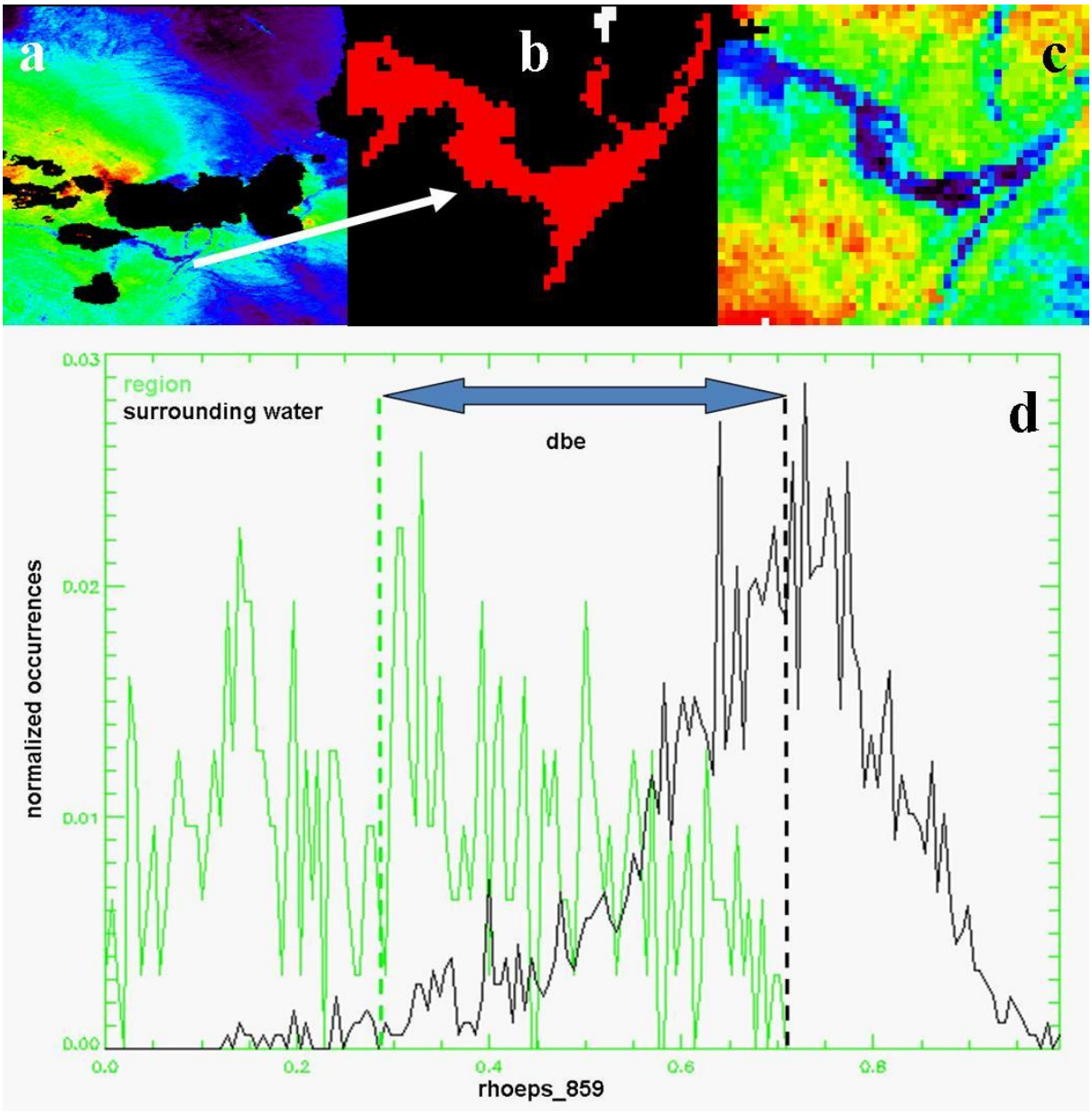

Figure 3.6 MODIS AQUA August 17 2005 12:15 UTC, low glint spill south of Elba island (northern Tyrrhenian Sea, slick in dark blue surrounded clean waters in green); (a) rhoeps band 859 nm; (b) Oil spill ROI (red) manually digitized; (c) rhoeps-859 slick detail; (d) Slick (green curve) and surrounding water (black curve) rhoeps-859 normalized distribution histograms. Dashed lines indicate histogram baricenters and blue arrow indicates baricenter distance dbe, which in this case is approximately 0.3 – 0.7 = -0.4, indicating slick to be darker than surrounding water.

Features Parameter	Threshold Value	Description
Area (A)	$1 < A < 125$ Km^2	Elimination of regions smaller than 1 and larger than 125 Km^2
Shape (S)	$0.6 < S1 > 4.$ $0.9 < S2 > 3.8$ $0.8 < S2 > 3.1$ $0.4 < S4 > 2.$	Elimination of regions shape with low values, which indicate region "roundness", thus unlikely to be oil slicks
Cloud Vicinity (V)		Elimination of regions made more brilliant by nearby cloud straylight, particularly important for high glint cases where brighter slicks may be confused with straylight affected regions
Contrast (C)		Ratio between mean region reflectance and mean surrounding water reflectance in a bounding box containing the region: positive (negative) contrast regions only are retained in high (low) glint scenes, as defined via the glint angle α threshold criterion
dbe		Regions in low (high) glint conditions are eliminated if their dbe is greater (less) than the mean dbe in the image minus (plus) one dbe standard deviation

Table 3.1 List of features parameters defined for oil spill characterization together with their threshold values.

Chapter 4

Development of Oil Spill Detection Algorithm for Optical Imagery: Clustering and Classification

Here we present and discuss the automatic OS detection techniques, i.e. image clustering and OS classification. MODIS and MERIS corrected reflectance bands (ρ_ε) are fed up to a *mean shift* procedure in order to obtain segmented regions. These regions are then pruned via a set of classification criteria. Finally, a score is assigned to each remaining region and the final result is a classification of oil spill candidate regions.

4.1 Automatic techniques for oil spill detection

The automatic OS detection technique is the application of a clustering algorithm, features extraction and final OS classification. The clustering procedure relies on the *mean shift algorithm* (Comaniciu, 1997; Comaniciu, 2002), the main idea being grouping image pixels with similar reflectance values into a set of clusters (regions) with common mode reflectance values (paragraph 4.1.1). Given the different oil /water contrast in high or moderate-low glint situations, separate clustering is performed in these two illumination situations, if present in the image. Pruning of cluster regions (paragraph 4.1.2) is achieved by means of the computation of a first set of features parameters, already defined in chapter III. Each region is retained or eliminated depending on the threshold value of its parameters. After pruning, most of obviously non-slick features (e.g. large regions) and look-alikes (e.g. slick-like regions with wrong region-water contrast) are eliminated. However, slick patchiness, residual natural variability after flattening, small residual clouds, etc., contribute to the impossibility to automatically eliminate all look-alikes with the above "clear-cut" pruning criterion. Therefore, a score is assigned to OS candidates remaining

after pruning. Scores have been devised for a second set of distinction parameters (paragraph 4.1.3).

4.1.1 Image segmentation technique

The basic computational module of the segmentation technique is a pattern recognition procedure, the *mean shift* (Comaniciu, 1997; Comaniciu, 2002), for the analysis of a complex multimodal feature space finalized to delineate shaped clusters in it. This is a nonparametric clustering technique for estimation of the density gradient, which does not require prior knowledge of the number of clusters, and does not constrain the shape of the clusters. Image pixels are regarded as samples from an unknown probability density function, and a mean shift vector is defined, at a given pixel, as parallel to the local maximum reflectance gradient, with length equal to a search radius determined as a fraction of the image's reflectance histogram standard deviation. The pixel reflectance is then ideally substituted with the reflectance of the pixel at the vector's point. The operation is repeated until a point is found where the reflectance gradient is zero and the shift stops. The final "arrival" reflectance value, the cluster's mode reflectance, is assigned to each pixel converging there in the shift process. The ensemble of pixels with the same mode constitute the cluster itself and each cluster is, in Euclidean space, in general formed by a set of disjointed regions. Finally, modes which are closer than a threshold value (to be determined on the basis of reflectance variability in the image) are pruned, as done in generic feature space analysis, and pruned mode pixels are assigned to the most populated and closest mode cluster.

Mean Shift Procedure

In general, given n data points (pixels in our case) x_i, $i = 1, \ldots, n$ on a d-dimensional space R^d, the multivariate kernel density estimate obtained with kernel $K(x)$ and window radius h is:

$$f(x) = \frac{1}{nh^d} \sum_{i=1}^{n} K\left(\frac{x - x_i}{h}\right). \quad (4.1)$$

For radially symmetric kernels, it suffices to define the profile of the kernel $K(x)$ satisfying

$$K(x) = c_{k,d}\, k(\| x \|^2), \quad (4.2)$$

where $c_{k,d}$ is a normalization constant which assures that $K(x)$ integrates to 1. Employing the profile notation, the density estimator (4.1) can be rewritten as:

$$f_{h,K}(x) = \frac{c_{k,d}}{nh^d} \sum_{i=1}^{n} k\left(\| \frac{x - x_i}{h} \|^2 \right). \qquad (4.3)$$

The modes of the density function are located at the zeros of the gradient function $\nabla f(x) = 0$ and the mean shift procedure is a way to locate these zeros without estimating the density. The gradient of the density estimator f(x) is:

$$\nabla f_{h,K}(x) = \frac{2c_{k,d}}{nh^{d+2}} \sum_{i=1}^{n} (x_i - x) g\left(\| \frac{x - x_i}{h} \|^2 \right)$$
$$= \frac{2c_{k,d}}{nh^{d+2}} \left[\sum_{i=1}^{n} g\left(\| \frac{x - x_i}{h} \|^2 \right) \right] \left[\frac{\sum_{i=1}^{n} x_i g\left(\| \frac{x - x_i}{h} \|^2 \right)}{\sum_{i=1}^{n} g\left(\| \frac{x - x_i}{h} \|^2 \right)} - x \right], \qquad (4.4)$$

where g(s) = -k´(s). The first term is proportional to the density estimate at x computed with kernel $G(x) = c_{g,d}\, g(|| x^2 ||)$ and the second term

$$m_{h,G}(x) = \frac{\sum_{i=1}^{n} x_i g\left(\| \frac{x - x_i}{h} \|^2 \right)}{\sum_{i=1}^{n} g\left(\| \frac{x - x_i}{h} \|^2 \right)} - x, \qquad (4.5)$$

is the *mean shift*, that is the difference between the weighted mean, using the kernel G for weights, and x, the center of the kernel (window). We can rewrite the above formula as

$$\nabla f_{h,K}(x) = f_{h,G}(x) \frac{2c_{k,d}}{h^2 c_{g,d}} m_{h,G}(x), \qquad (4.6)$$

yielding

$$m_{h,G}(x) = \frac{1}{2} h^2 c \frac{\nabla f_{h,K}(x)}{f_{h,G}(x)}. \qquad (4.7)$$

The mean shift vector always points toward the direction of the maximum increase in the density. So, the local mean is shifted toward the region in which the majority of the points

reside. Since the mean shift vector is aligned with the local gradient estimate, it can define a path leading to a stationary point of the estimated density. The mean shift procedure, obtained by successive

- Computation of the mean shift vector $m_{h,G}(x)$, according to 4.5;
- Translation of the kernel (window) $G(x)$ by $m_{h,G}(x)$, $x_{j+1} = x_j + m_{h,G}(x_j)$,

is guaranteed to converge at a nearby point where the estimate (4.3) has zero gradient, that is, the magnitude of the mean shift vector converges to zero and, at the limit, $m_{h,G}(x_c) = 0$.

Using the normal kernel

$$K(x) = (2\pi)^{-d/2} \exp\left(-\frac{1}{2} \| x \|^2\right) \qquad (4.8)$$

the jth mean shift vector is given by

$$m_h(x_j) = x_{j+1} - x_j = \frac{\sum_{i=1}^{n} x_i \exp\left(\| \frac{x - x_i}{h} \|^2\right)}{\sum_{i=1}^{n} \exp\left(\| \frac{x - x}{h} \|^2\right)} - x_j \,. \qquad (4.9)$$

The mean shift clustering algorithm is a practical application of the mode finding procedure: the set of all locations that converge to the same mode defines the *basin of attraction* of that mode. The points which are in the same basin of attraction are associated with the same cluster. In particular, let x_i, $i = 1, \ldots, n$, be the d-dimensional input pixels in the joint spatial-range domain. For each pixel,

1. Initialize $j = 1$ and $y_{i,1} = x_i$
2. Compute $y_{i,j+1}$ according to (4.9) until convergence, $y = y_{i,c}$
3. Assign $z_i = (x_i^s, y^r_{i,c})$

The superscripts s and r denote the spatial and range components of a vector, respectively. The assignment specifies that the filtered data z_i at the spatial location x_i^s will have the range component of the point of convergence $y^r_{i,c}$.

Image Segmentation

The image segmentation is a straightforward extension of the above algorithm. Each pixel is associated with a *significant* mode of the joint domain density located in its neighborhood, after nearby modes were pruned. In particular, let x_i, $i = 1, ...,n$, be the d-dimensional input image pixel in the joint spatial-range domain and L_i the label of the ith pixel in the segmented image. Then run the mean shift filtering procedure for the image and store all the information about the d-dimensional convergence point in z_i, i.e., $z_i = y_{i,c}$. Delineate in the joint domain the clusters $\{\boldsymbol{C}_p\}_{p = 1...m}$ by grouping together all z_i which are closer than h in the range domain, i.e., concatenate the basins of attraction of the corresponding convergence points.

For each $i = 1, ..., n$ assign $L_i = \{p \mid z_i \in \boldsymbol{C}_p\}$. A region is therefore defined by all the pixels associated with the same mode in the joint domain.

The input are the corrected reflectance bands ρ_ε and the d-dimensional space is the reflectance space. We tested the algorithm ranging from 1-d to 7-d components per pixel (e.g., 469, 555, 645, 859, 1230, 1640, 2130 nm for MODIS imagery). We saw that the best results are obtained working with only one band or running the algorithm separately for each band. An example of clustered image is given in figure 4.1 (b). Each color represents a cluster region. The next step is to classify all of these regions as either oil slicks or look-alikes.

ρ_ε (859 nm)

MODIS AQUA, August 22, 2006, 10:25 UTC.

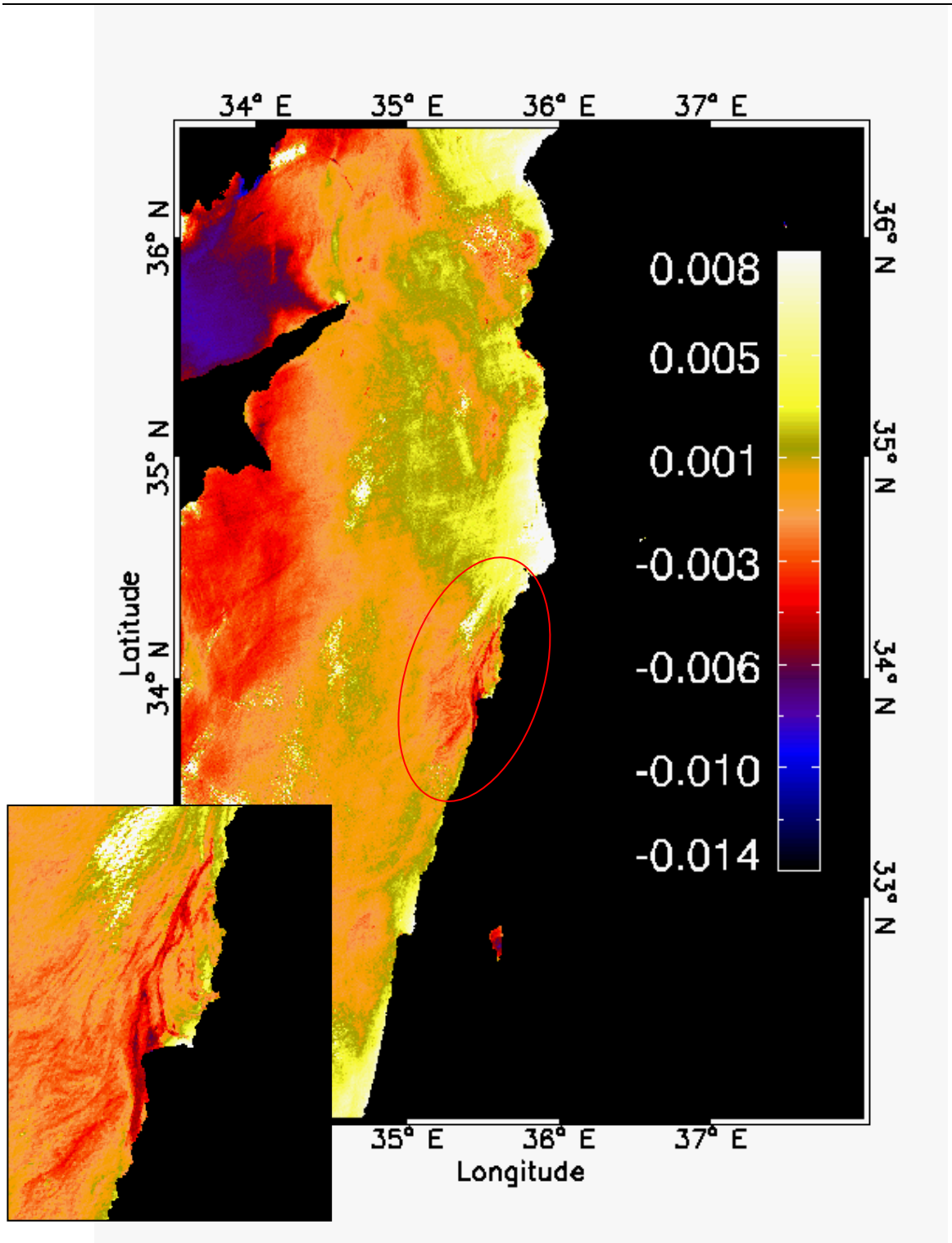

Figure 4.1 (a) MODIS AQUA (August 22 2006 10:25 UTC), 859 nm band ρ_ε. Lebanon coastal oil spill in low glint condition (slick evidenced by red ellipse).

Cluster Matrix of ρ_ε (859 nm)

MODIS AQUA, August 22, 2006, 10:25 UTC.

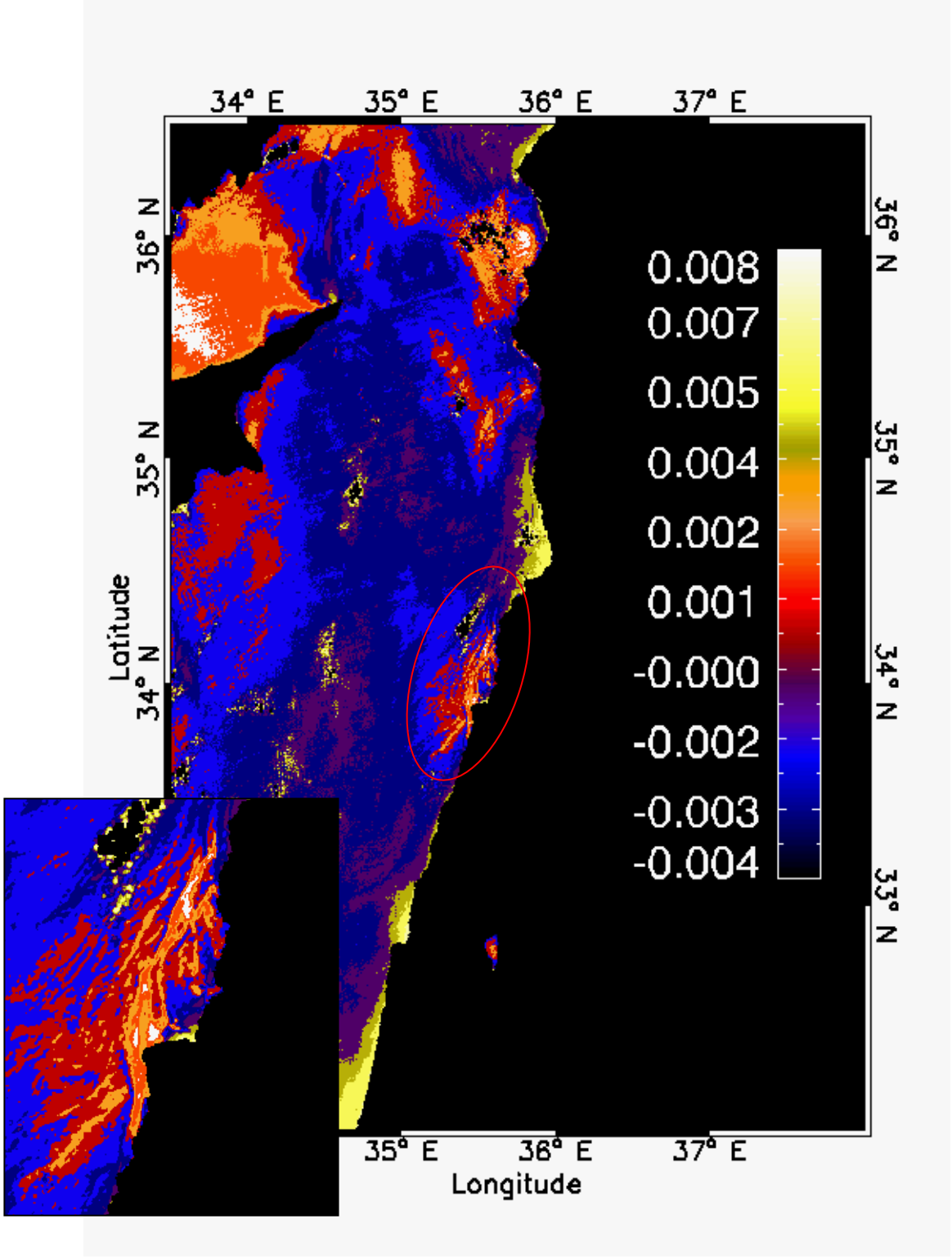

Figure 4.1 (b) MODIS AQUA (August 22 2006 10:25 UTC), ρ_ε (859) cluster matrix. The clustering procedure found 10 clusters (different colors correspond to different reflectance mode values).

Bandwidth Selection

The quality (resolution) of segmentation is controlled by the bandwidth parameter *h*, associated with the kernel density estimator (4.1), defining the radius of the search windows in the reflectance domain. Greater values of *h* will result in coarse segmentation with a few number of clusters; lower values will result in a more detailed segmented image with increased number of clusters. We defined our optimal bandwidth as the bandwidth that achieve the best compromise between the variances of the peaks of histograms computed at each clustering step.

Indeed, *h* was previously determined as a fraction of the reflectance histogram's standard deviation, as in figure 4.2 (a) and was maintained constant for the determination of all clusters (figure 4.2 b). We re-estimated *h* after each mode (cluster) determination (figure 4.2 c and d) in the following way:

1. After determining the *i-th* mode, the image is pruned of the *i-th* cluster pixels;
2. The histogram is then recomputed (figure 4.2 b);
3. The histogram is searched for wide population gaps and (eventually) subdivided into sub-histograms (figure 4.2 c);
4. The standard deviation is computed for each sub-histogram (figure 4.2 c);
5. *h* for *i*th cluster determination is computed as a fraction of the average of these standard deviations.

Bandwidth Selection

(a)

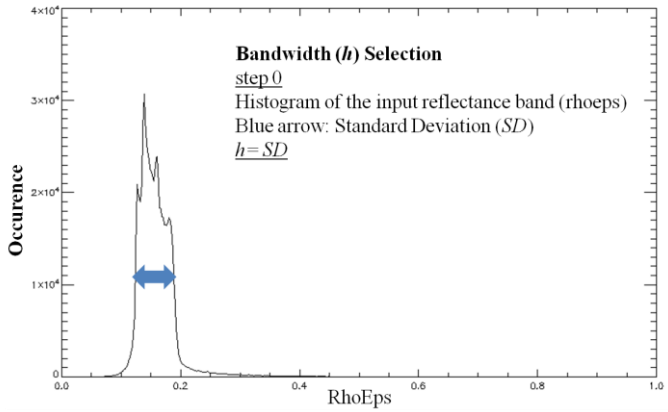

(b)

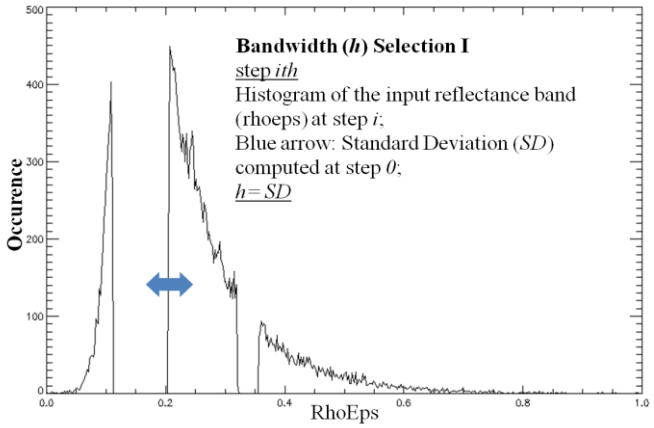

(c)

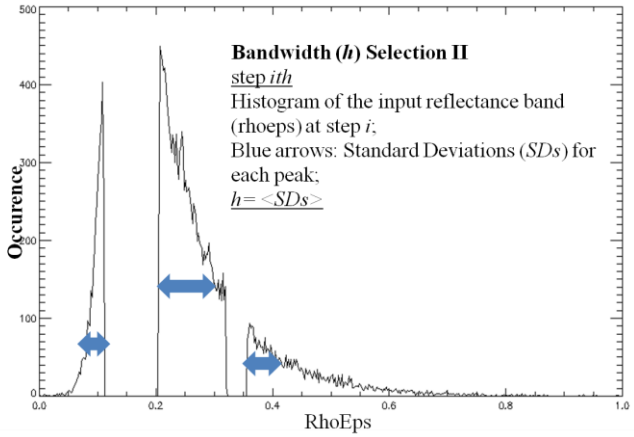

Figure 4.2 (a) Histogram of initial image, blue arrow indicates standard deviation; **(b)** histogram before *ith* cluster determination, with same constant deviation, thus constant search radius *h*; **(c)** same as **(b)** but with separate standard deviations for each sub-histogram (blue arrows) which will determine new *h*.

4.1.2 Oil spill candidate classification I: slick features extraction

The clustered image of figure 4.1 (b) shows how some regions are patently not oil slicks, e.g. the very large open sea dark grey regions or the small white specks, which are cloud residuals. These regions with "roundish" shape or "wrong" contrast, i.e. brilliant (dark) regions in low (high) glint conditions can be easily eliminated. This is done via the application of the set of parameters defined in table 3.1 (charter III). Features extraction is performed for each cluster region. Each region is maintained or eliminated depending on the values assumed by its features. For example, if the area parameter (A) of a region exceeds the threshold values defined in table 3.1, i.e. $A < 1$ Km^2 or $A > 125$ Km^2, it is eliminated, otherwise retained. The result of this region pruning process for the cluster matrix of figure 4.1 (b) is shown in figure 4.1 (c). As can be seen, however, there are too much remaining regions that are not clearly oil slicks. We define such regions as "OS candidates".

To date, the mostly empirical effort to develop the parameters for look-alike elimination has revealed that there seems not to be a clear-cut selection criterion to distinguish OS's from look-alikes. Region-water reflectance contrast may be used in visual/manual qualitative OS detection but is not sufficient for automatic detection, and does not assure that darker or more brilliant and features are actually OS's. The physical reason for the absence of clear-cut separation criterion lies in the fact that oil spills are patchy, and this was confirmed during the validation cruise (see chapter V). Oil concentration on the surface, even within a small oil slick detected by a high resolution SAR satellite image, may vary from virtual absence of hydrocarbon to a thin film which sufficiently suppresses capillary waves, to heavily polluted brown or black waters with floating hydrocarbon solid particles of variable dimensions. This patchiness has a spatial variability scale inferior to the MODIS, MERIS or even SAR pixel size. Consequently, reflectance from a pixel within an OS is often an average reflectance resulting from a mix of the above pollution situations. Moreover, "clean" water pixels surrounding an OS may actually be affected by slight pollution. Finally, the OS digitizing, the flattening and declouding processes are not perfect and residuals of clouds or natural surface variability may still be present, which is the fundamental reason for which look-alikes exist, e.g. as darker patches in low glint scenes.

These facts induced us to re-analyze the OS candidate regions issuing from the above pruning process (figure 4.1 c) with a second set of parameters and to define scores for each parameter applied to each OS candidate.

OS Candidate Matrix (859 nm)

MODIS AQUA, August 22, 2006, 10:25 UTC.

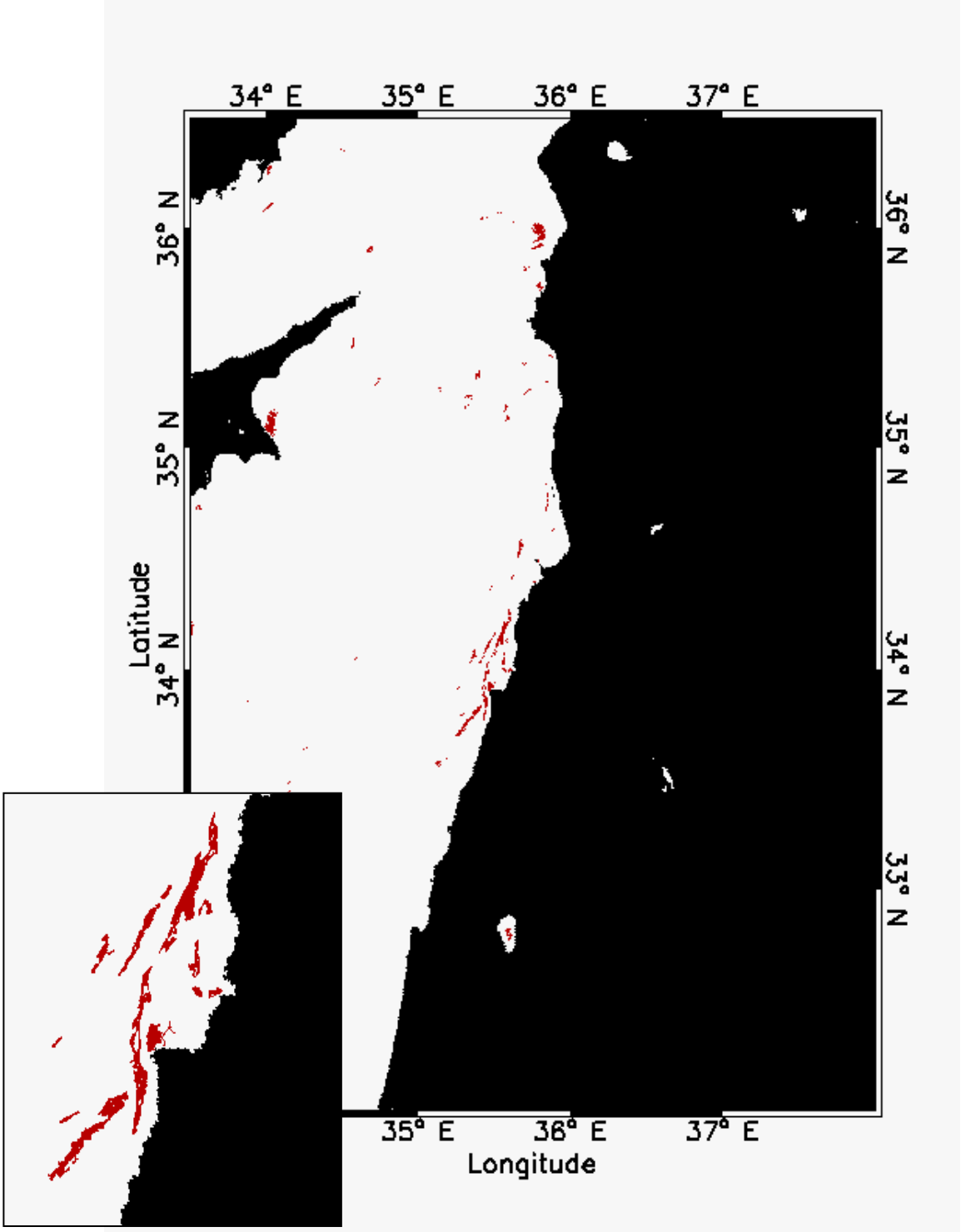

Figure 4.1 (c) MODIS AQUA (August 22 2006 10:25 UTC), OS candidate matrix. The OS selection procedure has leaved 68 regions, as candidate oil spills.

4.1.3 Oil spill candidate classification II: automatic score assignment

Score look-up table (LUT) computation

We defined a second set of features descriptors in order to build a score look-up table via the following parameters:

- **dbe**: This parameter is again taken into consideration (see table 3.1), now for score computation;
- **d4r**: Total population of the darkest quarter of the OS candidate region histogram (integral from the minimum reflectance to a fourth of the reflectance range covering the region and surrounding water histograms, figure 4.3);
- **l4r**: Total population of the brightest quarter (from 3/4 to the maximum reflectance of the above range) of the OS candidate's reflectance histogram (figure 4.3)
- **d4w** and **l4w**: The above for the surrounding water histogram (figure 4.3);
- **(d4r – d4w)/max(d4r, d4w)**: This ratio is equal to 1 when the darkest quarter of the reflectance range is only populated by the OS candidate region histogram; no surrounding water in this range implies d4w = 0. Contrarily, the ratio is equal to -1 when only populated by surrounding water (thus, d4r = 0). In practice this parameter tells us how much more the darker range of the histogram is populated by the OS candidate than by water which means that, in the case of no glint conditions, then candidate is a probable oil spill;
- **(l4r – l4w)/max(l4r, l4w)**: The same for the brighter quarter of the histogram reflectance range; values close to 1 in a high glint case probably indicate an OS;
- **dref**: The average reflectance distance between the OS candidate and water histogram integral curves (figure 4.4); this parameter indicates how much an OS candidate region is "globally" darker or brighter than surrounding water.

In order to overcome ambiguities introduced by slick patchiness, which may bias contrast conceived as region/water mean reflectance ratio, most of these parameters involve reflectance histogram integrals. These "integral" parameters enable us to tell whether a region is statistically darker or lighter than surrounding water.

Each parameter was estimated for all oil spill regions, look-alikes and surrounding water bounding boxes of our training OS database (15 OS cases). Histograms of each parameter (P) distribution were computed, both for known OS's ($H_{OS}(P)$) and known look-alikes ($H_{LA}(P)$). Figure 4.5 (a) shows an example relative to the histogram baricenter

distance (dbe) for all low glint OS and look-alikes of our training OS database. A 0 to 1 score value for each parameter was defined as (figure 4.5 b):

$$S(P) = H_{OS}(P)/(H_{OS}(P)+ H_{LA}(P)) .$$

Score assignment to selected oil spill candidates

For each selected OS candidate in a new image:

1) values P are computed for all score parameters;
2) Score values S(P) are found in the LUT;
3) Final score is issued as a linear combination of single-P scores.

That is, the score is higher if a high number of OS's have a given parameter value compared to the number of look-alikes with the same value. A cumulative score is then computed by adding single parameter scores and normalizing to 1. The parameters for score computation are still under evaluation, as well as single score weighting in cumulative score computation. Figure 4.1 (d) shows the score matrix relative to the Lebanon coastal spill of figure 4.1 (a). Each color represents a score value, from 0 to 1.

We conclude with two examples relative to the Lebanon oil spill event which summarize the main steps of the presented OS detection methodology. Figures 4.6 (a) and 4.7 (a) are the input reflectance bands ρ_t (859/865) containing the oil spill to be detected, the former relative to MODIS TERRA and the latter to MERIS sensor, both in high glint condition. The image flattening procedure gives the corresponding flattened ρ_ε(859/865) bands (figures 4.6 (b) and 4.7 (b)) which follow the OS detection procedure. The automatic detection results are showed in figures 4.6 (c) and 4.7 (c), in which are clearly visible oil spill regions and look-alikes, i.e. all candidate oil spills. Finally, figures 4.6 (d) and 4.7 (d) show all candidate regions with their associated score values. It is to be noted how look-alikes have an assigned score much smaller than the score associated to the actual slick region.

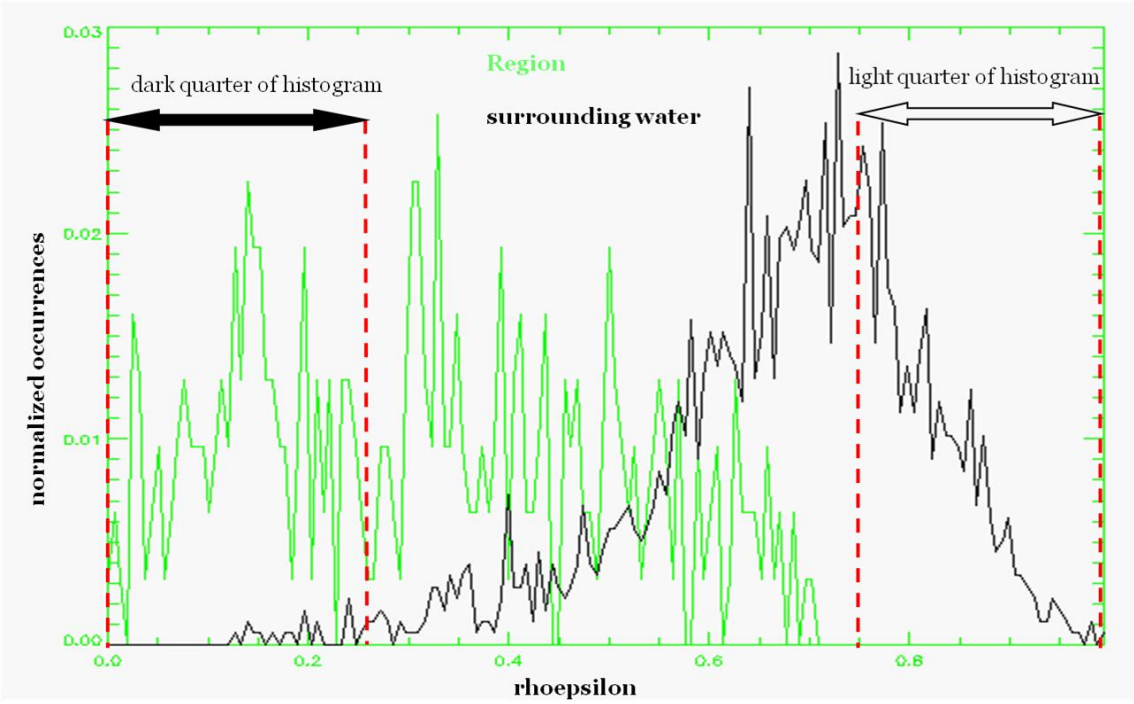

Figure 4.3 Slick (green curve) and surrounding water (black curve) $\rho_\varepsilon(859)$ normalized distribution histograms, with histogram regions used for computation of d4r, d4w (histogram integrals on dark quarter) and l4r, l4w (histogram integrals on light quarter).

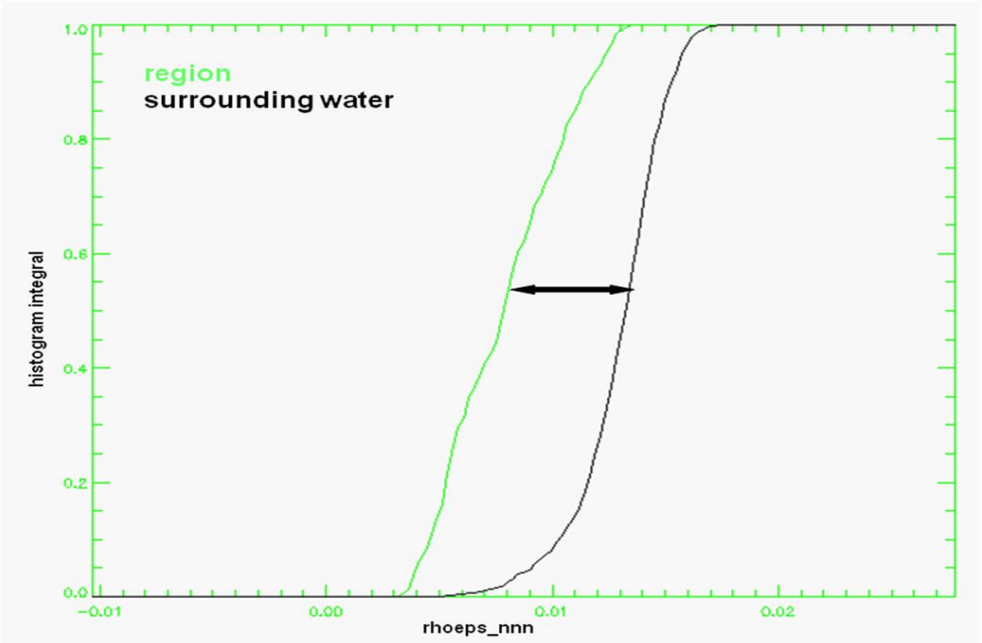

Figure 4.4 Slick (green curve) and surrounding water (black curve) $\rho_\varepsilon(859)$ normalized histogram integral functions. Black arrow shows reflectance distance between curves for a given integral value and dref is the average distance

(a)

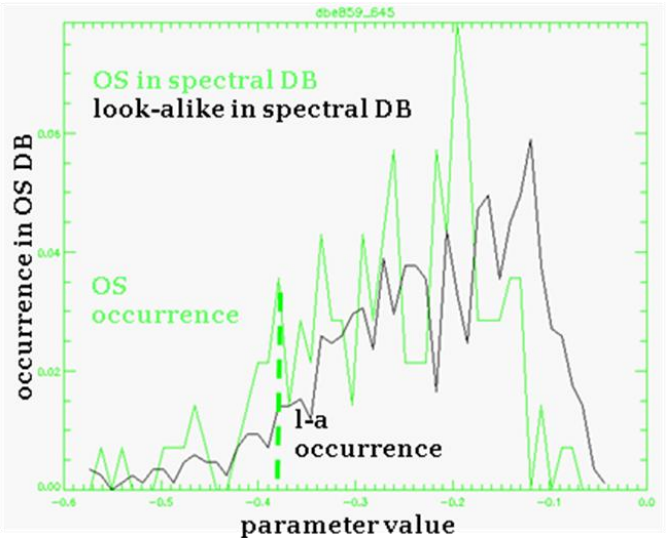

(b)

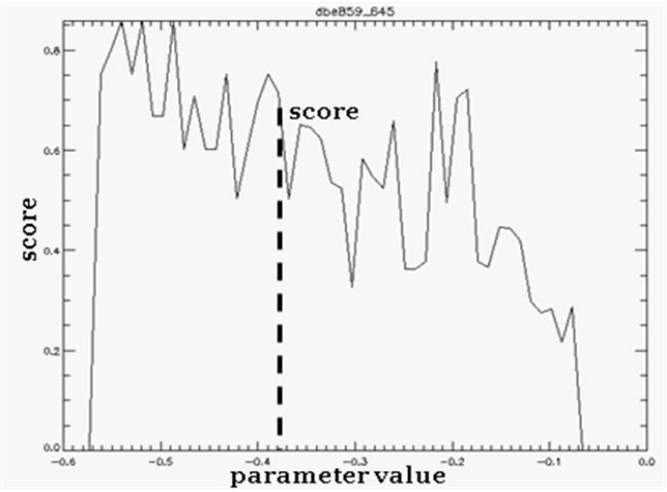

Figure 4.5 (a) Certified OS (green curve) and look-alike (black curve) dbe distribution for all no-glint images in the OS database. (b) Score for dbe values, regions with dbe's corresponding to high (low) score values will be classified as more probable oil spills (look-alikes). Similar scores are obtained for the high glint OS – look-alike database.

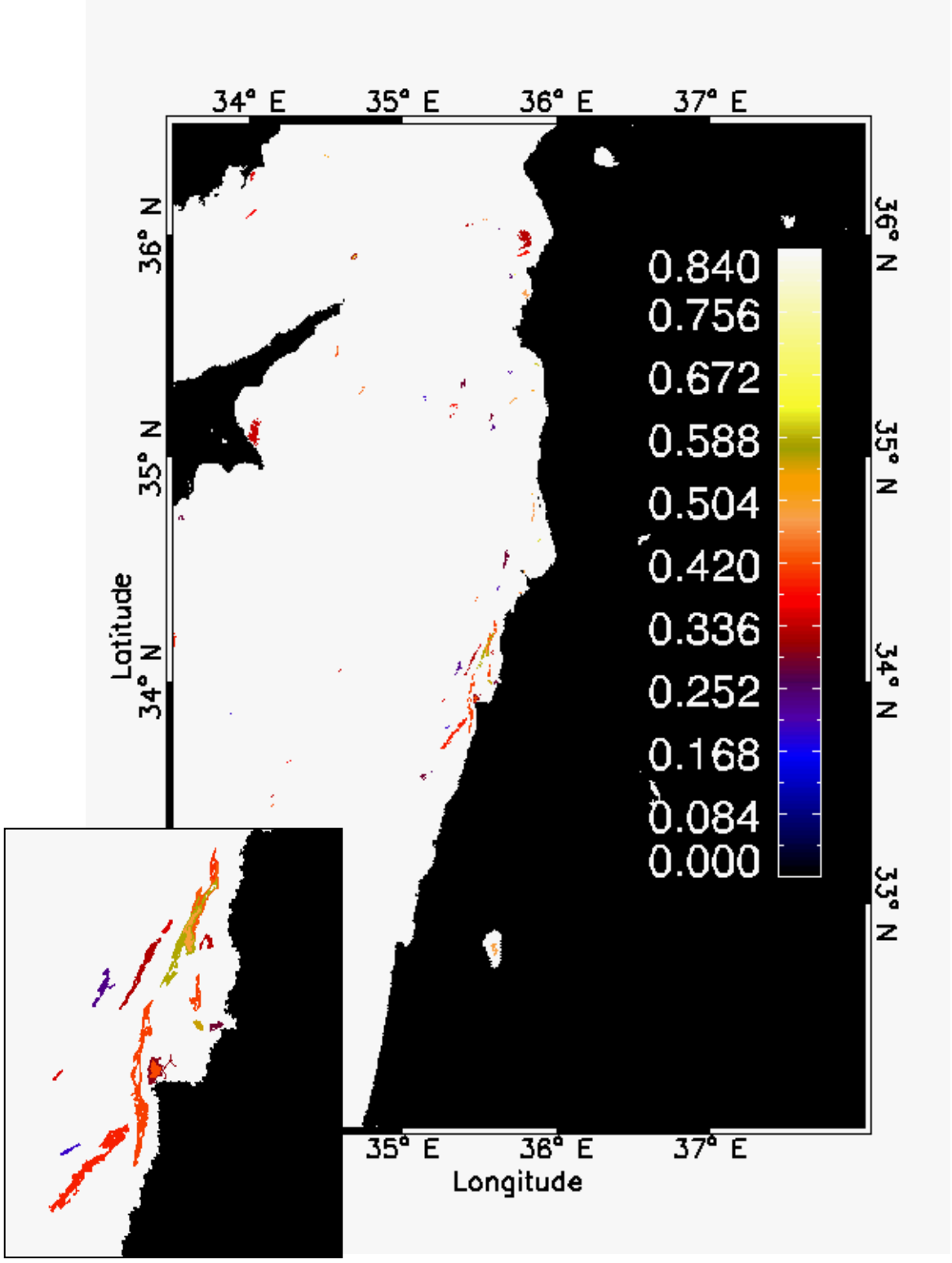

Figure 4.1 (d) MODIS TERRA (July 23 2006 08:30 UTC) OS Score Matrix. Different colors correspond to different score values from 0 to 1.

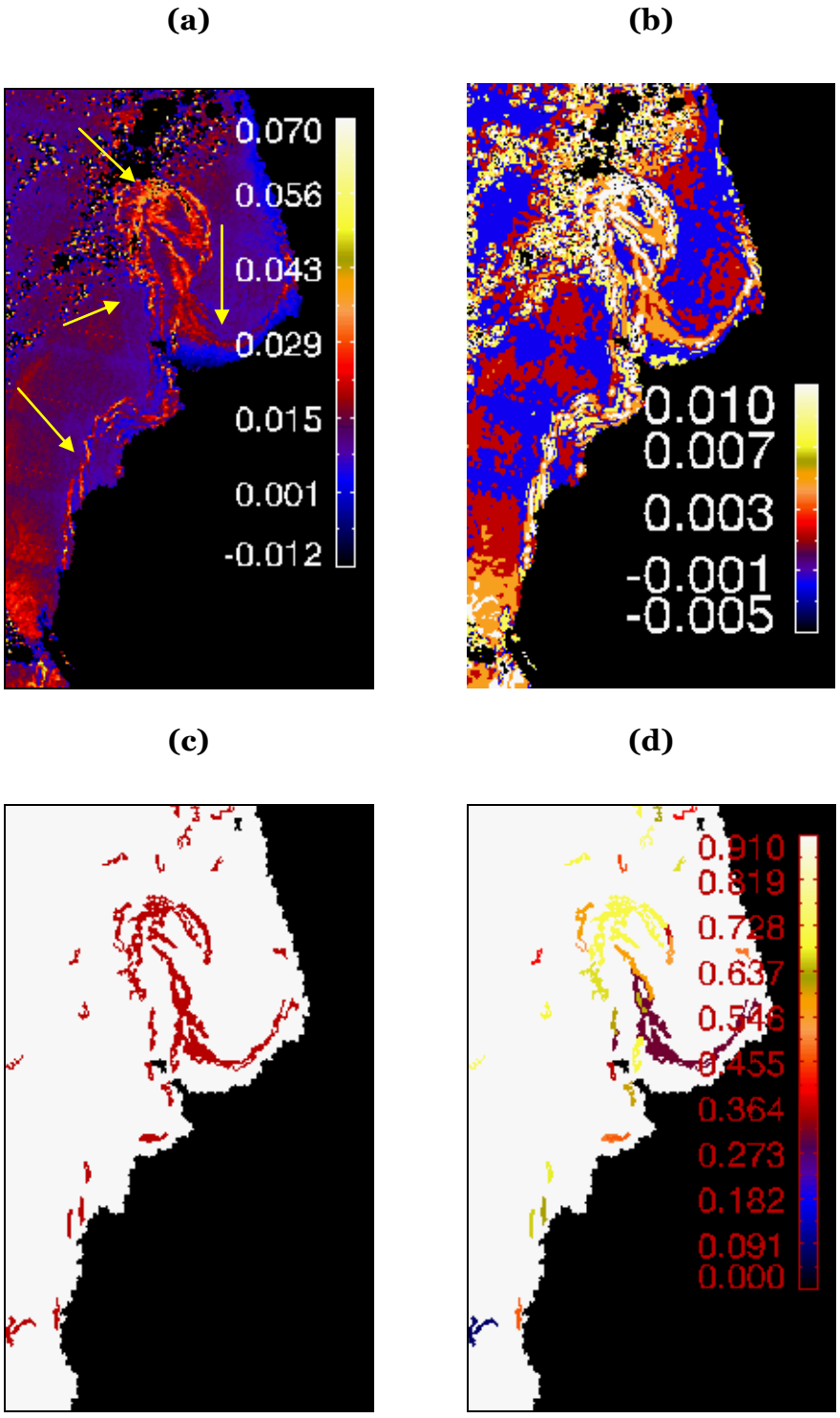

Figure 4.6 (a) MODIS reflectance band ρ_t (859) containing the oil spill to be detected. **(b)** ρ_ε (859)obtained by image flattening procedure. **(c)** OS candidate Matrix: 31 candidate oil spills **(d)** OS Score Matrix: each region has associated a score value from 0 to 1.

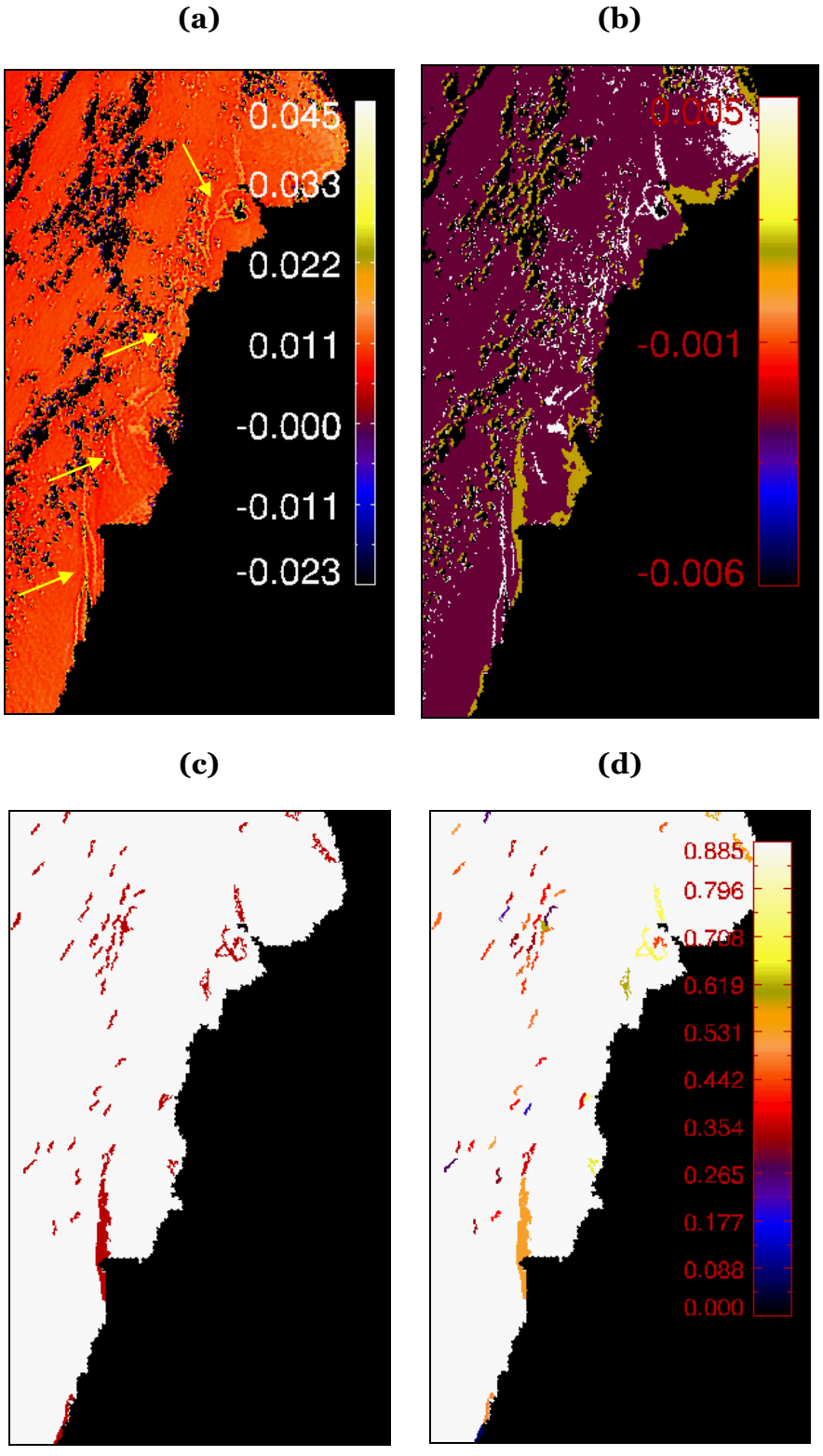

Figure 4.7 (a) MERIS reflectance band ρ_t (865) containing the oil spill to be detected. **(b)** ρ_ε (865)obtained by image flattening procedure. **(c)** OS candidate Matrix: 54 candidate oil spills **(d)** OS Score Matrix: each region has associated a score value from 0 to 1.

Chapter 5

Oil Spill Detection Algorithm: Validation and Application

Here we present the validation of the developed oil spill (OS) detection algorithm by the application of this to a number of certified oil spill events for which optical images (observations) were available and used as reference test cases by comparing the observed oil spills with those automatically detected by our OS detection algorithm. Finally, we report some experimental result with particular regards to the validation cruise in which the PRIMI system has been validated.

5.1 Validation

The developed OS detection algorithm has been tested and validated against *in situ* oil spill observations. For this purpose, a subset of 25 oil spill events taken from the validation OS database (see paragraph 2.3) has been selected and used for the validation. This validation dataset does not include the cases used to develop the methodology. The assessment of the algorithm was made by comparing the reference oil spills of the validation database with those automatically detected by our OS detection algorithm. The validation OS database contains oil spills observed by MODIS AQUA, MODIS TERRA and MERIS sensors. This database can be considered representative of the Mediterranean oil slicks, being characterized by a large variety of oil slicks (large, small, with different shape and thickness, etc..) and different illumination and satellite viewing geometry in the oil spill area (high and low glint case).

5.1.1 Validation oil spill database

The validation oil spill database, containing in situ observed oil spill events, is illustrated in table 5.1. It is to be noted that the number of observations in table 5.1 refers to the number of optical images relative to each OS event. Each observation (image) can contain one or more oil spill regions and the total number of OS regions is reported in the third column.

Location/OS Source	Number of Observations (images)	Total Number of digitized oil spill regions
Lebanon Case (2006)	11	77
Algeria (2008)	1	1
ROSES (2007)	3	3
Italian Ministry (2001-2008)	5	10
PRIMI Cruise (2009)	5	10
TOTAL	25 images	101 oil spill regions

Table 5.1 Validation oil spill database.

In correspondence of each event of the database, we collected the corresponding MODIS (AQUA and TERRA) L0 and MERIS full resolution (300 m) L1B passes, in which the area of hydrocarbon discharge was not covered by clouds and visible in the satellite imagery. This has constituted our OS dataset of certified oil spill cases. This includes a temporal suite of 11 OS cases relative to the Lebanon disaster caused by air raids on coastal power plants (July-August 2006), 5 open sea OS cases in the Italian seas reported by the Italian Ministry of the Environment, for which remediation units were sent on the spot to perform cleanup duties (2001-2008), an OS off the Algerian coast (August 6-10, 2008) certified by REMPEC, 3 OS cases reported by ROSES (Real Time Ocean Services for Environment and Security) and five OS's visited by CNR's R/V Urania during the PRIMI cruise (2009), for a total number of 25 images and 101 oil spill signatures (regions).

As done for the training dataset, each oil spill signature presents in MODIS and MERIS data was manually digitized via ENVI's Region of Interest (ROI) tool and saved to oil spill position text files. ROIs were used as reference oil spill regions.

5.1.2 Comparison analysis

The method has been tested by applying the OS detection algorithm to MODIS AQUA, MODIS TERRA and MERIS imagery relative to the oil spill cases reported in table 5.1. The validation was performed in two steps:

1) Computing a success percentage by comparing reference oil spills with those automatically detected in order to verify that our system is able to detect the event in the correct location;

2) Computing a success percentage by comparing the areas of the detected oil spills with the areas of the reference oil spills, by means of area ratios.

I° Validation Procedure: "Yes or No" comparison between ROIs and identified regions

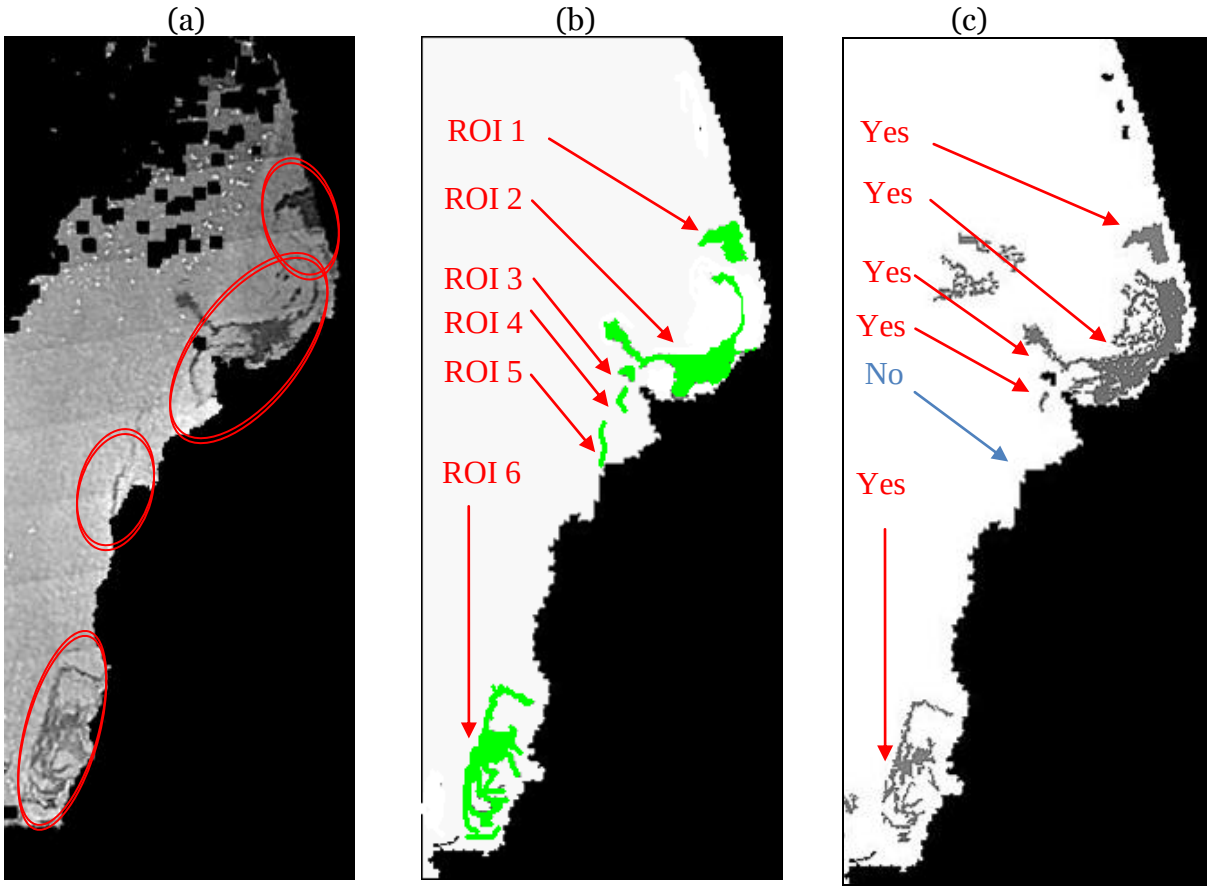

Figure 5.1 (a) $\rho_{\varepsilon}(859)$ from MODIS AQUA (August 2 2006) relative to the oil spill (in red ellipses) of the Lebanon coast **(b)** ROI matrix: green regions are oil spills signatures manually digitized. **(c)** Oil spill candidate matrix: land in black, sea in white and oil spill regions in grey.

The comparison procedure, step 1, simply counts how many digitized oil spill regions (ROIs) are detected in the output image by a "yes or no" assignment. Figure 5.1 (a) shows one of the 11 OS cases relative to the Lebanon oil spill disaster, represented by $\rho_\varepsilon(859)$ MODIS band, while figure 5.1 (b) shows the digitalization in which are present 6 oil spills depicted as green regions. The result of the application of the detection algorithm is showed in figure 5.1 (c) in which are present 5 oil spill regions. In this case, the algorithm was able to identify 5 out of 6 regions, giving a success percentage of 83%. Only the fifth oil spill (ROI 5) was missed by the automatic detection, probably detected as water region. It is to be noted that look-alike features, visible in of figure 5.1 c offshore Beirut, have an associated score less than 30% much smaller than the other regions (greater than 60%). Therefore, the system already provides an indication that such spills can be false alarms. This "yes or no" comparison procedure was applied to all OS cases of the validation dataset. Table 5.2 reports the percentage values obtained as average for each OS source.

Location/OS Source	**Number of Observations (images)**	**Total Number of digitized oil spill regions**	**Yes/NO**
Lebanon Case (2006)	11	77	95%
Algeria (2008)	1	1	100%
ROSES (2007)	3	3	75%
Italian Ministry (2001-2008)	5	10	70%
PRIMI Cruise (2009)	5	10	50%
TOTAL	25	101	78%

Table 5.2 "yes or no" comparison procedure applied to the validation OS dataset.

In most of cases, the auto detection was able to correctly identify the reference oil spill regions, even if the system is not able to detect very small spills as happens for some PRIMI cruise cases which will be discussed in the next section. The missing of small spills is due to threshold area values, defined in section 3.2.2, which discard regions with an area less than 1 Km^2 and is linked with the spatial resolution capability of the MODIS and MERIS data.

As regards step 2, we have performed a more detailed comparison procedure. Given the ROI matrix (e.g. figure 5.2 a) and the output OS matrix for each test case of the validation dataset, we computed the number of common pixels between the two matrixes, through an "and to and" operation. An example of this procedure is shown in figure 5.2, for the same OS case of figure 5.1. Red pixels of figure 5.2 (c) represent the percentage of

success in terms of contouring and area comparison. Figure 5.2 (c) shows that oil pills areas detected by the algorithm are in general smaller than those manually digitalized. This is not surprising since the manual digitalization of an expert operator can often include water pixels at border of oil spill contour and can connect disjoint regions separated by few pixels. This implies an overestimation of the actual area covered by the oil and a subsequent decreasing of the success percentage. The success percentage of figure 5.2 c results to be 70%. The decreasing with respect to the 83%, deriving from the "yes or no" computation, is due to both manual error and missing ROIs in the automatic detection, such as the ROI number 5 not present in the output image. Table 5.2 summarizes results of the application of the procedure described above to the entire validation dataset. The overall percentage of correct identification of the area covered by the 101 oil spills analyzed is 65%, which is obviously lower than the percentage derived analyzing only the number of identified regions. Since this method compares the overall area classified as oil by the automatic system with the ROI area for each event, the limited decrease of percentage resulting for table 5.2 with respect to 5.1 clearly indicates that the system detected the presence of oil region despite the ambiguity of the area in which oil and water are not really separated.

II° Validation Procedure: Area ratio comparison between ROIs and identified regions

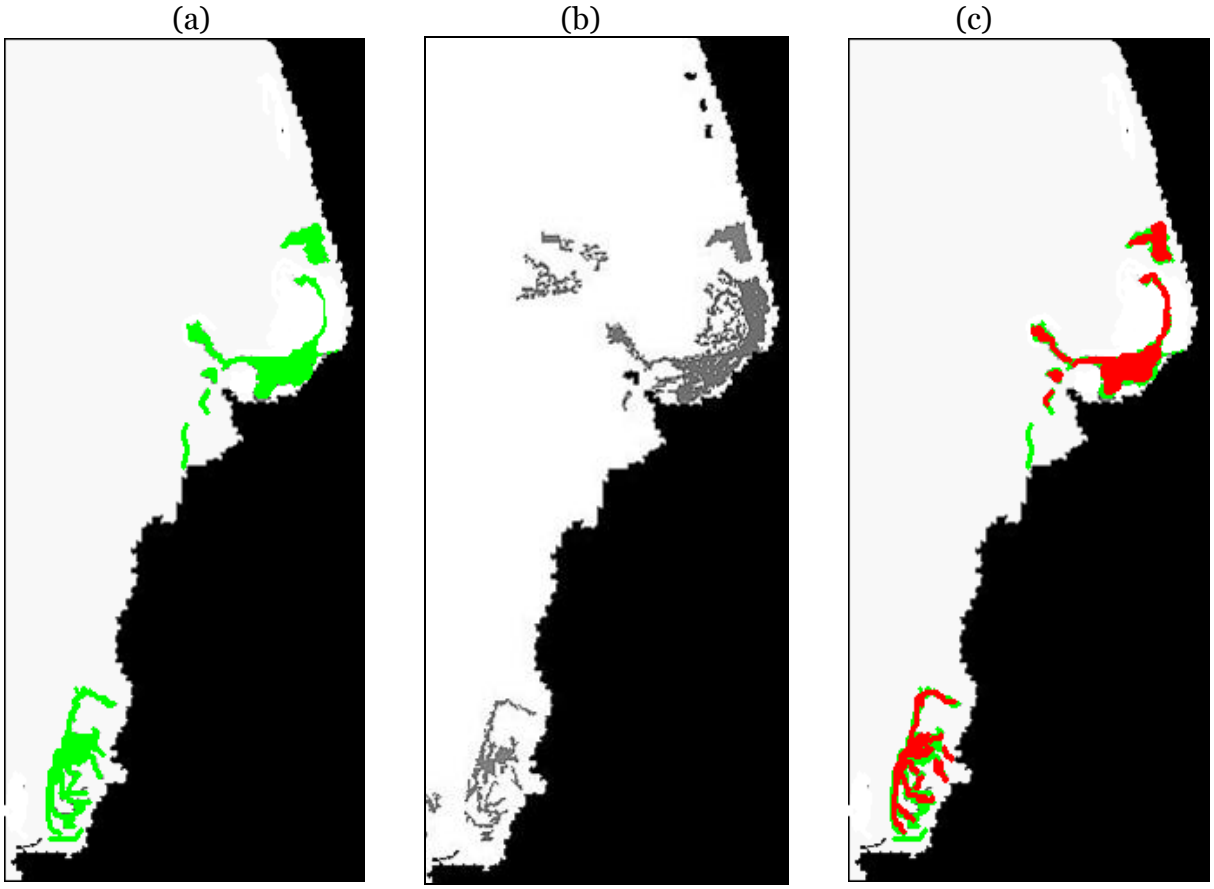

Figure 5.2 (a) ROI matrix: green regions are oil spills signatures manually digitized. **(b)** Oil spill candidate matrix: land in black, sea in white and oil spill regions in grey. **(c)** Comparison result: red pixels are common pixels belonging to both digitized pixels (in green, fig. a) and detected pixels (in grey, fig c).

Location/OS Source	Number of Observations (images)	(OS Area/ROI Area) %
Lebanon Case (2006)	11	85 %
Algeria (2008)	1	77 %
ROSES (2007)	3	50 %
Italian Ministry (2001-2008)	5	65%
PRIMI Cruise (2009)	5	40%
TOTAL	25	65%

Table 5.2 Area ratio comparison procedure applied to the validation OS dataset.

5.2 Experimental results

Here we report the results relative to the analysis of two OS cases taken from the validation OS database, the first relative to the Algeria oil spill event and the last relative to the PRIMI cruise.

5.2.1 The Algeria oil spill case

The Algeria OS event, one of the 25 OS events used for the validation of our OS detection algorithm, was certified in situ north of the Algerian coast by REMPEC in 2008.

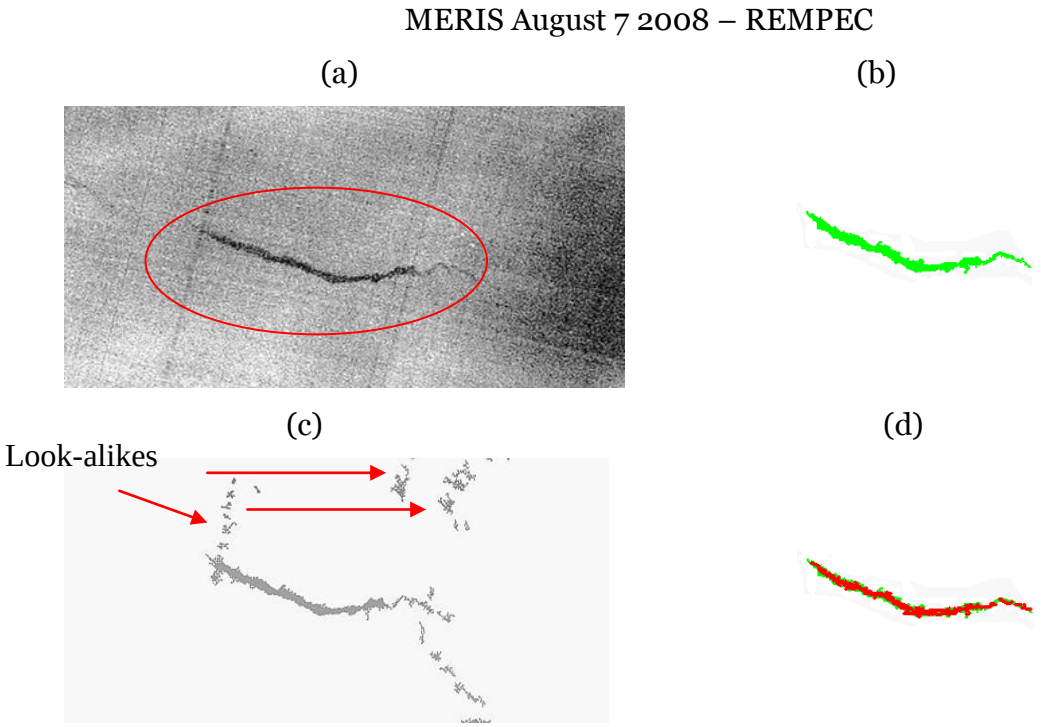

Figure 5.3 (a) $\rho_{\varepsilon}(865)$ from MERIS (August 7 2008) relative to the oil spill (in red ellipse) north of the Algerian coast. **(b)** ROI matrix: green region is the oil spill signature manually digitized. **(c)** Oil spill candidate matrix: land in black, sea in white and oil spill regions in grey. **(d)** Comparison result: red pixels are common pixels belonging to both digitized pixels (in green, fig. b) and detected pixels (in grey, fig c).

Figure 5.3 shows the representative steps of the OS detection methodology. The input image, containing the oil spill (in red ellipse of fig. 5.3 a) to be detected, is the $\rho_{\varepsilon}(865)$ reflectance band relative to MERIS sensor. Manually digitalization of the oil spill signature

is shown in fig. 5.3 b, depicted by the green region. Applying the OS detection algorithm to the input $\rho_{\varepsilon}(865)$ band, we obtain the result shown in fig. 5.3 (c), where grey regions represent all candidate oil spills and are also clearly visible the presence of look-alikes. Finally, figure 5.3 (d) shows the comparison result in terms of area ratio. Red pixels of fig. 5.3 (d) represent the detected oil spill area that corresponds exactly to the area of the reference oil spill region (green region of fig. 5.3 d). The area ratio percentage is 77%. As regards look-alike features, figure 5.4 shows that scores relative to look-alikes are much smaller than the score assigned to the slick structure that represents the actual spill.

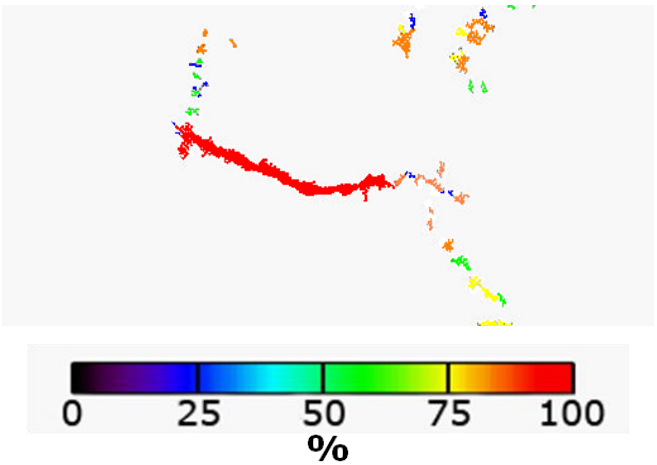

Figure 5.4 OS matrix, relative to the Algeria spill, with associated score.

Finally, figure 5.5 shows the same Algeria oil spill event detected by ASAR sensor, onboard ENVISAT satellite. The radar image is of August 8 2008, the day after MERIS observation and it is evident the displacement of the oil spill.

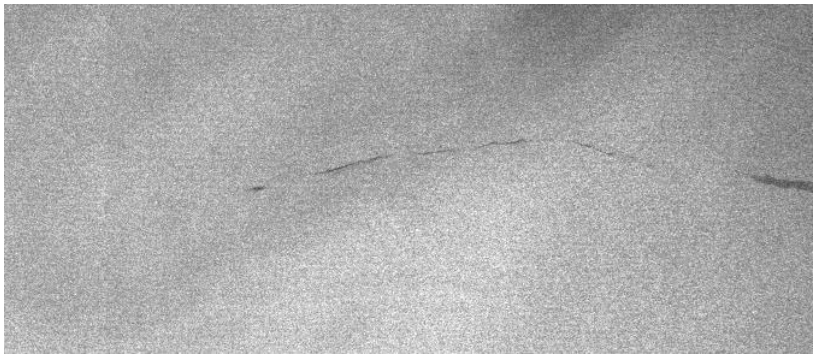

Figure 5.5 ASAR detail (August 8 2008) of the Algeria OS event.

5.2.2 PRIMI cruise validation

The PRIMI system was tested during a cruise (Aug. 6 – Sep. 7, 2009) organized by CNR-ISAC onboard CNR R/V Urania and to which both PRIMI and non-PRIMI institutions have participated. The cruise took place in the seas around Sicily (Tyrrhenian, Ionian Seas and Sicily Channel; Fig. 5.6), an area with high illegal hydrocarbon discharge frequency, as inferred from historical and PRIMI monitoring data. The main cruise objective was to visit oil slicks detected by the PRIMI SAR and Optical Observation Modules and whose displacement was predicted by the PRIMI Forecast Module, thus testing the system. The visited OS's are shown in figure 5.6 by red dots. A set of SAR ENVISAT ASAR, ERS-2 and COSMO-SkyMed acquisitions was planned before the cruise, in order to conceive the cruise track so as to maximize the probability of OS in situ validation and hydrological coverage. OS detection SAR reports were received on board, from the PRIMI operational site at ASI Matera (Italy), within two hours of acquisition (daytime images) or the following morning (nighttime images).

We exemplify the OS in situ location effort by describing the activities in correspondence of a slick (figure 5.7 a, b) detected in two successive ENVISAT ASAR images (Aug. 26 21:05:07 UTC and Aug. 27 10:15:10 UTC), in which 3 and 10 slicks were detected by the PRIMI system, respectively. The same OS was also detected in the MODIS TERRA imagery (Aug. 27 2009 10:00 UTC, figure 5.8 a) and correctly extracted by the OS detection algorithm (figure 5.8 b) , though partly under cloud. Upon report receipt, OS positions were predicted in real time by the Forecast Module dispersion-transformation model (figure 5.9 a) and R/V Urania steamed towards the OS location on Aug. 27 morning, adjusting its course to the latest OS predicted positions. The OS was successfully located within a few nautical miles of the predicted position (figure 5.9 a), photographed (figure 5.9 b). Polluted water samples were collected and 2.0 and 2.3 g kg-1 of hydrocarbons were found in the samples. Also, a lagrangian drifter was deployed within the OS and the trajectory agreed with the GPS fixes of the slick being followed by the ship, in describing a northwestward drift, though the slick drift was seen to be more of a straight line, probably due to greater influence of the wind on the oil film (figure 5.9 a).

8 OS's were visited (figure 5.6) out of a total of about 30 slicks detected by SAR in the area, 5 of which confirmed in MODIS or MERIS imagery when the sky was clear. The 50% success percentage (see table 5.2) of our auto detection algorithm can be justified by a detailed analysis of MODIS and MERIS signal against in situ inspection. In situ measurements revealed that in this cases the OS was made of a thin hydrocarbon film, detected visually by iridescence and absence of capillary waves and instrumentally by roughness attenuation in the onboard RADAR signal and Raman signal depression in the

LIDAR data. The combination of small dimension of the spill, its thin thickness and the mixture of oil-spill and clear water results in a limited OS signal in the TOP radiances which fails the automatic detection.

The three most polluted oil spills, i.e. those which contained thick, dark oil patches and floating solid hydrocarbon particles were chosen for drifter release. Patchiness was always found, both in lightly and heavily polluted sites. These heavy slicks were correctly detected by our method, as in the case shown in figure 5.8.

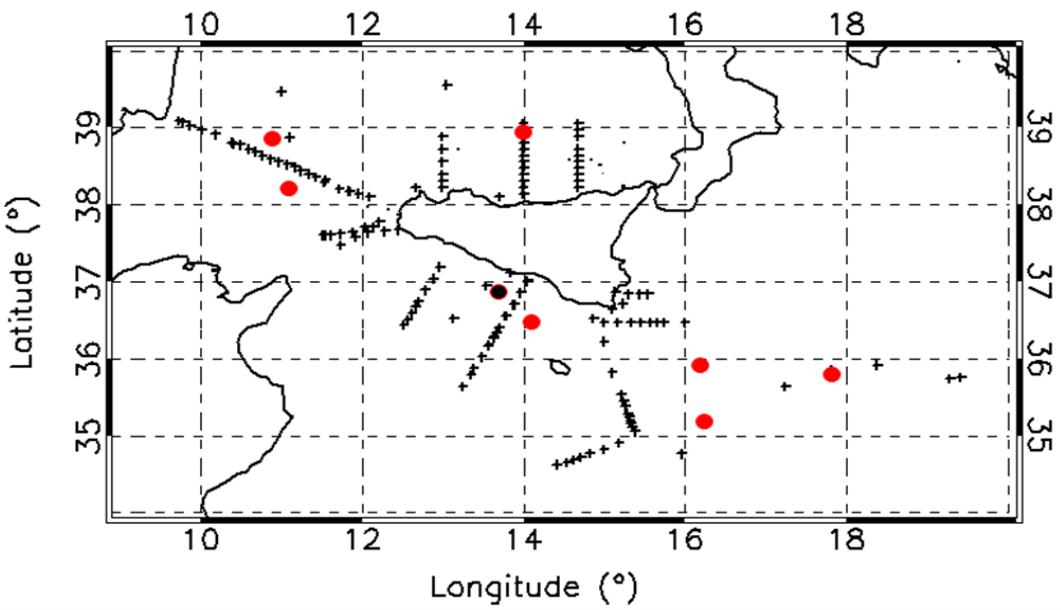

Figure 5.6 PRIMI cruise (Aug. 6 – Sep. 7 2009, R/V Urania) hydrological stations (black crosses) and visited OS's (red dots). Black dot: OS described in text.

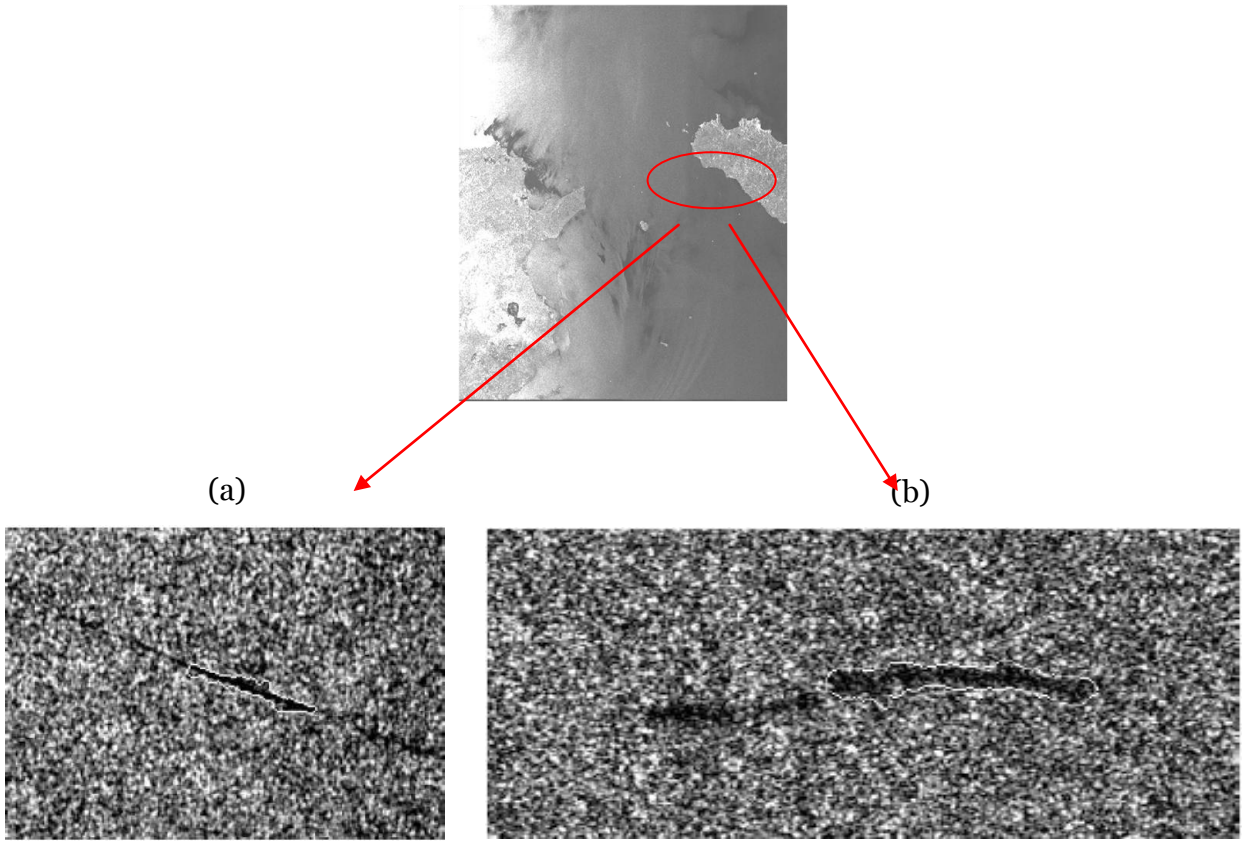

Figure 5.7 PRIMI cruise, OS of Aug. 26-27, 2009, Sicily Channel. **(a)** OS in ENVISAT ASAR image, Aug. 26 2009 21:05 UTC, extract from PRIMI report; **(b)** same OS in ENVISAT ASAR image, Aug. 27 2009 09:20 UTC, extract from PRIMI report.

PRIMI cruise, OS of Aug. 26-27, 2009, Sicily Channel
MODIS TERRA true color image (Aug. 27), $\rho_\varepsilon(859)$ detail and detection result

(a)

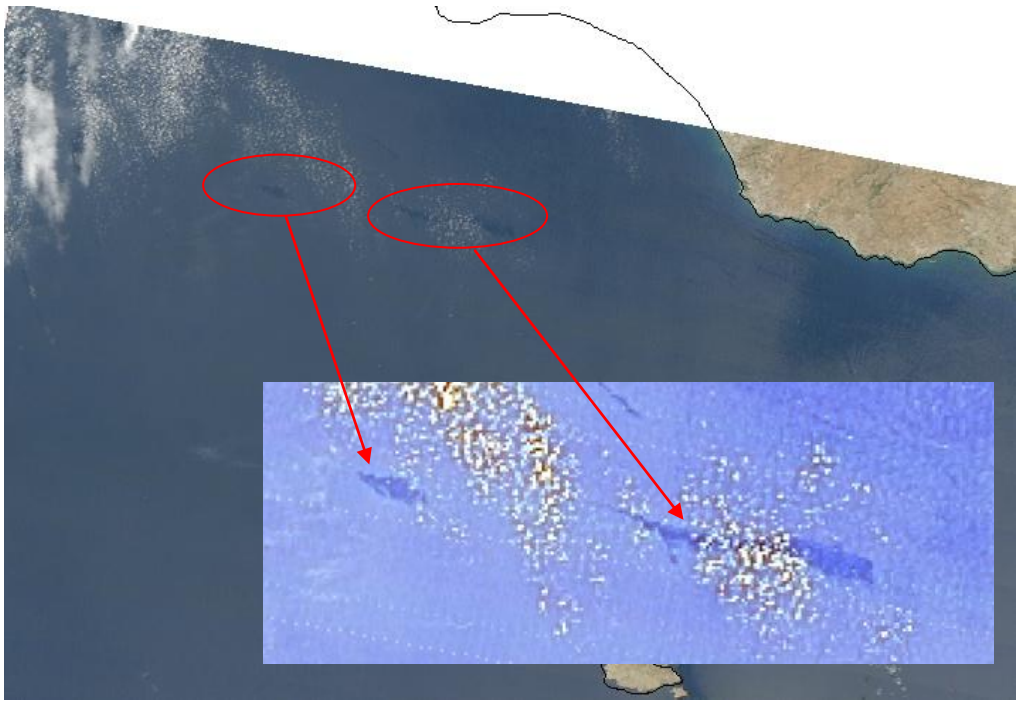

(b)

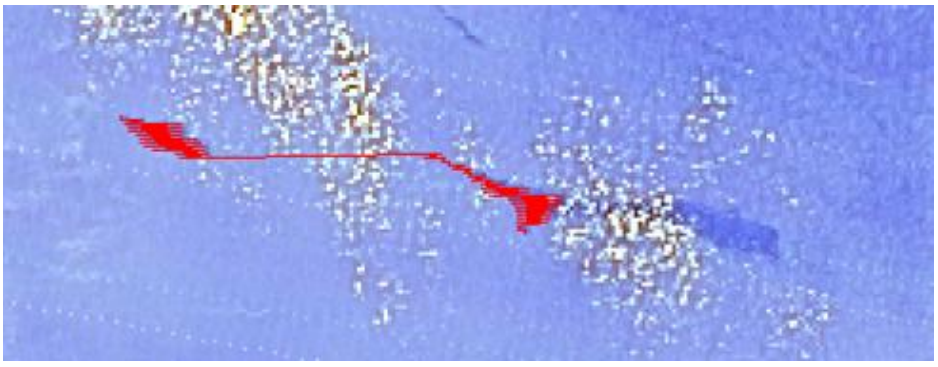

Figure 5.8 PRIMI cruise, OS of Aug. 26-27, 2009, Sicily Channel. **(a)** OS (in red ellipses, partly under cloud) in MODIS TERRA true color image and $\rho_\varepsilon(859)$ detail, Aug. 27 2009 10:00 UTC; **(b)** OS detection result.

PRIMI cruise, OS of Aug. 26-27, 2009, Sicily Channel

Forecasting

(a)

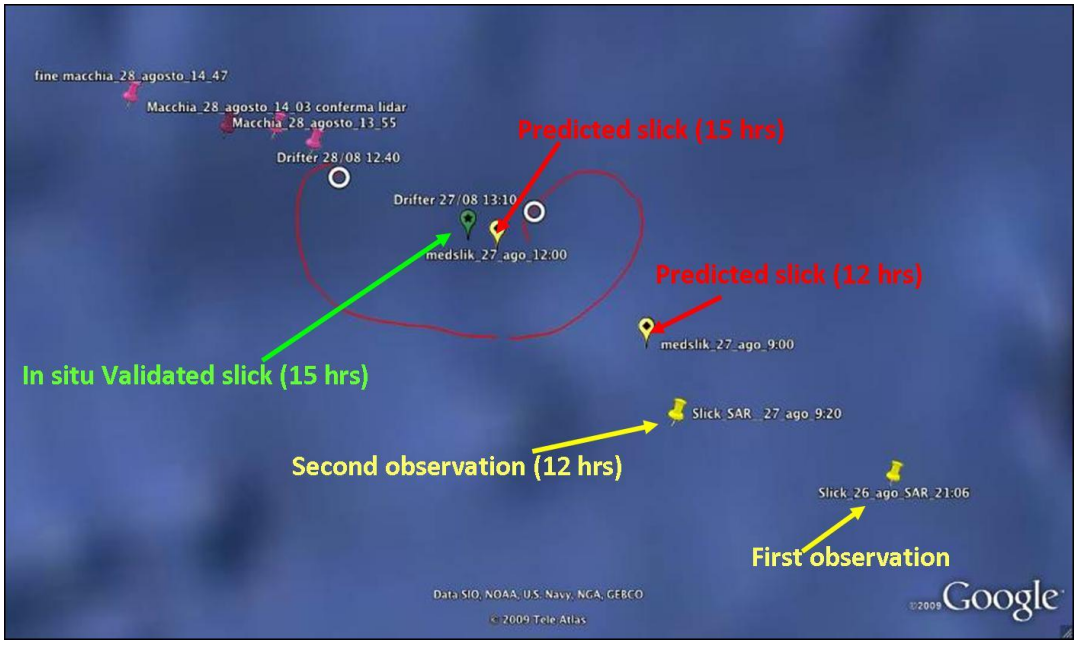

(b)

Figure 5.9 PRIMI cruise, OS of Aug. 26-27, 2009, Sicily Channel. **(a)** Slick SAR observation locations (in yellow), prediction positions (in red) and in situ location (green), drifter trajectory (red curve), final slick positions of Aug. 28 (tags at upper left). **(b)** One of the heavier oil slicks within OS, as photographed from the ship.

Summary and Conclusions

Satellite remote sensing has proved to be an effective support to naval and aerial surveillance in early detection and continuous monitoring of marine oil pollution caused by illegal ship discharges. At present, SAR sensors are commonly used by monitoring systems due to their well demonstrated capability in oil spill (OS) detection. However, long revisit times and low spatial coverage, due to SAR high spatial resolution and consequent narrow swaths, typically of order 100-400 km, call for a multi-platform SAR slick detection effort as well as wider swaths platforms, i.e. optical sensor satellites (with swath greater than 1000 km). The new optical satellite sensors generation, i.e. MODIS and MERIS spectroradiometers, can now overcome the SAR reduced coverage and long revisit time of the monitoring areas, given their higher spatial resolution (250-300 m) with respect to older sensors (>1 km), which consents the identification of smaller spills deriving from illicit discharge at sea. The optical image processing and analysis for oil spill detection is strongly innovative since algorithms on oil slick detection for MERIS and MODIS data are lacking. In this context, we have developed a new methodology for optical oil spill detection, which makes use of MODIS L1B high and medium resolution (250 and 500 m) and MERIS L1B full resolution (300 m) satellite top of atmosphere (TOA) reflectance imagery, for the first time in a highly automated way.

The objective of this thesis work was to investigate and understand how oil spills at sea can be remotely sensed by optical sensors in order to develop an automatic oil spill detection methodology. The passage from image inspection, relying on human operator skills, to more objective and automated detection procedures has been explored in this thesis by analyzing and combining the spectral signatures of the various available MODIS and MERIS products. The first task was to:

1. Build a database of certified oil spill events (OS database);
2. Collect for each certified OS event of the database the corresponding MODIS and MERIS passages;

This was necessary for the development and validation of our OS detection algorithm.
The most crucial steps in the oil spill detection methodology involved the development of the following procedures:

3. Removal of oceanic and atmospheric natural variability from MODIS and MERIS TOA reflectance images in order to enhance oil-water contrast;

4. Isolation and contouring of all spectral signatures, through appropriate threshold and clustering processing of the image;
5. Extraction of key parameters for each candidate signature and elimination of those features which look like spills (look-alikes), based on threshold values of these parameters;
6. Classification of oil spill candidate regions by means of a score.

The oil spill database

The development of our oil spill detection methodology for MODIS and MERIS imagery required the availability of a set of certified oil spill events. We built a database of *in situ* oil spill observations, collecting all the information on oil spill disasters occurred in the Mediterranean Sea and all the oil spills reported by International and Italian National Authorities responsible for the oil spill illegal monitoring. In correspondence of each of these events, we collected the corresponding MODIS (AQUA and TERRA) L0 and MERIS full resolution (300 m) L1B passes, in which the area of hydrocarbon discharge was not covered by clouds and visible in the satellite imagery. This has constituted our OS dataset of certified oil spill cases. This includes a temporal suite of the Lebanon coastal spills, caused by air raids on coastal power plants (July-August 2006), some cases in the Italian seas reported by the Italian Ministry of the Environment, for which remediation units were sent on the spot to perform cleanup duties (2002-2008), an OS off the Algerian coast (August 6-10, 2008) certified by REMPEC and five OS's visited by CNR's R/V Urania during the PRIMI cruise, for a total number of 40 images. A subset of 15 images present in the database were selected to develop the methodology, while the remaining 25 cases were used to validate the algorithm.

Oil spill regions were manually digitized in the images via ENVI's Region of Interest (ROI) tool and saved to oil spill position text files, which were used in the development and testing of spectral and shape criteria and building score tables for distinction between oil spills and look-alike features as detected by the image clustering algorithm. Finally, each OS scene in the images has been classified as high or low glint, depending on whether the slick was in mirror-like reflection (high sun glint) condition or not. Sun glint condition was determined by finding a threshold of the glint angle.

MODIS L0 and MERIS L1B files were downloaded from the NASA and ESA websites and then processed via standard procedures to obtain the following geophysical parameters:

- TOA reflectance bands, $\rho_t(\lambda)$[2];
- Rayleigh radiance bands, $L_r(\lambda)$;
- Calibrated TOA radiance bands, $L_t(\lambda)$;
- Water-leaving radiance bands, $L_w(\lambda)$;

plus additional products used to perform internal processing steps.

The oil spill detection methodology

The basic idea for the oil spill detection was to enhance oil spill contrast with respect to clean water and to flatten the variability as much as possible in the MODIS L1B and MERIS L1B TOA reflectance ρ_t images, in order to improve both the visual inspection and the automatic classification procedure. Indeed, oil slicks in standard TOA reflectance images are often confused visually (and numerically) with analogous look-like oceanographic features such as chlorophyll filaments, etc. Moreover, atmospheric effects such as reflectance modulation due to aerosol patches can introduce further noise, thus further masking the slicks.

The new automatic OS detection algorithm consists of three main parts, i.e. image flattening, image clustering and OS candidate selection. These techniques, described in detail in chapters III and IV, can be resumed as follows:

I. Striping correction (MODIS only) and production of geophysical data:
   - Destriping (only for MODIS imagery);
   - MODIS and MERIS data processing (L1B to L2) to produce selected geophysical products (table 2.4);

II. L2 TOA reflectance bands ($\rho_t(\lambda)$) and the selected geophysical products are the input for the image flattening procedure:
   - Cloud Masking;
   - Elimination of Rayleigh and water-leaving reflectance;
   - Elimination of aerosol contribution;

III. The elimination of natural oceanic and atmospheric natural variability provides flattened reflectance products ($\rho_\varepsilon(\lambda)$), that become the new input for the clustering and OS classification steps:
   - Segmentation and clustering;

[2] λ = (469, 555, 645, 859, 1240, 1640, 2139 nm) for MODIS imagery;
λ = (443, 560, 665, 681, 865) for MERIS imagery.

- OS selection among cluster regions via geometric, spectral and statistical criteria;
- Score assignment to OS candidates.

Striping correction and cloud masking

The destriping procedure was developed to eliminate the striping effect of MODIS imagery. These stripes are due to the fact that two consecutive data sweeps, perpendicular to the satellite's flight direction, are acquired by the two faces of a rotating mirror, which reflect the light from the scene to the onboard sensors. At present, a simple version of destriping was developed and applied to L1A data. It consists of determining the slope and bias of the regression line best fitting each ramp and "rectifying" the ramp by subtracting the regression line from the signal. Results showed that developed algorithm is able to eliminate elongated look-alike features at the border between two major stripes (figure 3.1) and has proven satisfactory to improve the oil spill classification since elongated features corresponding to the stripes are no more classified as possible slicks. However, the application of our destriping algorithm in other contexts (e.g. elimination of stripes in MODIS chlorophyll imagery) will require further development.

L2 images are then declouded via an ad hoc procedure which relies on the SST quality flag product (quality indicator for Sea Surface Temperature computation) and a specific procedure based on the high positive contrast for the cloud pixels in the high (250 or 300 m) resolution bands. We decided to use the SST quality flag instead of the standard cloud flag product (L2 Flag, table 2.3) since the analysis of our training dataset reveals that the standard cloud flag produced by SeaDas software includes also oil spill pixels. The use of the SST quality flag product overcome the problem of OS classification as clouds, that often occurs in high glint condition. Using the SST quality flag, all pixels for which even one quality flag indicates bad SST are flagged as bad data. Unfortunately, not all cloudy pixels can be removed in this way. Therefore, a custom procedure has been developed: the reflectance standard deviation of each pixel and its 3x3 pixel bounding box is computed and saved in a new matrix. Since cloudy pixels have high reflectance with respect to surrounding water, the standard deviation of a cloudy pixel and its bounding box will be high. Thus, cloudy pixels are further removed from the original image via thresholding on this standard deviation.

Image flattening

The image flattening procedure "strips" each $\rho_t(\lambda)$ image from the reflectance deriving from atmospheric and oceanic natural variability, thus leaving a smoother or flat

"residual ocean" field in which oil slicks stand out better, thus being less liable to be confused with or masked by non-slick features. This is done by:

- Subtracting Rayleigh reflectance from $\rho_t(\lambda)$ (all selected wavelengths);
- Subtracting Normalized Water-Leaving reflectance from $\rho_t(\lambda)$ ocean-sensitive wavelengths (e.g. 469 and 555 nm for MODIS);
- Subtraction of an aerosol reflectance map, created using red band, to which aerosol is sensitive, from each $\rho_t(\lambda)$.

The results of this procedure are what we call $\rho_\varepsilon(\lambda)$ or "flattened" TOA reflectance bands. The band yielding best OS visibility, i.e. in enhancing and maintaining the oil spill after image correction, resulted to be the 859 nm for MODIS and the corresponding 865 nm for MERIS. This led us to choose ρ_ε (859/865) as the "optimal" band for the clustering procedure following image correction.

Image clustering

The clustering procedure groups image pixels with similar reflectance into a set of clusters (regions) with common mode reflectance values. The purpose is to be able to segment the oil spill eventually presents in the image. We have developed a technique based on *mean shift algorithm*, a nonparametric clustering technique which does not require prior knowledge on cluster number and does not constrain cluster shape. Image pixels are regarded as samples from an unknown probability density function, and a mean shift vector is defined, at a given pixel, as parallel to the local maximum reflectance gradient. The length of the mean shift vector is equivalent to a search radius determined as a fraction of the standard deviation of reflectance distribution in the image. The pixel reflectance is then ideally substituted with the reflectance of the pixel at the vector's point. The operation is repeated until a point is found where the reflectance gradient is zero and the shift stops. The final "arrival" reflectance value, the cluster's mode reflectance, is assigned to each pixel converging there in the shift process. The ensemble of pixels with the same mode constitute the cluster itself and each cluster is, in Euclidean space, in general formed by a set of disjointed regions. Finally, modes which are closer than a threshold value (to be determined on the basis of reflectance variability in the image) are pruned, as done in generic feature space analysis, and pruned mode pixels are assigned to the most populated and closest mode cluster. Cluster regions are then pruned by means of a first set of geometric and spectral parameters computed for each region and for water surrounding the region itself.

Oil spill classification

We defined a suitable set of *features parameters* in order to characterize oil spills and determine criteria to distinguish between oil slicks and look-alikes. The features parameters are a mix of standard region descriptors, such as the area, perimeter and reflectance mean values, and features tailored to oil spill detection (see table 3.1). These have been devised and tested on 15 certified oil spills cases constituting the training OS database (paragraph 2.2.4). For each region issuing from the above clustering process the set of features is computed (features extraction) in order to classify the slick as either oil or look-alike. After pruning, most of obviously non-slick features (e.g. large regions) and look-alikes (e.g. slick-like regions with wrong region-water contrast) are eliminated. The result of this region pruning process leaves several regions that are clearly not oil slicks, that we defined as "OS candidates". The physical reason for the absence of clear-cut separation criteria mainly lies in the fact that oil spills are patchy, and this was confirmed during the PRIMI validation cruise. Oil concentration on the surface, even within a small oil slick detected by a high resolution SAR satellite image, may vary from virtual absence of hydrocarbon to a thin film which sufficiently suppresses capillary waves, to heavily polluted brown or black waters with floating hydrocarbon solid particles of variable dimensions. This patchiness has a spatial variability scale inferior to the MODIS, MERIS or even SAR pixel size. Consequently, reflectance from a pixel within an OS is often an average reflectance resulting from a mix of the above pollution situations. Moreover, "clean" water pixels surrounding an OS may actually be affected by slight pollution. Finally, the OS digitizing, the flattening and declouding processes are not perfect and residuals of clouds or natural surface variability may still be present, which is the fundamental reason for which look-alikes exist, e.g. as darker patches in low glint scenes.

Score computation

These facts and the results of the more consolidated research in SAR OS detection induced us to re-analyze the OS candidate regions issuing from the above pruning process with a second set of parameters and to define scores for each parameter applied to each OS candidate. The new set of parameters is defined in paragraph 4.1.3. Most of these parameters involve reflectance histogram integrals in order to overcome ambiguities introduced by slick patchiness, which may bias contrast conceived as region/water mean reflectance ratio. These "integral" parameters enable us to tell whether a region is statistically darker or lighter than surrounding water. Each parameter was estimated for all regions and surrounding water bounding boxes of our training OS image database. Histograms of each parameter distribution were computed, both for known OS's and look-

alikes. The training OS database (15 OS events constituted by several slicks) together with the look-alikes deriving from the application of the algorithm was used to compute score look-up tables (LUT), for each of the above parameters. Given a parameter distribution (e.g. figure 4.8 a), histograms (H) of each parameter (P) distribution were computed, both for known OS's ($H_{OS}(P)$) and known look-alikes ($H_{LA}(P)$) and a 0 to 1 score for each parameter value was defined as (figure 4.8 b):

$$S(P) = H_{OS}(P)/(H_{OS}(P)+ H_{LA}(P)) .$$

That is, the score is higher if a high number of OS's have a given parameter value compared to the number of look-alikes with the same value. This constitutes the score LUT. When a new oil spill candidate is detected its P values are computed and found in LUT. Then a cumulative score issued by adding single parameter scores and normalizing to 1. Therefore, a score is assigned to each OS candidate remaining after pruning.

Validation and conclusions

The method has been tested and validated using an independent dataset of 25 oil spill events (see table 5.1) in which several slicks were present in MODIS AQUA, MODIS TERRA and MERIS sensors and revealed its capability to detect also small slicks coming from illegal discharges. The success of the method was quantified by comparing the automated classified slicks against 101 certified oil spills taken from the dataset, visible in the imagery and digitalized by an expert operator. The result of this validation show that the method was able to detect the 78% of the certified oil spill cases. Obviously, optical sensors are not able to detect spills when the area is cover by clouds and the comparison with respect to SAR detection indicated the inability of detection when the dimension of the spills is less than 1 Km^2, due to the MODIS and MERIS medium spatial resolution.

The method developed in this thesis has been transferred in the PRIMI system and constitutes the optical observation module of the PRIMI project. This method has been engineered and tested operationally for 6 months allowing to increase the monitoring of the Italian Seas complementing SAR images and 210 spills were reported.

Research has been encouraged by the positive results of in the situ validation cruise, but calls for further development. A crucial point is to increase the certified OS cases in the OS database, in order to cover as many illumination-view situations, type and thickness of the spill as possible in order to improve the capability of the pruning parameters to eliminate look-alikes. Next, research in devising new pruning and score parameters is still ongoing, in order to obtain more efficient pruning parameters and score tables with which

to more certainly discriminate oil spills from look-alikes. Indeed, the goal is to have a threshold score to perform a second pruning and fully automatized system. Finally, the proposed algorithm, being independent from the specific satellite platform, permits to exported it on a different satellites and sensors (e.g. hyperspectral) and to be updated for the next generation of optical satellites (e.g. Sentinel-3, VIISR).

Acknowledgments

We thank Drs. M. de Dominicis, G. Coppini and N. Pinardi (INGV) for providing oil slick location and prediction positions; Dr. Mario Sprovieri (CNR-IAMC Naples) for hydrocarbon chemical analysis; all the PRIMI cruise participants and the R/V Urania crew. The PRIMI project is funded by the Italian Space Agency (ASI).

Appendix A

Principles Of Remote Sensing

The principle of ocean remote sensing is the measure of e.m. radiation reflected and/or emitted from the observed sea surface. There are just three possible sources of the energy that can received by a remote sensing instrument. It may have originated from the Sun and then been reflected, it may have been emitted by the surface being observed, or it may have been produced on the satellite by the sensor and then reflected from the sea. Remote sensing systems which measure radiation that is naturally produced or emitted are called *passive sensors*; those that measure their own energy are called *active sensors*. Figure A.1 shows schematically what is involved in obtaining ocean information using a sensor that is typically hundreds or thousands of kilometers from the sea surface.

The e.m. radiation that have interacted with or being emitted from the sea surface carries the information from the sea to the sensor. Information transfer is limited because the radiation must pass through the Earth's atmosphere. The atmosphere is opaque for many parts of the e.m. spectrum, rendering them useless for remote sensing. In those part of the spectrum where the atmosphere is transparent, the radiation passing through may still be altered in various ways, potentially corrupting the ocean information.

The ocean remote sensing is dictated by the nature of the information about the sea that is possible to communicate by e.m. radiation. In practice, there are just four primary quantities that can be observed from space: *colour*, *temperature*, *roughness* and *height* of the sea. Only properties at the sea surface can be detected. For colour it is the upper few metres that are observed, while the other three properties are defined at the very surface itself. Many phenomena in the upper ocean have sufficient influence on one or more of the primary measurable quantities to be detectable in remotely sensed data and images. We refer to this as the phenomenon having a *surface signature* or *spectral signature*. The spectral signatures of organic and inorganic obsorbers and scatters in the water, such as phytoplankton, dissolved organic material and suspended particulates, are directly related to the colour of the sea, as measured from the satellite. Internal waves, a dynamical phenomenon centred tens of metres below the sea surface, can sometimes be revealed in the images of SAR, because of their surface roughness signature. Many ocean features have

their own surface and spectral signatures and can be studied by remote sensing from space. Obviously we need to understand the processes that cause them to have a spectral or surface signature in one of the primary detectable variables, if quantitative information about them is to be recovered. For now it is important to note that most of the phenomena that appear in satellite images are revealed indirectly, that is through the development of specific algorithms.

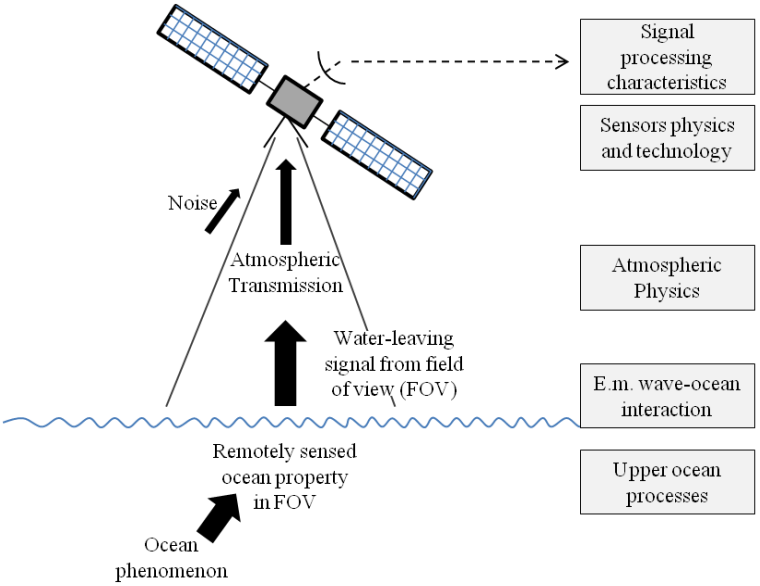

Figure A.1 Schematic flow chart for the ocean remote sensing. The boxes on the right indicate the field of knowledge required to understand the processes controlling the information flow.

Therefore all Earth-viewing sensors on a satellite measure one or more properties of the incoming e.m. radiation and transmit these measurements to the ground. The potential of oceanographic application of the data is dependent on the detailed specification of what aspect of the radiation is detected. For example, it could be the radiant energy of solar reflection from the sea in a narrow spectral waveband, the time of arrival of a radar pulse reflected from the sea, or the power intercepted by a microwave antenna pointing at the sea. Once the digital data have been received at the ground station, the task remains to recover useful oceanographic information. This requires an inversion of the flow chart outlined in figure 2.1, that is a knowledge of the physical processes of the upper and under water surface, the atmospheric interaction and a knowledge of the sensors characteristics and the electronic signal processing which has been applied.

Appendix B

The Electromagnetic Spectrum

All satellite sensors make use of electromagnetic (e.m.) radiation for their observations. Here we review main properties of e.m. radiation as applied to remote sensing. Figure B.1 shows the part of the e.m. spectrum that is of relevant to remote sensing. It ranges from ultraviolet (UV) rays at 0.1 μm through visible, infrared (IR), and microwave radiation to radio waves at 1km wavelength. The figure also shows the corresponding frequency of the types of radiation. The visible spectrum is defined between 0.4 μm and 0.7 μm, the infrared between near and middle-IR (0.7 to 3μm) and far-IR (thermal and emissive, from 3μm to 1mm), and microwave from 1mm to 1m.

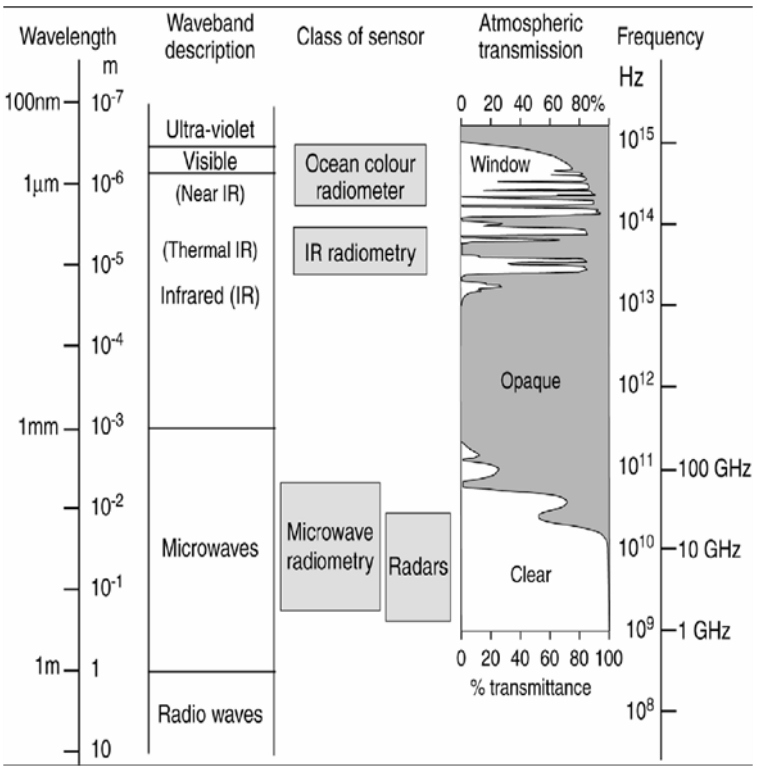

Figure B.1 The electromagnetic spectrum showing the regions exploited by typical remote sensing sensors and the corresponding atmospheric transmittance.

Figure B.1 also indicates which parts of the spectrum are used by remote sensing sensors. The choice of bands is governed firstly by the atmospheric transmission spectrum, and secondly by the source of the e.m. energy in relation to the application. The Earth's

atmosphere contains roughly 78% nitrogen, 20% oxygen, a variable amount of water vapour and small amount of other gases and aerosols. As we discuss in the next paragraph, the e.m. radiation interacts with the atmosphere through two fundamental processes: *absorption* and *scattering*. Thus it can absorbs and/or scatters part of the incoming energy. In particular, the atmosphere absorbs most radiation at wavelength less than 350nm. There are definite wavelength ranges, across the visible and near-IR, and also at select bands within the thermal-IR, where the atmosphere is fairly transparent. These are referred to as *spectral windows*, and are the bands that have been exploited for remote sensing, leading to the development of two distinct families of sensors: visible/near-IR and thermal-IR radiometers. For wavelengths between 20μm and 3mm there is almost complete absorption, but above this (from microwave to radio wave) there is very little absorption. Microwave radiometers observe the small amounts of naturally occurring radiation in the 1-mm to 10-cm wavelength range, but mostly the microwave part of the spectrum is exploited by instruments that create their own radiation with which to illuminate the target, and then observe the nature of the reflected signal. Such sensors are known as active devices or *radars*, as distinct from the passive sensors that rely on naturally occurring radiation, as mentioned above.

Finally, we remember the natural emission process of a body. Each body at a temperature greater than 0°K emits radiation due to its thermal excitation, according to the Plank's law. The *emittance* or *irradiance* of a body is the energy emitted per unit time (power), unit surface and wavelength unit ($W/m^2/nm$) at a given temperature T. The peak in emittance at a temperature T is $\lambda_{max}= 2897/T$ ($\mu m\ k^{-1}$), according to the Wien law. The emission peak of the solar radiance is about 0.5 μm (visible range), while the peak of Earth is about 11μm (thermal infrared).

In summary, if features of the land or sea are to be observed by the reflection of incident solar radiation in the same way as the human eye observes, then the frequency range of high-energy solar radiation should be used, between 300 nm and 3μm, peaking in the visible range. Alternatively, if the self emission of radiation by the sea is to be the means of remote sensing, sensors should be used for the 3 to 40 μm wavelength range (thermal infrared). The emission peak of the sea surface is in fact between 9 and 11μm. However, not all the parts of these ranges are useful, since the atmosphere will not transmit them.

Appendix C

Radiation-Atmosphere Interaction

Light from a sea surface reaching a sensor in space must first pass through the atmosphere. If we are to be able to determine the contribution of the atmosphere to the satellite measured radiance to estimate the actual water-leaving radiance, an understanding of the optical processes in the atmosphere is needed. We have outlined that the propagation characteristics of e.m. waves in atmosphere constrain their use to three spectral windows (visible, infrared and microwave). However, the transparency of the atmosphere in these wavebands is not perfect. The e.m. radiation interacts with the atmosphere through the absorption and scattering processes, thus corrupting the remote sensing signal from the sea. We briefly discuss these processes, being of fundamental importance for the recovering of data at the sea surface (atmospheric correction).

The process of scattering occurs when suspended particles and gas molecules in the atmosphere diffuse part of the incoming radiation in random directions without any alteration to the wavelength of the electromagnetic energy. Scattering reduces the amount of incoming radiation reaching and/or leaving the Earth's surface, as shown for the solar spectral irradiance in figure B.1. Scattering is dependent on two factors: the wavelength of the incoming radiation and the size of the scattering particles or gas molecules. The dimensionless size parameter is defined as:

$$k = 2\pi r/\lambda,$$

where r represents the radius of the scatterer and λ the incident wavelength. If x«1, that is particles very small respect to the incident wavelength, it is used the *Rayleigh* scattering theory. Vice versa, when x»1, it is used the classical geometric optics (reflection and refraction). Otherwise, when x~1, it is used the *Mie* theory. For the scattering of radiation in the visible part of the spectrum, x ranges from much less than 1 for air molecules to ~1 for haze and smoke particles to »1 for raindrops.

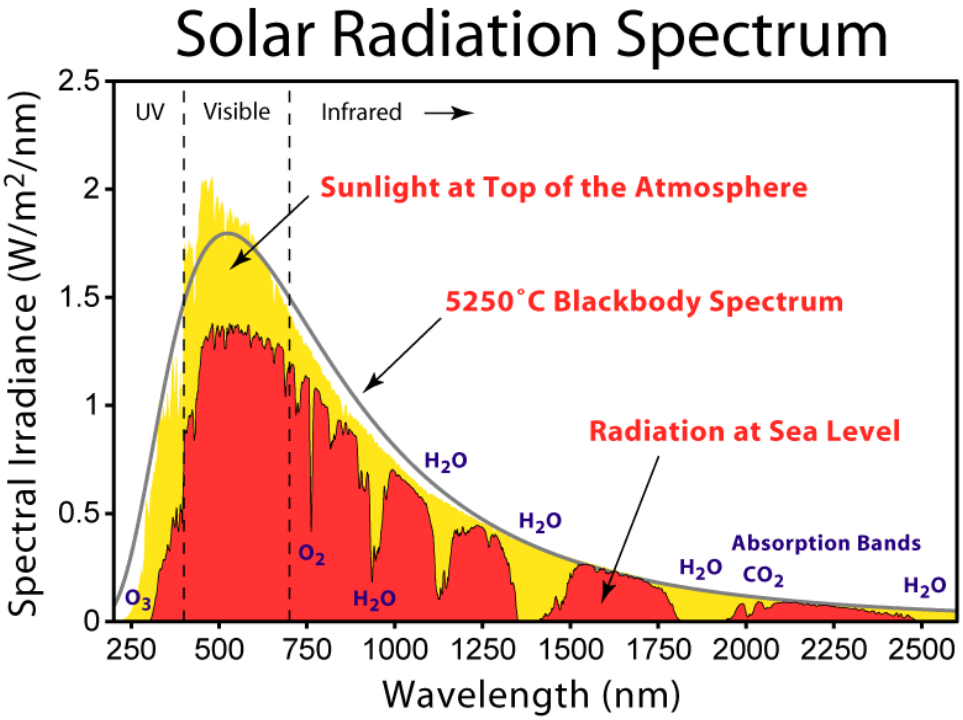

Figure B1 This figure shows the amount of light that is directly transmitted through the Earth's atmosphere for both sunlight and upgoing thermal radiation. The absorption and scattering bands that give rise to the transmission curves shown above.

Absorption is the process whereby the radiation is retained by a substance and converted into heat energy. The creation of heat energy also causes the substance to emit its own radiation. Figure B.1 shows how the solar radiation is modified by the atmospheric interaction, with an overall reduction at sea level and absorption peaks .

The visible wavelengths are affected most by scattering in the atmosphere, the thermal-IR by absorption and emission of radiation by the atmosphere's gases and water vapour, while the impact on microwaves is small but not always negligible. The most obvious impact of the atmosphere comes in the form of clouds, formed of liquid water droplets in suspension. Cloud obscure the view of the sea from space entirely, rendering visible and IR sensors useless, and there is no way of correcting for clouds in an individual image, since no information about the sea gets through to the sensor at all.

It is therefore necessary for the analysis and interpretation of the data to make allowance for the atmospheric effects. The most problematic aspect of atmospheric interference is its spatial and temporal variability, coupled closely to the uneven distribution of the water content of the atmosphere, which makes it unpredictable.

Appendix D

Classes Of Sensors

There are different families of sensors related to the type and frequency range of the e.m. radiation they use. Here we illustrate what ocean properties can be measured using different parts of the e.m. spectrum. A sensor must detect aspects of the radiation that are not only changed by an encounter with the surface ocean but that can also be correlated with a property of the sea. There are just three possible sources of the energy that can be received by a remote sensing device. It may have originated from the Sun and then been reflected, it may have been emitted by the surface being observed, or it may have been produced on the satellite by the sensor and then reflected from the sea. These are summarized in figure D.1.

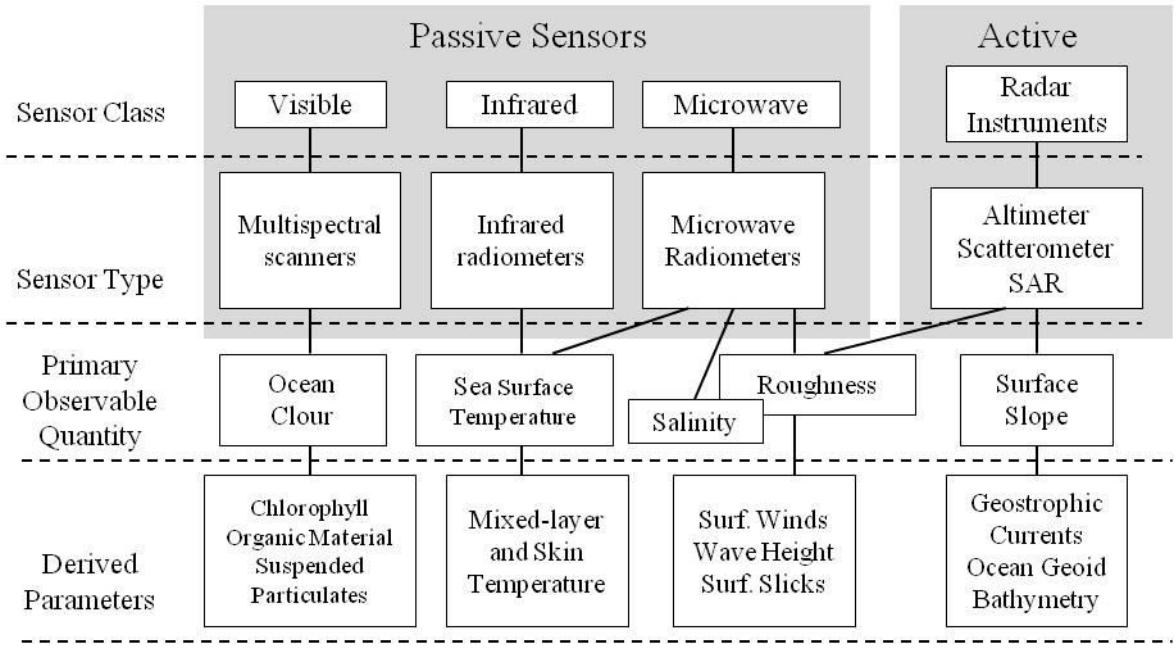

Figure D.1 Schematic illustration of different remote sensing methods and classes of sensors used in satellite oceanography, along with their applications.

The first way to classify sensors and methods of ocean remote sensing is in terms of the part of the spectrum being used, and whether the sensor is active or passive, as in the

top row of figure D.1. Passive sensors are used in the three principal spectral windows used to study the ocean, i.e. visible, thermal-IR and microwave wavebands. Active sensors on satellites all operate in the microwave. Next we can identify the different types of instruments used in each waveband, and these are placed in the second row of figure D.1.

The simplest passive remote sensing instrument is a radiometer, which measures the flux of e.m. energy reaching the sensor. Radiometers measure in the visible, thermal-IR and microwave parts of the spectrum.

Visible waveband radiometers

These are the multispectral radiometers, that measure the incoming radiation within several discrete spectral windows, in order to describe its spectral composition or colour. What is important oceanographically is that sunlight reflected by the sea into the FOV of the sensor is influenced by the optical processes in the surface layer of water, as will be discussed in more detail in the next paragraph. Thus colour is characteristic of the seawater properties. Modern imaging spectrometers have many channels, such as NASA's MODIS and ESA's MERIS sensors. It should be noted that the near-IR part of the spectrum, using the Sun's radiant energy as its source, cannot tell us much about the ocean. The reason is that the sea readily absorbs almost all the solar near-IR radiation incident upon it before it can be back-scattered. Thus the sea looks very dark in an image formed in this waveband.

Thermal-IR and microwave radiometers

Visible waveband radiometers can operate only in daylight. However, in the thermal-IR and microwave parts of the spectrum most of the observed radiation will have been thermally emitted by the sea surface. In this case the intensity can be related to the surface temperature. In this way IR and microwave radiometers can be used directly to measure *temperature*, known as *Sea Surface Temperature* (SST). The use of passive microwave radiometers to measure SST is more complex. Unlike the thermal-IR wavebands, where emissivity is almost 1, in the microwave region the emissivity of the surface is less than 0.5. The emitted radiation depends on the surface orientation and the dielectric constant of the water as well as the temperature. Thus the radiation may change if the surface roughness or the surface salinity changes, even if the SST remains constant. It does offer the possibility of using microwave radiometers for detecting sea surface roughness and salinity.

Active microwave radars

Active microwave devices provide their own energy, in the form of radar pulses which are emitted from the satellite, reflected from the sea surface and received back at the

sensor again. Since the amount of energy reflected depends largely on the short-scale profile (length scales comparable to the radar waveband) of the surface, most radars provide information about sea surface *roughness* as the primary observable quantity. Most imaging radars on satellites belong to a class known as SAR's because of the way they process data to recover detailed spatial resolution in the azimuth direction.

Appendix E

Atmospheric Correction

The atmospheric correction of the measured top of atmosphere (TOA) radiance in the visible, in order to estimate the actual water-leaving radiance, is the most crucial step in the whole of the data processing scheme for any ocean colour sensor. This is because about 80% of the measured radiance comes from atmospheric scattering and only a 20% of the signal comes from the sea surface. Here we introduce the problem and describe the "standard" procedure used for atmospheric correction.

Gordon (1978,1981) proposed an useful grouping of different ray paths, illustrated in figure E.1.

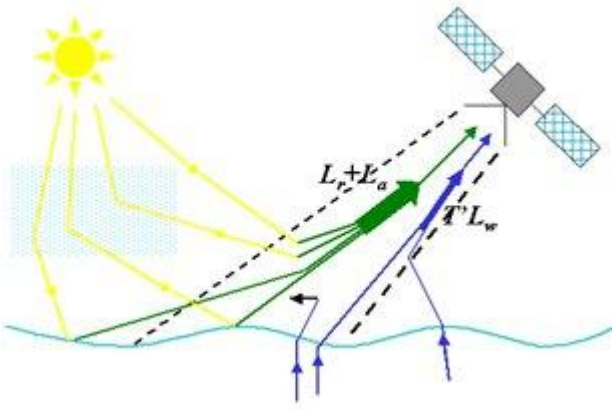

Figure E.1 Optical pathways to an ocean colour sensor, grouped to facilitate atmospheric correction.

Figure E.1 illustrates the variety of possible atmospheric pathways for light rays which can reach the sensor. Each labeled ray represents one of the following processes:

a. Rays which are scattered in the atmosphere before reflecting at the surface into the sensor. This is the *sky glitter*.

b. Rays from the sun which reflect at the sea surface directly into the sensor. This is the *sun glitter*.

c. Rays from the sun crossing through the field of view of the sensor which are scattered towards it by the atmosphere.

d. Rays which upwell from below the sea surface and, after refraction at the sea surface, point in the direction of the sensor. They may have travelled directly from the sunand been reflected once in the sea, or they may have been scattered many times before emerging. This is the water-leaving radiance (*Lw*).

e. Rays from *Lw* which are emitted by the water column, or absorbed by the atmosphere and then ri-emitted.

Figure E.1 shows that radiance received by the sensor at the top of the atmosphere is made up of two components: the atmospheric scattering radiance and the water-leaving radiance. The atmospheric component is divided in two parts, that due to Rayleigh (molecular) scattering, L_R, and that caused by aerosol particle scattering, L_A, since the molecular composition of the atmosphere is generally uniform and well known, whilst aerosols are variable in space and time. The water-leaving radiance, L_W, is the signal from the sea. If L_S represents the total radiance to the sensor, we can write:

$$L_S = L_A + L_R + T\,L_W$$

T is the atmospheric *transmittance*, i.e. the proportion of radiation passing through the atmosphere. T depends on the scattering and absorption properties of the atmosphere (see section 1.1.1). Here we note that T at a given wavelength of light, and over a path length l in the direction denoted by distance co-ordinate s is given by:

$$T_\lambda(\lambda,z) = \exp\left[-\int_0^l K(\lambda,s)ds\right] = \exp\left[-\frac{1}{\cos\vartheta}\int_0^z K(\lambda,z)dz\right] = \exp\left[-\tau(\lambda,z)/\cos\vartheta\right]$$

where $K(\lambda)$ is the attenuation coefficient, $\tau(\lambda,z)$ a dimensionless quantity called the optical thickness which represents the amount of attenuation caused by absorption and scattering between the surface and the height z. K and hence τ and T are due to the collision of photons with air molecules and with aerosols. The latter are small solid or liquid particles which may have been lifted by wind from Earth's surface, or sublimated and condensed gases from the atmosphere. The strategy of atmospheric correction is therefore to obtain L_A and L_R, from which $T\,L_W$ can be determined and thence L_W, once T is estimated. L_R can be calculated quite accurately from our knowledge of the atmospheric composition. Gordon *et al.* (1988a) and Gordon and Wang (1994b) provide the expression necessary to achieve this, which depend on the viewing and solar geometry, unique for each individual pixel. The major difficulty is to estimate L_A, since the aerosol composition and concentration cannot be modelled. The standard approach is to use measurements in wavelengths where L_W is known to be zero or very small, typically for $\lambda > 650$ nm, then, since L_R and T are also known, L_A can be determined at that wavelength. From the knowledge of L_A at one or more

wavelengths, its value is estimated across the whole spectrum, and so the full atmospheric contribution can be accounted for in order to recover L_W.

To be completed

Appendix F

Definitions Of Optical Quantities

Table F.1 lists the physical quantities mainly used to describe the measurement in optical remote sensing.

Quantity	Definition	Symbol	SI Unit
Radiant Energy	Q		J (joule)
Radiant Flux of Energy	dQ/dt	Φ	W (watt)
Irradiance (landing on surface A)	$d\Phi/dA$	E	$W\ m^{-2}$
Emittance (leaving a surface A)	$d\Phi/dA$	M	$W\ m^{-2}$
Radiant Intensity	$d\Phi/d\omega$	I	$W\ sr^{-1}$
Radiance	$dI/d(A\cos\theta)$	L	$W\ sr^{-1}\ m^{-2}$

Table F.1 List of quantities, units and conventional symbols used in optical remote sensing of the sea.

Radiant energy and *radiant flux* are the energy and power of electromagnetic waves. Thus the radiant energy of a light source is the energy emitted from the source itself in all directions, irrespective of the spatial size of the source. The radiant flux for the same source is the rate of flow of energy radiated (i.e., the energy per unit time).

Irradiance and *Emittance* represents the energy flux intercepted per unit area of a given surface (radiant flux density). The irradiance denotes a flux arriving at a surface, whilst the emittance that emitted from a surface. *E* and *M* do not in general specify the direction of the radiation, since they integrate the total flux incident on a surface from all directions capable of reaching the surface. Flux passing down into the lower part of the water column is described as the *downwelling irradiance*, *Ed*, whilst that which has been backscattered from below and is travelling towards the surface is the *upwelling irradiance*, *Eu*.

Radiant intensity, *I*, introduces the concept of direction of propagation of light. It is the radiant flux per unit solid angle leaving a point source in a given direction.

Radiance, *L*, is a radiometric measure that describe the amount of light that passes through or is emitted from a particular area, and falls within a given solid angle in a specified direction. This is a parameter of great relevance in remote sensing, since a satellite measuring radiation backscattered from the sea views the ocean surface as an extended source of light.

For the special case of remote sensing, we define the *water-leaving radiance* L_w as the upward radiance leaving the sea surface.

Reflectance, *R*, refers to the fraction of the downwelling light that is reflected back up from the water. It is defined simply as:

$$R = E_u/E_d$$

In remote sensing it is used the ratio of the upward water-leaving radiance (L_w) in the direction of the sensor and the downwelling irradiance, defined as:

$$\rho = L_w/E_d$$

Satellite Data Levels

Satellite data processing is the ensemble of procedures needed to recover geophysical products from raw data received from satellite. Raw data are digital counts of the measured e.m. radiation, known as Level 0 data. Processing can be split into four stages, to which correspond four levels of data types (L0 to L4). The level 1 data set contains calibrated and geolocated top of atmosphere (TOA) radiances generated from level L0 sensor counts. Level 2 contains oceanic optical products and various derived quantities from the observed TOA radiances. Table F.2 illustrates the first two levels of data processing together with some product.

Level	Product Description	Example
L0	Raw data received from satellite	Radiance in digital counts
L1	Image data in sensor co-ordinates Individual calibrated channels of measurements made at the satellite	Radiance at the top of atmosphere (unit)
L2	Atmospherically-corrected and calibrated image data of derived oceanic variable Geolocated, but normally presented in image co-ordinates	Water-Leaving Radiance

Table F.1 List of L0-L2 levels used in satellite data processing.

Appendix G

Technical Aspects Of Optical Sensors

A typical optical sensor scans sideways across the satellite track direction. Figure G.1 illustrates a typical arrangement where the scan lines are perpendicular to the satellite track. Normally a rotating mirror deflects the radiance from a scanned line on the ground into a focusing lens, and then into the detector system. Here it is split into several beams, each of which is fed through a diffracting grating and onto a detector. The outputs from the several detectors represent the different channels or wavebands of the sensor. The field of view (FOV) is the angular extent of the area viewed by the satellite. The area subtended by the FOV is called *swath*. The instantaneous field of view (IFOV) is the angular extent seen by a single detecting element at any given time. The IFOV defines the *spatial resolution* of the sensor, which is the shortest spacing at which variations in the scene can be detected. The time elapsed between observations of the same point on the ground is the satellite *revisit time*. It depends on the satellite's orbit, target location, and swath of the sensor. There are two scanning techniques: *mechanical* and *push-broom*. The first one provides a rotating mirror that projects the IFOV of the sensor in different portions of the ground (figure G.2, a) and onto a linear detectors array. In push-broom mode (fig. G.2, b) a bi-dimensional detection array is used, where one dimension is used to sample spectrally while the other samples instantaneously along a scan line. For fine spatial resolution, it is necessary to scan several lines in parallel, each with its own detection subsystem, in order to recover the ground while allowing enough time to scan each line. This is achieved using linear detector arrays. These consist of multiple detector elements lined up in the along-track direction, which can scan across the scene in parallel, as shown in figure G.3 (a). The major disadvantage of this scanning mode is that the two faces of the mirror and each individual detector element always have a slightly different sensitivity. This results in a striping into the images. The push-broom mode provides to align the array across-track so that the it views and samples the whole scan line in one go, as in figure G.3 (b). Several such array spectrometers may be needed in parallel to achieve a wide swath, as with MERIS. By having a large number of individual detection elements all operating in parallel, the

integration time for each element can be extended to a maximum corresponding to the travel of the satellite from one scan line to the next.

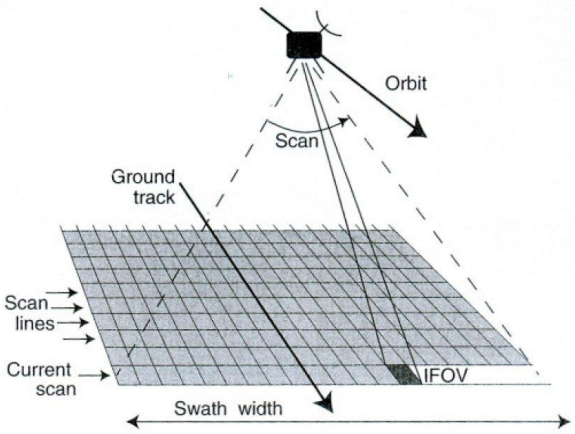

Figure G.1 Swath filling geometry of a rectangular, line-scanning sensor.

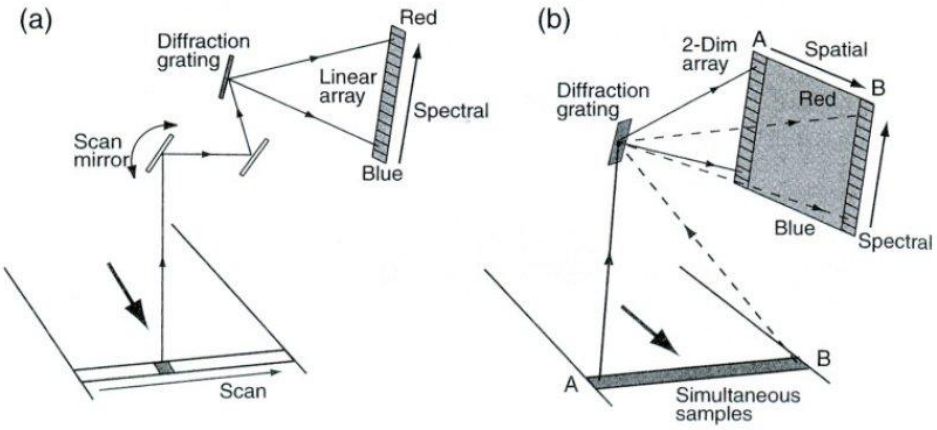

Figure G.2 Schematic of spectroradiometer type of ocean colour sensor (a) linear array, (b) 2-D array.

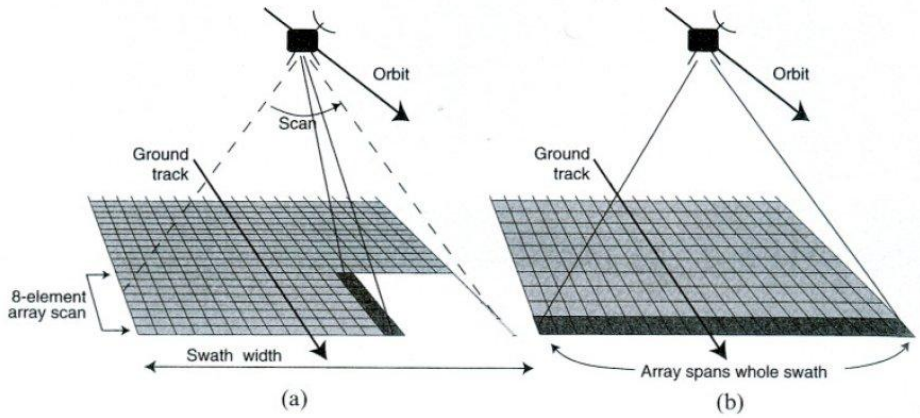

Figure G.3 Scanning with linear array detector. (a) With the elements aligned along-track several scan lines are swept out in parallel (mechanical mode). (b) With the elements aligned across-track each row of data is acquired without mechanical scanning by sampling across the array (push-broom mode).

Glossary

Aerosol

Non-gaseous microscopic particles and droplets floating in the atmosphere that have a climate forcing effect, which can be derived from natural and artificial sources, with the most abundant ones being particles of mineral dust, sulphuric acid, ammonium sulphate, biological material-like pollens, and carbon or soot.

Aerosol Optical Thickness

The factor by which the aerosol reduces optical transmission within the atmosphere.

Albedo

The ratio of the radiation reflected from an object to the total amount incident upon it, for a particular portion of the spectrum.

Azimuth Angle

Horizontal direction measured clockwise from the meridian plane.

Backscatter

In radar, the portion of the microwave energy scattered by the terrain surface directly back toward the antenna.

Bloom

A population burst of phytoplankton that remains within a defined part of the water column.

Case 1 Waters

Those oceanic or coastal waters where the ocean colour is determined by algal pigments.

Case 2 Waters

All oceanic or coastal waters which are not case I waters.

Chlorophyll

Pigments found in plant cells that are active in harnessing energy during photosynthesis.

Cloud Albedo

The ratio of the radiation reflected from the cloud's surface to the total amount incident upon it, for a particular portion of the spectrum.

Glitter

The reflection of sunlight from a rough water surface.

Mie Scattering

A form of atmospheric scatter that occurs when radiation interacts with atmospheric particles whose diameter is approximately equal to the wavelength of the radiation.

Nadir

Point on the ground directly in line with the remote sensing system and the centre of the Earth.

Ocean Colour

Study of physical and biological seawater quantities using satellite radiometers of water-leaving radiance in the visible range.

Phytoplankton

One of two groups into which plankton are divided, the other being zooplankton. Phytoplankton comprise all the freely floating photosynthetic forms in the oceans, i.e., they are free-floating microscopic plants which, having little mobility, are distributed by ocean currents.

Rayleigh Scattering

Dominant form of light scattering in the upper atmosphere, which produces the blue colour of the sky. It is caused by atmospheric particulates that have very small diameters relative to the wavelength of the light, such as dust particles or atmospheric gases like nitrogen and oxygen.

Sun Glint

Specular reflection of solar flux on ocean surface.

Total Suspended Matter

Particulates ranging in size from less than 0.1 μm to 50 μm are called Total Suspended Particulates (TSP).

White Caps

The air/water emulsion occurring at the top of ocean surface waves under high winds.

Water Vapour

Water in gaseous form.

Yellow Substance

Consists of various polymerized dissolved organic molecules which are formed by the degradation products of organisms. These originate in brackish and underground water as well as in extraordinary plankton blooms.

Zenith Angle

Angle between a look direction in the topocentric coordinate system and the zenith axis of that system.

References

AI-Ghunaim, I., Abuzar, M. & AI-Qurnas, F. S. (1992). “Delineation and monitoring of oil spill in the Arabian Gulf using Landsat thematic mapper (TM) Data”. In: Proceedings of the First Thematic Conference on Remote Sensing for Marinc and Coastal Environments, ERIM Conferences, Ann Arbor, Michigan, pp. 1151-1160.

A1-Hinai, K. G., Khan, M. A., Dabbagh, A. E. & Badcr, T. A. (1993). “Analysis of Landsat thematic mapper data for mapping oil slick concentrations-Arabian Gulf oil spill 1991”. The Arabian Journal for Science and Engineering, **18** (2), 85-93.

Alfoldi, T. T. & Prout, N. A. (1982). “The use of satellite data for monitoring oil spills in Canada”. Environment Canada Report EPS 3-EC-82-5, Ottawa, Ontario.

Antonelli P., M. di Bisceglie, R. Episcopo, C. Galdi (2004).” Destriping MODIS data using IFOV overlapping”. IEEE International Geoscience and Remote Sensing Symposium (IGARSS) proceedings, **7**, 4568 – 4571, DOI: 10.1109/IGARSS.2004.1370171.

Balick, L., DiBenedetto, J. A. & Lutz, S. S. (1997). “Fluorescence emission spectral measurements for the detection of oil on shore”. In: Proceedings of the Fourth Thematic Conference on Remote Sensing for Marine and Coastal Environments, vol. 1. Environmental Research Institute of Michigan, Ann Arbor, Michigan, pp. 13-20.

Barni, M., Betti, M., & Mecocci, A. (1995). A fuzzy approach to oil spill detection on SAR images. Proc. IGARSS ’95, vol. 1 (pp. 157– 159).

Bernardini, A., Ferraro, G., Meyer-Roux, S., Sieber, A., Tarchi, D., (2005). “Atlante dell’inquinamento da idrocarburi nel Mare Adriatico”, European Commission, EUR 21767 IT (2005).

Benelli, G., & Garzelli, A. (1999). Oil-spills detection in SAR images by fractal dimension estimation. Proc. IGARSS’99, vol. 1 (pp. 218– 220).

Bern, T-I., Wahl, T., Anderssen, T., & Olsen, R. (1993). Oil spill detection using satellite based SAR: Experience from a field experiment. *Photogrammetric Engineering and Remote Sensing* . 59 (3): 423:428.

Brekke, C, & Solberg, A. H. S. (2005).“Oil spill detection by remote sensing”, Remote Sensing of Environment **95**, 1-13.

Brown, C. E., & Fingas, M. F, (2001). “New Space-Borne Sensors For Oil Spill Response”. International Oil Spill Conference, 911-916.

Brown, C. E., Fingas, M. F, & Goodman, R.H. (1998). “Oil-spill Remote Sensors: New tools that provide solutions to old problems”. *Proc. XXI Arctic and Marine Oil spill Program Technical Seminar.*

Brown, H. M., Bittner, J. P. & Goodman, R. H. (1996). “The limits of visibility of spilled oil sheens”. In: *Proceedings of the Second Thematic International Airborne Remote Sensing Conference and Exhibition*. Environmental Research Institute of Michigan, Ann Arbor, Michigan, pp. III 327-III 334.

Brown, C. E., Fruhwirth, M., Wang, Z., Lambert, P. & Fingas, M. (1994a). “Airborne oil spill sensor test program”. In: Proceedings of the Second Thematic Conference on Remote Sensing for Marine and Coastal Environments: Needs, Solutions and Applications. ERIM Conferences, Ann Arbor, Michigan, pp. 1-19-33.

Brown, C. E., Wang, Z., Fruhwirth, M. & Fingas, M. (1994b). “May 1993 oil-spill sensor test program: correlation of laser fluorosensor data with chemical analysis”. In: Proceedings of the Seventeenth Arctic and Marine Oilspill Technical Seminar. Environment Canada, Ottawa, Ontario, pp. 1239-1261.

Byfiel, V., & Boxal, B. (1999). “Thickness estimated and classification of surface oil using passive sensing at visible and near-infrared wavelength”. *Proc. Of the IEEE International Geoscience and Remote Sensing Symposium,* 1475-1477.

Casciello, D., Lacava, T., Pergola, N., & Tramutoli, V., (2007). “Robust Satellite Techniques (RST) for Oil Spill Detection and Monitoring”. *Fourth International Workshop on the Analysis of Multitemporal Remote Sensing Images*, MultiTemp 2007, July 18-20, 2007 Leuven, Belgium, 2007a.

Cecamore, P., Ciappa, A. & Perusini, V. (1992). “Monitoring the oil spill following the wreck of the tanker Haven in the Gulf of Genoa through satellite remote sensing techniques”. In: Proceedings of the First Thematic Conference on Remote Sensing for Marine and Coastal Environments. ERIM Conferences, Ann Arbor, Michigan, pp. 183-189.

Cleanseanet, <http://cleanseanet.emsa.europa.eu/>

Comaniciu D., P. Meer (1997). “Robust analysis of feature spaces: color image segmentation”. Proc. IEEE Conference on Computer Vision and Pattern Recognition, San Juan, Puerto Rico June 1997, 750-755.

Comaniciu D., P. Meer (2002). “Mean Shift: a robust approach toward feature space analysis”. IEEE Trans. Pattern Anal. Machine Intell., **24**, 603-619.

Cross, A. (1992). “Monitoring marine oil pollution using AVHRR data: observations off the coast of Kuwait and Saudi Arabia during January 1991”. International Journal of Remote Sensing, 13, 781-788.

Dawe, B. R., Parashar, S. K., Ryan, T. P. & Worsfold, R. O. (1981). “The use of satellite imagery for tracking the Kurdistan oil spill”. Environment Canada Report EPS 4-EC-81-6, Ottawa, Ontario.

Dean, K. G., Stringer, W. J., Groves, J. E., Ahlinas, K. & Royer, T. C. (1990). “The Exxon Valdez oil spill: satellite analyses”. In: Spalding, M.L., Reed, M. (Eds), Oil Spills: Management and Legislative Implications. American Society of Civil Engineers, New York, pp. 492-502.

Del Frate, F., Petrocchi, A., Lichtenegger, J., Calabresi, G., (2000). “Neural networks for oil spill detection using ERS-SAR data”. *IEEE Transactions on Geoscience and Remote Sensing* **38**, 2282–2287.

EMSA, http://www.emsa.europa.eu/

ERS-1, http://earth.esa.int/ers/satconc/

ERS-2 Web-site. (2004). http://earth.esa.int/services/pg/pgerssarpri.xml, accessed 20 October 2004.

Espedal, H. (1999). Detection of oil spill and natural film in the marine environment by spaceborne SAR. Proc. IGARSS’99, vol. 3 (pp. 1478– 1480).

Espedal, H. A. (1998). Detection of oil spill and natural film in the marine environment by spaceborne synthetic aperture radar. PhD thesis, Department of Physics University of Bergen and Nansen Environment and Remote Sensing Center, Norway.

Espedal, H. A., & Johannessen, O. M. (2000). Detection of oil spills near offshore installations using synthetic aperture radar (SAR). International Journal of Remote Sensing, 21(11), 2141–2144.

Espedal, H. A., & Wahl, T. (1999). Satellite SAR oil spill detection using wind history information. International Journal of Remote Sensing, 20(1), 49–65.

European Space Agency, (1998). “Oil pollution monitoring”. ESA brochure: ERS and its applications—Marine, BR-128, 1.

European Space Agency. (2002). ASAR product handbook. Tech. rep., European Space Agancy-ENVISAT Product Handbook, Issue 1.1, 1 December 2002.

Ferraro, G., Bernardini, A., David, M., Meyer-Roux, S., Muellenhof, O., Perkovic, M., Tarchi, D., & Tpouzelis, K., (2007). “Towards an operational use of space imagery for oil pollution monitoring in the Mediterranean basin: A demonstration in the Adritatic Sea”. Marine Pollution Bulletin, **54**, 403-422

Ferraro, G., Tarchi, D., Fortuny, J., Sieber, A., (2006a). “Satellite monitoring of accidental and deliberate marine pollution”. In: Gade, M., Hu¨ hnerfuss, H., Korenowski, G.M. (Eds.), Marine Surface Films: Chemical Characteristics, Influence on Air-Sea Interactions, and Remote Sensing. Springer, Heidelberg.

Ferraro, G., Bernardini, A., Meyer-Roux S., Tarchi, D., (2006b). “Satellite monitoring of illicit discharges from vessels in the French environmental protection zone (ZPE) 1999–2004”, European Commission, EUR 22158 EN (2006).

Fingas, M. (2001). “The basics of oil spill cleanup”. Lewis Publishers.

Fingas, M. F., Brown, C. E., & Mullin, J. V., (1998). “A Comparison of the Utility of Airborne Oil Spill Remote Sensors and Satellite Sensors”. Proceedings, Fifth Conference on Remote Sensing for Marine and Coastal Environments. Environmental Research Institute of Michigan, Ann Arbor, MI. 1:I-171-I-178.

Fingas, M. F., & Brown, C. E. (1998). Review of the visibility of oil slicks and oil discharges on water, in *Proc. XXI Arctic and Marine Oil spill Program Technical Seminar*.

Fingas, M. F., & Brown, C. E. (1997). Review of oil spill remote sensing. Spill Science and Technology Bulletin, 4, 199– 208.

Fiscella, B., Giancaspro, A., Nirchio, F., Pavese, P., & Trivero, P. (2000). Oil spill detection using marine SAR images. International Journal of Remote Sensing, 21(18), 3561–3566.

Friedman, K. S., Pichel, W. G., Clemente-Colo´n, P., & Li, X. (2002). “GoMEx—an experimental GIS system for the Gulf of Mexico Region using SAR and additional satellite and ancillary data”. Proc. IGARSS’02, **6**, 3343– 3346.

Fruhwirth, M., Fingas, M. F. & Brown, C. E. (1994). “The development of oil spill laser fluorosensors at Environment Canada”. In: Proceedings of the Second Thematic Conference on Remote Sensing for Marine and Coastal Environments: Needs, Solutions and Applications. ERIM Conferences, Ann Arbor, Michigan, pp. 1-59-67.

Grimaldi, C.L.S, Casciello, D., Coviello, I., Lacava, T., Pergola, N., & V. Tramutoli, (2008). “A MODIS based Robust Satellite Technique for near real time monitoring of oil spilled areas”. *Proceeding of 2008 IEEE Gold Remote Sensing Conference*, ESAESRIN Frascati (Roma), Italy, 22-23 May 2008 (in press).

Grimaldi, C.L.S, Casciello, D., Coviello, I., Lacava, T., Pergola, N., & V. Tramutoli, (2009). “Near Real Time Oil Spill Detection And Monitoring Using Satellite Optical Data”. IGARSS 2009, **4**, 709-712.

Hengstermann, T. & Reuter, R. (1990). “Lidar fluorosensing of mineral oil spills on the sea surface”. *Applied Optics,* **29**, 3218-3227.

Hu, C.,Mqller-Krager, F. E., Taylor, C. J.,Myhre,D.,Murch, B.,Odriozola,A. L., *et al.*, (2003). “MODIS detects oil spills in Lake Maracaibo, Venezuela”. EOS, Transactions, American Geophysical Union, **84** (33), 313-319.

Huijer, K., 2005. “Trends in Oil Spills from Tanker Ships 1995-2004”. Vol. 1 Proceedings of the Twenty-eighth Arctic and Marine Oilspill Program (AMOP) Technical Seminar. 7-9 June 2005. Calgary, Canada. Pp 319-332.

Indregard, M., Solberg, A., Clayton, P. (2004). D2-report on benchmarking oil spill recognition approaches and best practice. Tech. rep., Oceanides project, European Commission, Archive No. 04-10225-A-Doc, Contract No: EVK2-CT-2003-00177.

ITOPF (International Tanker Owners Pollution Federation). Statistical information available from <http://www.itopf.com/>.

JRC, see <http://www.jrc.cec.eu.int/> and <http://serac.jrc.it/midiv/>.

Kostianoy, A., Litovchenko, K., Lavrova, O., Mityagina, M., Bocharova, T., Lebedev, S., Stanichny, S., Soloviev, D., Sirota, A., & Pichuzhkina, O., (2006). “Operational Satellite Monitoring of Oil Spill Pollution in the Southeastern Baltic Sea: 18 Months Experience.” Environmental research, engineering and management, **38** (4), 70-77.

l2gen, http://oceancolor.gsfc.nasa.gov/DOCS/MSL12/MSL12_prod.html

LMIU, (2001). “LMIU Shipping Data”, Lloyd’s Marine Intelligence Unit, 2001.

Lodge, A.E. (1989). “The Remote Sensing of Oil Slicks”. Institute of Petroleum, London, Wiley and Sons, New York, 1989.

MERIS, http://envisat.esa.int/instruments/meris/

McGarigal & Marks, 1995. “Spatial pattern analysis program for quantifying landscape structure”. http://www.umass.edu/landeco/pubs/mcgarigal.marks.1995.pdf

MODIS, http://modis.gsfc.nasa.gov

Nirchio F., Pandiscia, G.V., Ruggieri, G., Santoleri, R., Tataranni, F., Trivero, P., Pinardi, N., Masini, A., Manzella, G., & Castellani, C., (2009). PRIMI (Pilot Project Marine Oil Pollution). ISRSE 2009, 33rd International Symposium on Remote Sensing of environment Sustaining the Millennium Development Goals, May 4-8, 2009, Palazzo dei Congressi Stresa, Lago Maggiore, Italy, http://isrse-33.jrc.ec.europa.eu/.

Oceanides Web-site. (2004). http://oceanides.jrc.cec.eu.int/prestige.html, accessed 13 August 2004.

O'Neil, R. A., Neville, R. A. & Thompson, V. (1983). The Arctic Marine Oilspill Program (AMOP) remote sensing study. Environment Canada Report EPS 4-EC-83-3, Ottawa, Ontario.

Otremba, Z., (1994). “The influence of an oil-film covered sea surface on the reflection and upward transmission of light”. OCEANOLOGIA, **2** (36), 137-154.

Otremba, Z., (1997). “A thin oil film covering the sea surface as a modifier of the downward transmission of light”. OCEANOLOGIA, **4** (39), 397-411.

Otremba, Z., (2000). “The impact on the reflectance in VIS of a type of crude oil film floating on the water surface”. Optics Express, **7** (3)**,** 129-134.

Otremba, Z., & Piskozub, J., (2001). “Modelling of the optical contrast of an oil film on a sea surface”. Optics Express, **9** (8)**,** 411-416.

Otremba, Z., & Piskozub, J., (2002). “Modeling the remotely sensed optical contrast caused by oil suspended in the sea water column”. Optics Express, **11** (1)**,** 2-6.

Otremba, Z., & Piskozub, J., (2004). “Modeling the bidirectional reflectance distribution function (BRDF) of seawater polluted by an oil film”. Optics Express, **12** (8)**,** 1671-1676.

Otremba, Z., (2005). “Influence of oil dispersed in seawater on the bi-directional reflectance distribution function (BRDF)”. Optica Applicata, **35** (1)**,** 99-109.

Otremba, Z., (2009). “Influence of oil dispersed in seawater on the bi-directional reflectance distribution function (BRDF)”. Optica Applicata, **39** (1)**,** 123-128.

Pavlakis, P., Tarchi, D., Sieber, A, Ferraro, G., Vincent, G., S. (2001). “On the monitoring of illicit discharges - a reconnaissance study in the Mediterranean Sea”, European Commission, EUR 19906 EN.

Pavlakis, P., Sieber, A., & Alexandry, S. (1996, June). “Monitoring oil-spill pollution in the Mediterranean with ERS SAR”. ESA Earth Observation Quarterly (52).

Rand, R. S., Davis, D. A., Satterwhite, M. B. & Anderson, J. E. (1992). “Methods of monitoring the Persian Gulf oil spill using digital and hardcopy multiband data”. U.S. Army Corps of Engineers Report, TEC-0014.

REMPEC, see http://www.rempec.org.

REMPEC, 2002. “Protecting the Mediterranean against maritime accidents and illegal discharges from ships”. Malta, 2002.

Robinson, I. S. (1994). Satellite oceanography. An introduction for oceanographers and remote-sensing scientists. Wiley–Praxis series in remote sensing.

Salem, F., & Kafatos, P. M. (2001). “Hyperspectral image analysis for oil spill mitigation”. Proc. ACRS 2001-22nd Asian Conference on Remote Sensing, 5-9 November 2001, Singapore, **1**, 748– 753.

Sherman, J. W.III. (1992). Historical Perspectives: “Marine Oil Spill Detection by Remote Sensing”, in The First Thematic Conference on Remote Sensing for Marine and Coastal Environment, New Orleans, Louisiana, 1992, pp. 15-17.

Solberg, A. H. S., Dokken, S. T., & Solberg, R. (2003). Automatic detection of oil spills in Envisat, Radarsat and ERS SAR images. Proc. IGARSS’03, vol. 4 (pp. 2747–2749).

Solberg, A. H. S., & Solberg, R. (1996). A large-scale evaluation of features for automatic detection of oil spills in ERS SAR images. Proc. IGARSS’96, vol. 3 (pp. 1484–1486).

Solberg, A. H. S., Storvik, G., Solberg, R., & Volden, E. (1999). Automatic detection of oil spills in ERS SAR images. IEEE Transactions on Geoscience and Remote Sensing, 37(4), 1916– 1924.

Solberg, A. H. S., & Volden, E. (1997). Incorporation of prior knowledge in automatic classification of oil spills in ERS SAR images. Proc. IGARSS'97, vol. 1 (pp. 157– 159).

Tarchi, D., Bernardini, A., Ferraro, G., Meyer-Roux, S., Muellenhoff, O., Topouzelis, K., (2006). "Satellite monitoring of illicit discharges from vessels in the seas around Italy 1999–2004", European Commission, EUR 22190 EN (2006).

Topouzelis, K., Karathanassi, V., Pavlakis, P., Rokos, D., (2002). "Oil spill detection: SAR multi-scale segmentation and object features evaluation". In: 9th International Symposium on Remote Sensing (SPIE), pp. 77–87.

Topouzelis, K., Bernardini, A., Ferraro, G., Meyer-Roux, S., Tarchi, D., (2006). "Satellite mapping of oil spills in the mediterranean sea". Fresenius Environmental Bulletin 15, 1009-1–1009-14.

Trieschmann, O., Hunsanger, T., Tufte, L., & Barjenbruch, U. (2003). "Data assimilation of an airborne multiple remote sensor system and of satellite images for the North- and Baltic sea". *Proceedings of the SPIE 10th int. symposium on remote sensing, conference " remote sensing of the ocean and sea ice 2003",* pp. 51–60.

Tseng, W. Y., & Chiu, L. S. (1994). "AVHRR observations of Persian Gulf oil spills". Proc. IGARSS'94, **2**, 779– 782.

Ulaby, F. T., Moore, R. K., & Fung, A. K. (1986). Microwave remote sensing: Active and passive. Vol. 3: From Theory to Applications. Artech house.

Voloshina, I. P. & Sochnev, O. Y., (1992). "Observations of surface contaminations of the region of the Kol'shii Gulf from IR measurements". Soviet Journal of Remote Sensing, **9** (6), 996-1000.

Wahl, T., Eldhuset, K., Skoelv, A., (1993). Ship Traffic Monitoring and Oil Spill Detection Using ERS-1. *Proceedings*, Conference of Operalization of Remote Sensing. ITC. Pp. 97-105.

Weinreb M. P., R. Xie, J. H. Lienesch, D. S. Crosby (1989). "Destriping GOES Images by Matching Empirical Distribution Functions". Remote Sens. Environ., **29**, 185-195.

Zhifu, S., Kai, Z., Baojiang, L., & Futao, L. (2002). "Oil-spill monitoring using microwave radiometer". Proc. IGARSS'02, **5**, 2980– 2982.